Precision Measurements of the LEP Beam Energy for the Determination of the W Boson Mass

Dissertation
zur Erlangung des Grades
"Doktor der Naturwissenschaften"
am Fachbereich Physik
der Johannes Gutenberg-Universität
in Mainz

Anke-Susanne Müller
geboren in Frankfurt am Main

Mainz 2000

Abstract

The measurement of the W Boson mass at LEP2 requires a determination of the beam energy with the highest possible accuracy. Present schemes for energy calibration above the W^+W^- threshold of 80 GeV are based on extrapolations of resonant depolarization measurements to high energy. Since such extrapolations involve systematic uncertainties, alternative methods have been studied which are based on measurements of the energy loss due to synchrotron radiation. Because this energy loss increases with the fourth power of energy, observables sensitive to the energy loss per turn can be used to determine the beam energy.
Three different methods to measure the energy loss have been studied. The first technique is based on the analysis of electron positron difference orbits, the second on measurements of the damping of horizontal coherent oscillations after an excitation and the last one on studies of the relation between synchrotron tune Q_s and total accelerating voltage. As a side product, the analysis of the damping of coherent oscillations gives an opportunity to measure the horizontal detuning with amplitude (anharmonicity), which is an important parameter for the understanding of the dynamic aperture of storage ring optics. This thesis focuses on the description of the different approaches to the energy loss measurement and discusses advantages and disadvantages of the methods. The impact of beam parameters like center-of-mass energy and asymmetries of electron and positron beam energies on the measurement of the mass of the W boson is studied.

Contents

Chapter 1

Introduction

The **L**arge **E**lectron **P**ositron collider LEP [1] at CERN is situated near the Swiss-French border. The ring extends from the foothills of the Jura mountain to the Geneva airport as shown in figure 1.1. LEP consists of eight arcs and eight straight sections with interaction points (IPs).

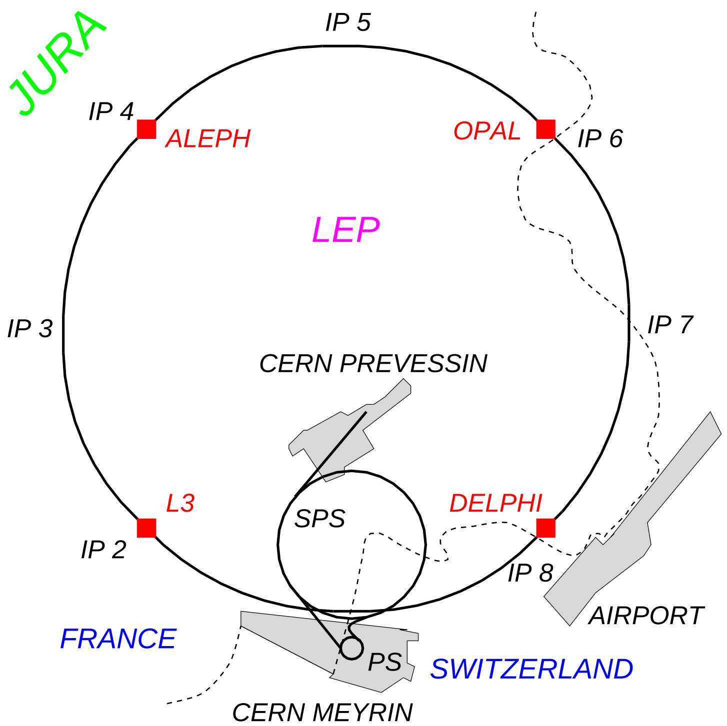

Fig. 1.1: *Situation of the LEP accelerator. LEP comprises eight interaction regions with four experiments.*

In the even interaction points four large halls house the detectors of the LEP experimental collaborations L3, ALEPH, OPAL and DELPHI. One very important aim of the LEP physics program are precision tests of the Standard Model (SM). The accurate measurements of Standard

Model parameters can be used to search for deviations from the SM at the level of quantum corrections.
From 1989 to 1995 the LEP machine was operated at beam energies around 45.6 GeV to study the properties of the Z boson. Since 1996 LEP was operated at beam energies above the threshold for W pair production of 80 GeV [2]. Physics aims for this LEP2 phase are (among others) the precision determination of the mass of the W boson which is an important SM parameter and to test the gauge structure of the SM in studies of ZWW vertices and anomalous couplings [3].
In the framework of the Standard Model the two following processes contribute to the W pair production:

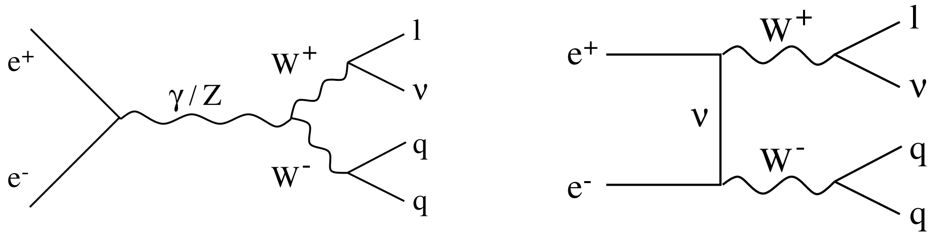

the s-channel exchange of a Z or a γ and the t-channel exchange of an electron neutrino. Each W decays either in two quarks or in a lepton and its corresponding neutrino as indicated in the diagrams. Figure 1.2 shows the W pair production cross-section as function of the center-of-

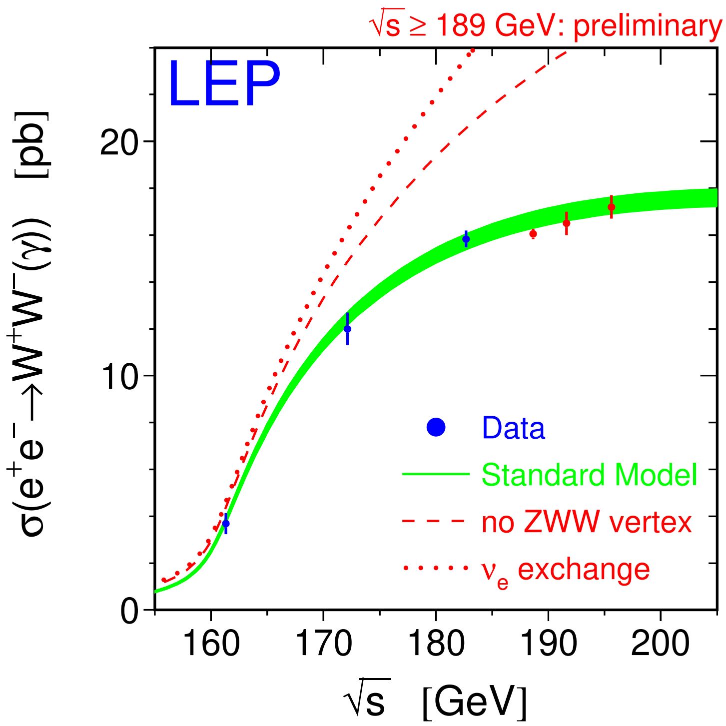

Fig. 1.2: *W pair production cross-section as function of the center-of-mass energy. LEP combined results are shown. (Plot by the LEP electroweak working group)*

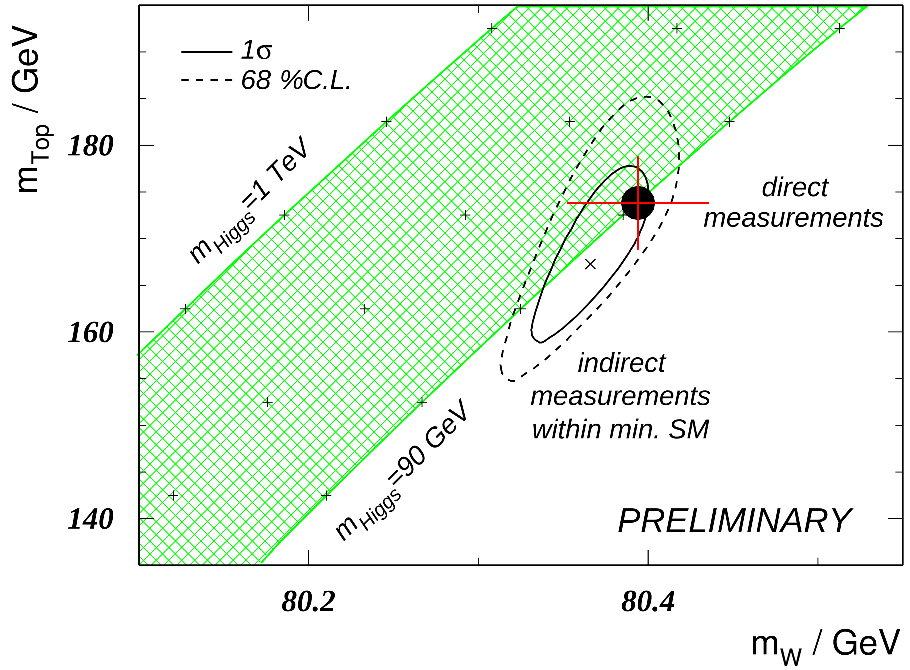

Fig. 1.3: *Mass of the* t *quark versus the W mass. Direct measurements are compared to results from indirect determinations. The band represents the Standard Model expectation for the relation between top and W mass for Higgs masses between 90 GeV and 1 TeV. Within the minimal SM the data show a strong preference for a light Higgs boson [4].*

mass energy of LEP. Three different predictions for the cross-section are drawn: the cross-section with only t-channel neutrino exchange, the cross-section without Z exchange and the complete Standard Model prediction as a band which indicates the theoretical uncertainties. At higher center-of-mass energies the s- and t-channel diagrams interfere destructively and the existence of the ZWW vertex (expected from the non-Abelian structure of the SU(2)) yields a reduced cross-section which is in good agreement with the observations.
The mass of the W boson m_W is also very interesting for consistency checks of the SM, since it enters into indirect determinations of other parameters, like for example the mass of the Higgs boson [5]. Electroweak vertex and propagator loops induce a sensitivity of observables (like m_W) to heavy particles like the top quark, the yet undiscovered Higgs boson or even to particles beyond the scope of the Standard Model. Figure 1.3 indicates how precision measurements of m_t and m_W allow to constrain the Higgs mass. A future comparison of a direct measurement of the Higgs mass with an accurate indirect determination would be a powerful test of the consistency of the SM. Any deviation would give unambiguous evidence for physics beyond the SM.

Precision tests like the measurement of the W mass require an accurate determination of the beam energy and a good understanding of the accelerator to guarantee stable running with high luminosities at high beam energies [6]. The relative error on the beam energy translates into the same uncertainty on the measured m_W since the beam energy is used as kinematic constraint to improve the mass resolution. A stable running with high luminosities is essential to bring down the statistical uncertainty of the W mass measurement.

This thesis is organized as follows. After the introduction, first a short description of the basic concepts of accelerator physics is given. Problems of operating an accelerator at high energies are discussed in the third chapter, and a method to measure the horizontal anharmonicity is presented which turned out to be an important stability criterion for the LEP high energy optics. The procedure of the LEP2 energy calibration is discussed in chapter 4. The standard method is based on precise energy determinations with resonant depolarization in the energy range from 40 to 60 GeV and on extrapolations to the respective physics energies. These extrapolations show differences which are not fully understood and enter as a large contribution in the uncertainty on the beam energy. To provide an independent cross check for the standard extrapolations three methods to determine the beam energy above the W pair production threshold based on measurements of the energy loss have been studied and are discussed in chapters 5 to 7. The determinations of the beam energy based on the analysis of the damping of transverse coherent beam oscillations and the study of the energy sawtooth do not meet the precision requirements for a LEP energy calibration. The beam energy measurement based on the analysis of synchrotron oscillations provides a powerful and reliable high precision cross check for high energy calibration. The measurement and analysis procedure is presented and a detailed discussion of systematic effects is given.

Finally the impact of machine parameters like center-of-mass energy of the electron-positron system and asymmetries of electron and positron beam energies on the measurement of m_W is studied.

Chapter 2

Concepts of Accelerator Physics

This chapter is a short introduction to the structure and the properties of an accelerator lattice. Its purpose is to introduce all quantities necessary for the understanding of the following chapters. More detailed descriptions of the physics involved can be found in [7–10].

2.1 Transverse Motion

2.1.1 Bending Magnets

To guide the particles around the 26.7 km circumference of LEP, a homogeneous vertical magnetic field is needed. This field is provided by 3336 dipoles (see fig. 2.1 and fig. C.2) with a length of ~ 5.75 m each and a weight of ~ 4.6 tons. The radius of curvature for a particle of

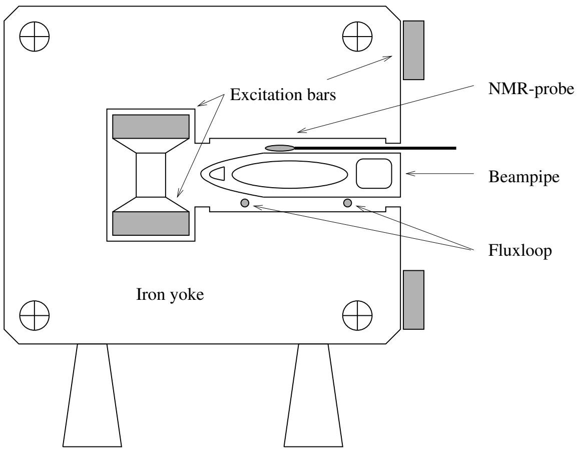

Fig. 2.1: *Cross section of a LEP bending dipole with elliptical vacuum chamber, flux-loop cables and an NMR probe (used for energy calibration).*

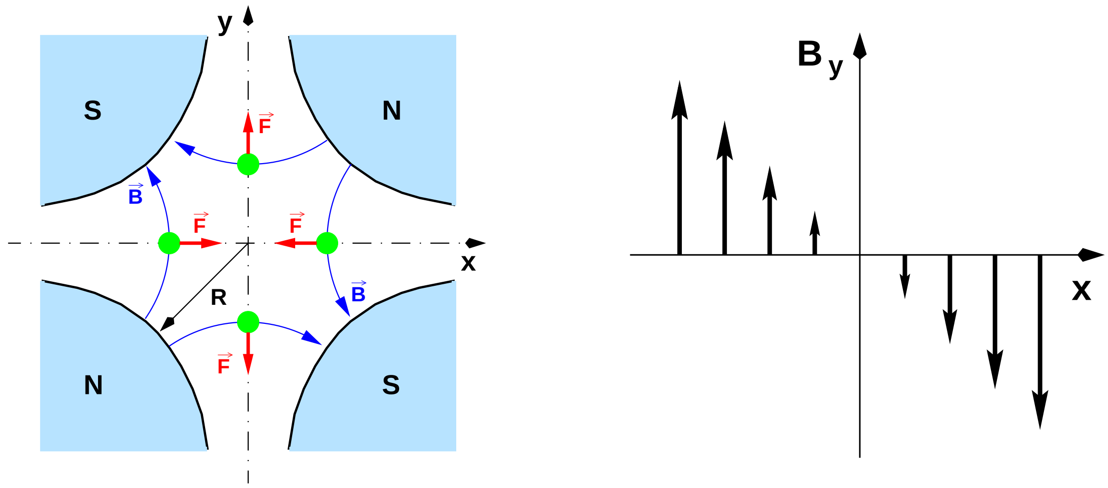

Fig. 2.2: *Transverse section of a horizontally focusing quadrupole. The left sketch shows how the Lorentz force acts on a particle of positive charge traveling into the image plane. The result is a focusing effect in the horizontal plane and a defocusing effect in the vertical plane. The right sketch shows how the magnetic field close to the center increases with the distance from the magnet's center.*

charge e and momentum p is given by

$$\frac{1}{\rho} = \left|\frac{e\ B}{p}\right| = \left|\frac{e\ c\ B}{\beta\ E}\right|. \tag{2.1}$$

The total magnetic length of the LEP dipoles is about 19.2 km. The field range extends from 0.01 to 0.2 T and the bending radius is about 3 km. As indicated in figure 2.1, all dipoles are equipped with flux loop cables which are used to measure the integrated magnetic field ($\int B dl$) by induction during a field ramp. Some dipoles are also equipped with NMR probes (**N**uclear **M**agnetic **R**esonance, see chapter 4). The magnetic measurement devices are used for energy calibration and will be described in more detail later.

2.1.2 Quadrupoles

Quadrupole magnets are used to focus the particle beams. More than 800 quadrupoles are installed in LEP. The quadrupole field (fig. 2.2) increases linearly with the distance from the magnet's center:

$$B_x(y) = -\ g \cdot y \qquad\qquad B_y(x) = -\ g \cdot x. \tag{2.2}$$

For perfectly shaped pole faces the gradient $g = \partial B_y/\partial x = \partial B_x/\partial y$ is given by

$$g = \frac{2\mu_0 n I}{R^2}$$

where I is the current in the n coils and R the distance of the poles from the center of the magnet. It is convenient to define a normalized quadrupole strength in analogy to the curvature

$1/\rho$ of a dipole magnet:

$$k = \frac{e}{p}\, g \tag{2.3}$$

where e and p are charge and momentum of the particle.

The quadrupole field is focusing in one plane and defocusing in the other. To focus the beam in both transverse planes, the focusing must be done alternatively in the horizontal and vertical planes (fig. 2.3). In the following the expression *focusing* will be used for a horizontally focusing and vertically defocusing quadrupole and *defocusing* for a horizontally defocusing but vertically focusing quadrupole. Focusing and defocusing quadrupoles are organized in structures called

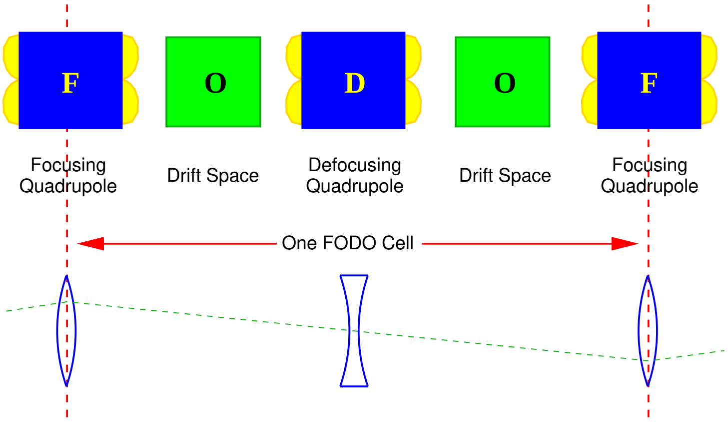

Fig. 2.3: *FODO cell - magnet structure and optical lens representation.*

FODO cells (F: focusing quadrupole, D: defocusing quadrupole, O: drift space) as shown in figure 2.3. Below the magnets an optical lens representation of the focusing mechanism in the horizontal plane is drawn. Bending of the trajectories is achieved by placing dipoles in the drift spaces of the FODO cells. The accelerator lattice is composed of a periodic structure of FODO cells in the arcs with bending dipoles in the drift spaces (fig. 2.4 on the following page). The motion of a particle in this lattice is discussed in the following section.

2.1.3 Equation of Motion and Phase Advance

The equation of motion for the transverse planes is a second order differential equation with a periodic driving term. It can be written in the form of Hill's equation:

$$\begin{aligned} u'' + K(s)u &= 0 \\ K(s+l) &= K(s) \end{aligned} \tag{2.4}$$

where $u(s)$ stands for the horizontal or vertical coordinate ($x(s)$ or $y(s)$) and s is the longitudinal coordinate. For a circular accelerator $K(s)$ is a periodic function with the period l (full circumference or length of a FODO cell for a periodic lattice). The form of eq. (2.4) is valid for

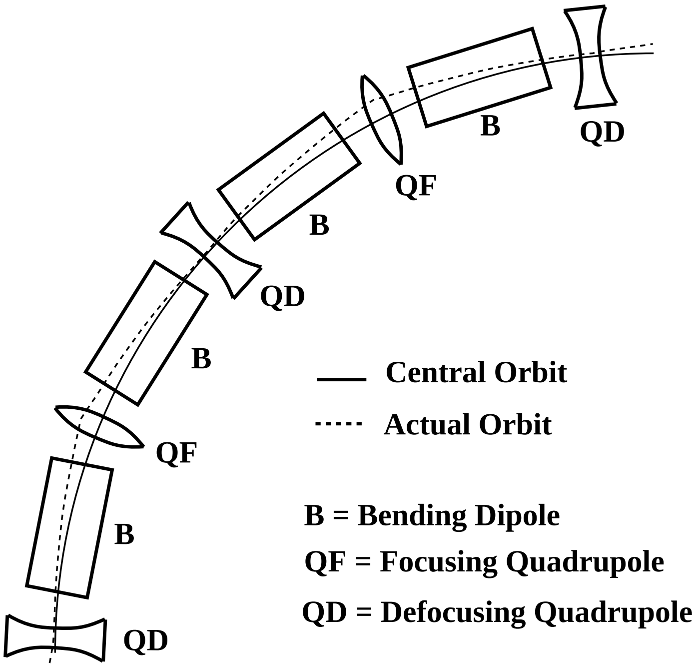

Fig. 2.4: *A regular FODO lattice. The solid curve represents the central orbit (no momentum deviation), the dashed curve shows an off-momentum orbit. [11]*

particles with nominal momentum and no coupling between the horizontal and vertical planes. For the individual planes $K(s)$ is given by

$$K(s) = \begin{cases} -k(s) + \frac{1}{\rho(s)^2} & \text{horizontal plane} \\ +k(s) & \text{vertical plane} \end{cases} \tag{2.5}$$

where $k(s)$ is the quadrupole strength and $\rho(s)$ the (local) bending radius. The independent solutions of the Hill equation are

$$\begin{aligned} u(s) &= a\sqrt{\beta(s)}\; e^{\pm i(\Phi(s)+\Phi_0)} \\ \text{with } \Phi'(s) &= \frac{1}{\beta(s)} \text{ and } a = \text{const.} \end{aligned} \tag{2.6}$$

A particle trajectory is described by a real solution of Hill's equation. The *betatron function* $\beta(s)$ is a continuous function given by the structure of the lattice which depends on the longitudinal coordinate s. The envelope function for all particle trajectories is proportional to the square root of the betatron function. In a circular accelerator each quadrupole affects the betatron function all along the ring. This is similar to an optical setup where a change in a single lens affects the entire down-stream optics.

The phase advance per period of length l (full circumference or length of a FODO cell) is derived from the betatron function:

$$\mu = \mu(s,l) = \int_s^{s+l} \frac{1}{\beta(t)} dt. \tag{2.7}$$

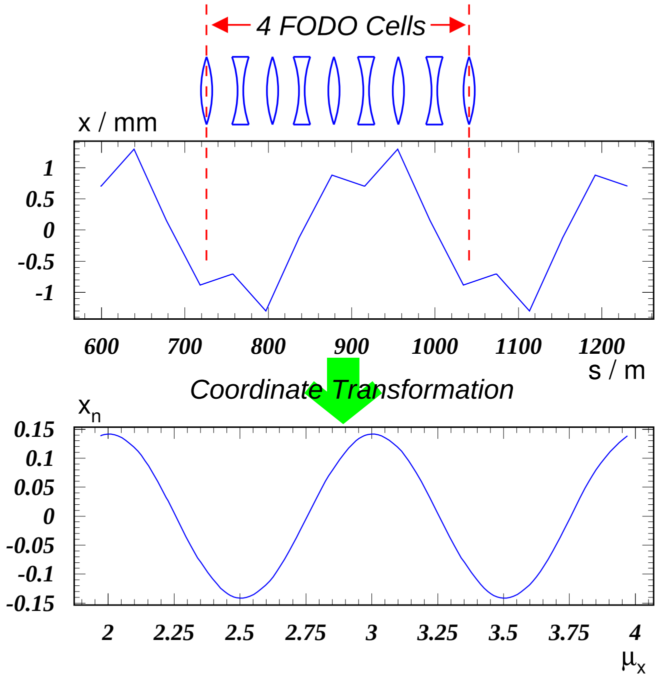

Fig. 2.5: *Particle trajectory in a regular FODO lattice. The upper plot shows the horizontal particle position $x(s)$ as a function of the longitudinal coordinate s. In the bottom plot the position normalized by the square root of the betatron function $x_n(s)$ is drawn as a function of the horizontal phase advance μ.*

A particle trajectory in a regular FODO lattice is displayed in fig. 2.5 together with the focusing and defocusing quadrupoles of the FODO structure. The deflections caused by the quadrupoles can be clearly identified. Since the phase of the oscillation advances by 2π over four cells, the phase advance per period (i.e. per FODO cell) is 90^o in this case. The phase advance per period μ is a parameter which is characteristic for a given optics. At LEP it is therefore used as a key to name different optics: " $90^o/60^o$ " for example stands for an optics with 90^o horizontal and 60^o vertical phase advance per cell. If the particle position is normalized by the square root of the betatron function and plotted versus the local phase advance $\mu(0,s) = \Phi(s)$ the sinusoidal character of the solutions of Hill's equation becomes clear (bottom plot of fig. 2.5).

2.1.4 Tune and Optical Resonances

The betatron oscillations described by solutions of Hill's equation lead to the definition of the tune of the machine. The tune or "Q-value" is defined as the number of betatron oscillations per revolution. For an accelerator with N periods, the Q-value is given by

$$Q = \frac{N\,\mu}{2\pi} = \frac{1}{2\pi}\int_0^L \frac{ds}{\beta(s)} = \frac{1}{2\pi}\oint \frac{ds}{\beta(s)} \tag{2.8}$$

where the integral [1] is evaluated on the closed orbit (closed path through the ring, in the absence of alignment and field errors equal to a path through the center of all magnets). The horizontal and vertical tunes (Q_x,Q_y) define the "tune working point" of a machine. Often only the fractional part of the tune is given. To have bounded motion the tune must not reach certain

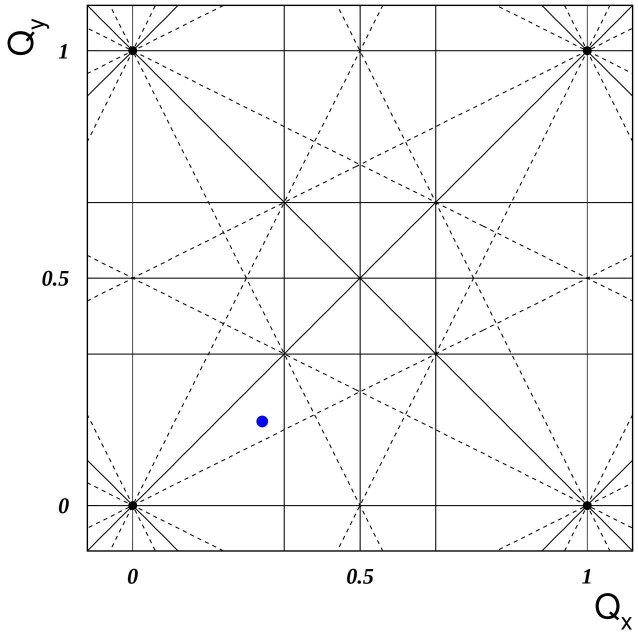

Fig. 2.6: *Optical resonances up to the third order in the horizontal and vertical plane. The non-integer part of the vertical tune Q_y is plotted versus the non-integer part of the horizontal tune Q_x. The dot denotes a LEP tune working point.*

rational numbers which can cause the motion to resonate (small perturbations due to field errors of the magnets add up over several turns) and result in losses. The fact that in a real machine there is always coupling between horizontal and vertical motion leads to a general condition for the appearance of optical resonances:

$$mQ_x + nQ_y \;=\; p \qquad \text{with} \quad m, n, p \in \mathbb{Z} \tag{2.9}$$

and m, n small. The order of a resonance is given by $|m| + |n|$. Dipole field errors lead to first order (integer) resonances, quadrupole errors to second order (half-integer) resonances and sextupole errors (see later in this chapter) to resonances on third-integer values of Q. An e^+e^- storage ring like LEP is only sensitive to resonances up to the third order thanks to the strong damping caused by synchrotron radiation. Figure 2.6 shows a tune diagram with resonance lines up to the third order. The tune working point has to be chosen in a safe distance to resonance lines.

---

[1] The integral $\int_0^L ds$ over the closed orbit is often written as $\oint ds$.

2.1.5 Emittance, Twiss Parameters and Courant-Snyder Invariant

A particle trajectory given by eq. (2.6) and its first derivative form a parametric representation of an ellipse in the u-u' plane at place s:

$$\begin{aligned} u(s) &= a\sqrt{\beta(s)}\ \cos\left(\Phi(s)-\delta\right) \\ u'(s) &= -\frac{a}{\sqrt{\beta(s)}}\left(\sin\left(\Phi(s)-\delta\right)\ -\ \frac{1}{2}\frac{d}{ds}\beta(s)\ \cos\left(\Phi(s)-\delta\right)\right) \end{aligned} \tag{2.10}$$

where δ is an arbitrary phase angle. The area of this phase space ellipse $\pi\ a^2$ is independent of s in the absence of non-conservative forces. The quantity a^2 is called the *Courant-Snyder invariant* W. In Cartesian coordinate representation the ellipse equation can be written as:

$$\begin{aligned} &\gamma u^2 + 2\alpha u u' + \beta u'^2 = W_u \\ &\alpha = -\frac{1}{2}\ \beta' \qquad \gamma = \frac{1+\alpha^2}{\beta} \end{aligned} \tag{2.11}$$

where α, β and γ are the so-called Twiss parameters. Figure 2.7 shows a phase space ellipse in the horizontal plane. Maxima and intersections with onto abscissa and ordinate are given. Shape

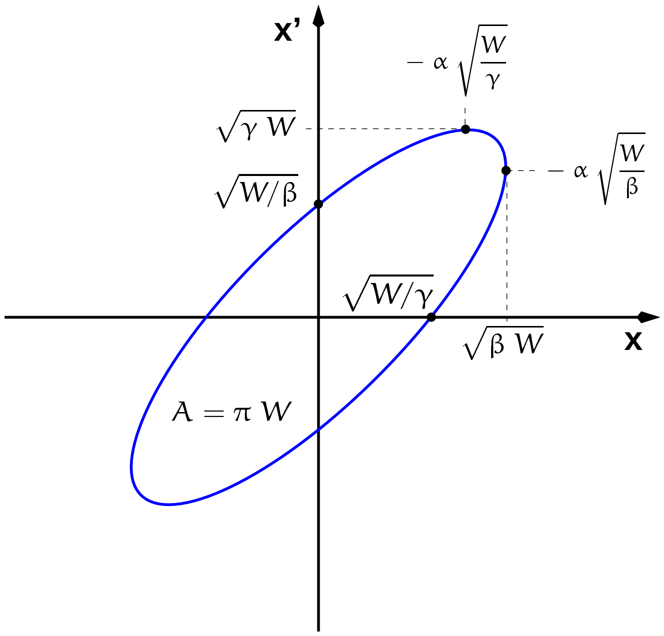

Fig. 2.7: *Phase ellipse of horizontal particle motion in the x-x' plane. The area of the ellipse is given by the Courant-Snyder invariant W.*

and orientation of the ellipse depend on s. In a regular FODO lattice for example, β' vanishes in the center of a quadrupole in which case the main axes of the ellipse coincide with ordinate and abscissa. Figure 2.7 indicates that the Courant-Snyder invariant W can be extracted by a determination of the maximum elongation $\sqrt{\beta\ W}$ provided the local betatron function is known. The maximum elongation can be obtained turn by turn form a measurement of the position at

two places separated by 90° in phase. From the relation for the transverse position in eq. (2.10) it is immediately visible that the sum of the squares of the measured positions yields the square of the oscillation amplitude which is identified with the maximum elongation $\sqrt{\beta\, W}$. This procedure was used for the determination of W in section 3.1.
The Courant-Snyder invariant W corresponds to a single particle emittance. For a bunch of N particles with a two-dimensional Gaussian charge distribution the so-called equilibrium emittance ε is defined as

$$\varepsilon = \frac{\sigma^2(s)}{\beta(s)} \tag{2.12}$$

where $\sigma(s)$ is the RMS beam size.

2.2 Motion with Momentum Deviation

2.2.1 Dispersion

Particles having different momenta move on different closed orbits because the deflection from the dipoles depends on the particle momentum. The change in position Δu due to a momentum deviation with respect to the position of the reference particle ($\Delta p/p_0 = 0$) is called the dispersion:

$$D_u(s) = \frac{\Delta u}{\Delta p/p_0}. \tag{2.13}$$

Since the bending dipoles deflect horizontally, the dispersion is mainly horizontal. However field and alignment errors introduce some vertical bending resulting in a residual vertical dispersion. The horizontal particle position with respect to the nominal orbit consists of two components, the betatron amplitude $x_\beta(s)$ and a dispersion contribution:

$$x(s) = x_\beta(s) + x_D(s) = x_\beta(s) + D_x(s)\,\frac{\Delta p}{p_0}. \tag{2.14}$$

2.2.2 Momentum Compaction Factor

A particle with $\Delta p/p_0 > 0$ travels on a longer path than the reference particle. The dependence of the relative change in path length $\Delta L/L$ on the momentum deviation $\Delta p/p_0$ defines the momentum compaction factor α_c:

$$\frac{\Delta L}{L} = \alpha_c\,\frac{\Delta p}{p_0}. \tag{2.15}$$

The change in path length for a particle moving on the closed dispersion trajectory $x_D(s)$ is

$$\Delta L = \oint ds\,\frac{x_D(s)}{\rho(s)} = \frac{\Delta p}{p_0}\oint ds\,\frac{D(s)}{\rho(s)}. \tag{2.16}$$

The momentum compaction factor can be rewritten using this equation yielding

$$\alpha_c \; = \; \frac{1}{L} \oint ds \; \frac{D(s)}{\rho(s)}. \tag{2.17}$$

A rough estimate of α_c in terms of the horizontal tune is given by

$$\alpha_c \; \approx \; \frac{1}{Q_x^2}. \tag{2.18}$$

2.2.3 Chromaticity

The focal length of a quadrupole depends on the particle momentum: particles with lower momenta experience a stronger deflection than particles with higher momenta according to eq. (2.3). This leads to a dependence of the tune on the momentum which is described by the chromaticity defined as

$$Q' \; = \; p_0 \, \frac{dQ}{dp} \; \approx \; \frac{\Delta Q}{\Delta p / p_0}. \tag{2.19}$$

The natural chromaticity arising from a linear magnet lattice is given by

$$Q'_u \; = \; - \, \frac{1}{4\pi} \oint ds \; \beta_u(s) \; K(s). \tag{2.20}$$

where u stands for the horizontal or vertical coordinate respectively. An additional contribution to the chromaticity arises from the dipoles (according to eq. (2.5)) which however is negligible for large accelerators ($\frac{1}{\rho^2} \ll k$). In general a superposition of the effects of dispersion and chromaticity is observed for a linear lattice (only dipole and quadrupole magnets), leading to a change of the longitudinal and transverse position of the focal point (see sketch fig. 2.8).
For big accelerators the natural chromaticity is a large quantity ($\mathcal{O}(-150)$ for LEP). In that case the “tune spread” due to the momentum spread of the beam becomes so large that some part of the beam unavoidably hits dangerous resonance lines. Therefore the chromaticity has to be compensated.

2.2.4 Chromaticity Correction with Sextupoles

The chromaticity is corrected using sextupole magnets (see fig. 2.8). A sextupole generates a nonlinear field

$$B_x(x, y) = g' \; x \cdot y \qquad\qquad B_y(x, y) = \frac{1}{2} \; g' \; (x^2 - y^2) \tag{2.21}$$

where g' is related to the current I in the n coils by

$$g' = 6 \; \mu_0 \; \frac{nI}{R^3}$$

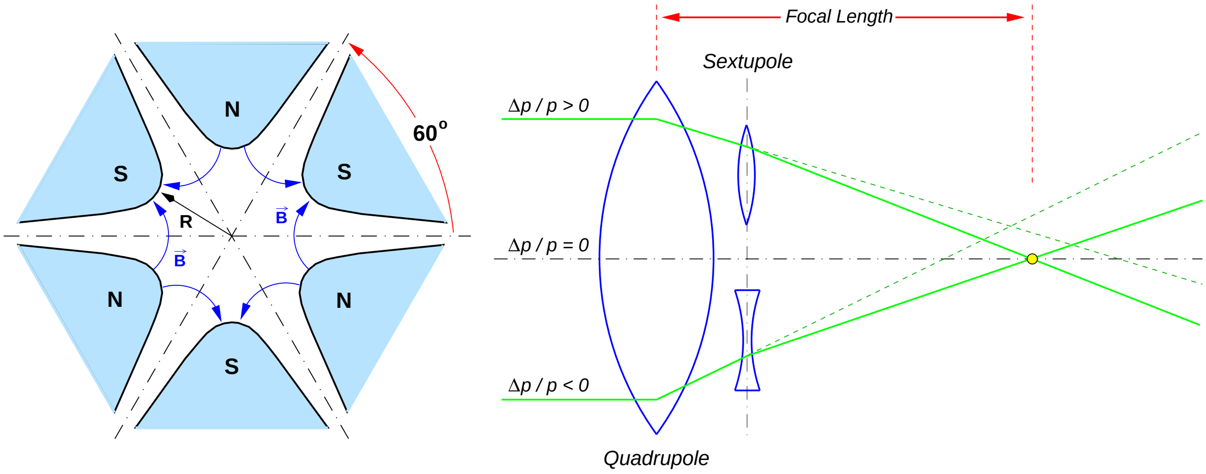

Fig. 2.8: *Sextupole magnet. The left sketch shows a cross-section of a sextupole. The polarity is chosen for a positive charge traveling into the image plane.*
The right sketch displays a chromatic correction with a sextupole magnet: The focusing strength of a quadrupole depends on the momentum of the particle. This chromatic error is corrected by the quadratic field of a sextupole (represented by the additional focusing and defocusing lenses).

with R the distance from the center of the magnet to the pole tip. Like for quadrupole magnets a momentum normalized sextupole strength is defined by

$$m = \frac{e\,g'}{p_0}. \tag{2.22}$$

In the horizontal plane ($y = 0$) the quadratic sextupole fields results in an additional focusing field for particles with $\Delta p/p > 0$ where $\partial B_y/\partial x < 0$ (traveling on the outside of the "ideal" orbit) and in an additional defocusing force for particles with $\Delta p/p < 0$ where $\partial B_y/\partial x > 0$ (see figure 2.8). The focal point is corrected back onto the nominal orbit ($\Delta p/p = 0$). The right hand plot of fig. 2.8 illustrates this.

2.3 Longitudinal Motion

The longitudinal particle motion is determined by the radio frequency (RF) system and the energy loss of the particles. Acceleration of the particles is provided by RF fields whose oscillations are synchronous to the revolution of the reference particle (hence the name "synchrotron"). To meet this synchronization condition the frequency of the RF system must be a multiple of the revolution frequency of the particles

$$f_{RF} = h\, f_{rev} \tag{2.23}$$

where $h \in \mathbb{N}$ is the so-called harmonic number of the accelerator and f_{rev} the revolution frequency. The harmonic number of LEP is 31320, the revolution frequency 11.249 kHz.

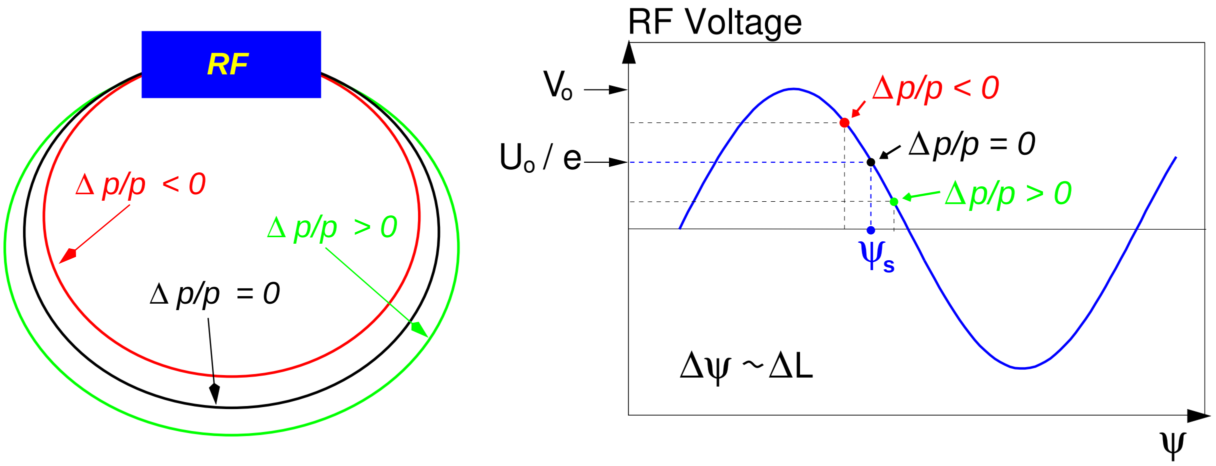

Fig. 2.9: *Change of orbit length for particles with momentum deviation in an accelerator with a single RF cavity (left). Accelerating voltage as function of phase. Particles with different momenta arrive at different phases thus seeing a voltage different from the voltage needed to compensate the nominal energy loss per turn (right).*

2.3.1 Synchrotron Tune and Stable Phase Angle

The accelerating voltage of an RF cavity can be expressed as

$$V(\psi) = V_0 \sin\psi \tag{2.24}$$

where V_0 is the maximum or "peak" voltage provided by the system and ψ the phase. For the derivation of the synchrotron tune it is convenient to consider the case of a single RF cavity as shown in fig. 2.9. A detailed derivation can be found in [7]. A particle with a momentum lower than the reference particle experiences a stronger deflection by the bending magnet resulting in a shorter path length and a change in the arrival phase at the RF unit (see fig. 2.9). In the ultra relativistic regime, the particle arrives earlier and experiences a higher voltage. This effect leads to an oscillation around the phase of the synchronous (reference) particle, ψ_s, where the particle gains an energy equal to the energy loss per turn U_0. If damping due to the emission of synchrotron radiation is negligible, the oscillation equation can be written as

$$\ddot{\psi} + \Omega^2 \psi = 0 \tag{2.25}$$

with the frequency Ω given by

$$\Omega^2 = \omega_{\rm rev}^2 \left(\frac{\alpha_c h}{2\pi E_0}\right) e \frac{dV}{d\psi}(\psi_s) \tag{2.26}$$

where $\omega_{\rm rev} = 2\pi\, f_{\rm rev}$ and E_0 the beam energy. Equation (2.26) implies that $dV/d\psi$ is constant which is valid in the limit of small oscillation amplitudes. The synchrotron tune is defined as the ratio of oscillation frequency Ω and revolution frequency ω_{rev} and can be written as

$$Q_s^2 = \left(\frac{\Omega}{\omega_{rev}}\right)^2 = \left(\frac{\alpha_c h}{2\pi E_0}\right) e\, V_0 \cos\psi_s. \tag{2.27}$$

Using the condition for the stable phase angle $U_0 = e\, V_0 \sin\psi_s$ the synchrotron tune is finally given by

$$Q_s^2 = \left(\frac{\alpha_c h}{2\pi E_0}\right) \sqrt{e^2\, V_0^2 - U_0^2}. \tag{2.28}$$

2.3.2 Synchrotron Radiation

Acceleration of charged particles leads to the emission of synchrotron radiation. The instantaneous synchrotron radiation power is given by

$$P_\gamma = \frac{2}{3} \frac{q^2}{m_0^2 c^3} \frac{\gamma^2}{4\pi\varepsilon_0} \left(\frac{dp}{dt}\right)^2 = \frac{2}{3} \frac{q^2\, c}{4\pi\varepsilon_0} \frac{\gamma^4\beta^4}{\rho^2} \tag{2.29}$$

where the horizontal kick is $\frac{dp}{dt} = \gamma\, m_0\, \frac{v^2}{\rho}$. The local bending radius is ρ, q denotes the particle charge and m_0 its rest mass. Using the following relations

$$r_c = \frac{1}{4\pi\varepsilon_0} \frac{q^2}{m_0 c^2} \qquad C_\gamma = \frac{4\pi}{3} \frac{r_c}{(m_0 c^2)^3} \qquad \gamma = \frac{E}{m_0 c^2} \tag{2.30}$$

where r_c is the classical particle radius and $C_\gamma = 8.86\ 10^{-5}\ \mathrm{m(GeV)^{-3}}$ Sand's synchrotron radiation constant for electrons [12], produces an expression for the instantaneous synchrotron radiation power in more practical units:

$$P_\gamma = \frac{C_\gamma}{2\pi}\, c\, \frac{E^4}{\rho^2}. \tag{2.31}$$

A complete derivation can be found in [7]. Integration of this equation yields the energy loss per turn U_0 of a particle on the ideal orbit with nominal energy E_0:

$$U_0 = \oint P_\gamma dt = \frac{C_\gamma E_0^4}{2\pi} \oint \frac{ds}{\rho(s)^2}. \tag{2.32}$$

For an isomagnetic lattice with $\rho(s) = \rho$ inside all magnets and $\rho(s) = \infty$ elsewhere, the energy loss per turn can be simplified to

$$U_0 = \frac{C_\gamma}{\rho} E_0^4 \tag{2.33}$$

2.3.3 Radiation Damping

Radiation damping occurs due to continuous energy loss into synchrotron radiation. Damping of energy deviations originates from an energy dependence of the radiation. In the transverse plane damping comes from the loss of transverse momentum with the emission of photons while the RF system replenishes only the longitudinal momentum. Damping and quantized emission of synchrotron radiation determine the equilibrium energy spread of the beam.

Betatron and synchrotron oscillation amplitudes are damped exponentially with time like $A_i = A_{i,0}\, e^{-\,t/\tau_i}$ where $i = x, y, \varepsilon$. The index "ε" indicates an oscillation in the longitudinal coordinate. The damping decrements τ_i^{-1} depend on beam energy E_0 and energy loss per turn U_0:

$$\tau_i^{-1} = \frac{1}{2}\,\frac{U_0\, f_{rev}}{E_0}\, J_i \tag{2.34}$$

where J_i are the so-called damping partition numbers defined by

$$\begin{aligned} J_x &= 1 - \mathcal{D} \\ J_y &= 1 \\ J_\varepsilon &= 2 + \mathcal{D} \end{aligned} \tag{2.35}$$

with Robinson's sum rule [13]

$$\sum_i J_i = 4 \tag{2.36}$$

and the damping parameter $\mathcal{D}$ defined as follows:

$$\mathcal{D} = \frac{\oint ds\, \frac{D(s)}{\rho(s)} \left(2k(s) + \frac{1}{\rho^2(s)}\right)}{\oint \frac{ds}{\rho^2(s)}}$$

where $D(s)$ is the (horizontal) dispersion function and $k(s)$ the quadrupole strength. The damping parameter does not depend on energy, only on the chosen lattice. The contribution of $\mathcal{D}$ to the damping is only non-zero for non-central orbits. As an implication of eq. (2.36) the total amount of damping is a constant. However it is possible to redistribute the damping between the horizontal and the longitudinal plane by changing the damping parameter. This can be achieved by an RF frequency shift Δf_{RF} since the damping parameter can be written as

$$\mathcal{D} = \frac{1}{\alpha_c}\,\frac{dJ_x}{dp/p_0}\,\frac{\Delta f_{RF}}{f_{RF}}. \tag{2.37}$$

2.3.4 Impedance

A high intensity bunch acts as a source of electro-magnetic fields. The beam surroundings (vacuum chambers, cavities, etc.) alter these fields which can act back on the beam (see fig. 2.10). This feedback loop can cause shifts of the betatron and synchrotron oscillation frequencies of the beam and a resonant increase of small beam disturbances, i.e. instabilities. These phenomena are called collective effects since they are caused by the collective action of the particles in a bunch.

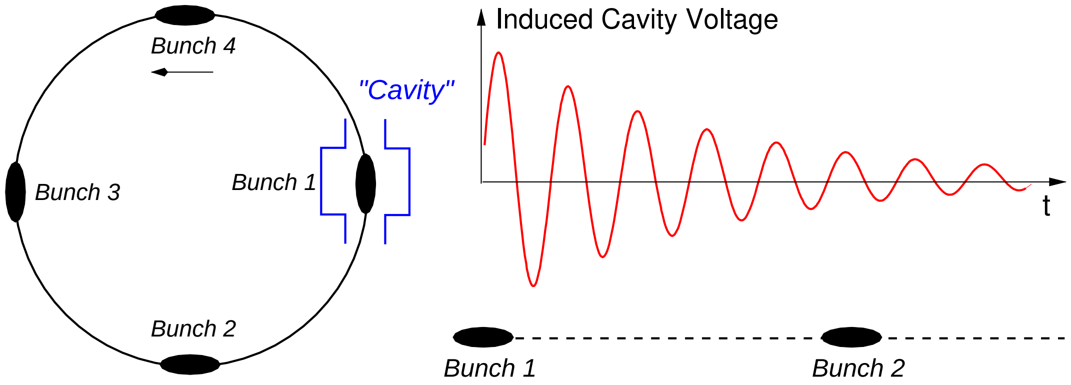

Fig. 2.10: *Illustration of the feedback mechanism in presence of an impedance. The slowly decaying induced field may act back on the generating bunch, influence the next bunch or even the same bunch on the next turn for a very slow decay.*

The impedance $Z(\omega)$ of an accelerator element is defined as the ratio of the voltage V induced in the element and the circulating current I: $Z(\omega) = V(\omega)/I(\omega)$. The impedance is a function of the excitation frequency ω and in general a complex number. The resistive part of the impedance $\mathrm{Re}Z(\omega)$ leads to energy losses while the reactive component $\mathrm{Im}Z(\omega)$ causes frequency shifts. The additional energy losses in the longitudinal plane are due to a voltage induced by the charged particles when passing an impedance. In the transverse planes a beam traveling off-center through an object generates deflecting forces which act back on the transverse motion.

Chapter 3

High Energy Optics

A central parameter of an accelerator is its luminosity. For a storage ring the luminosity can be written as

$$\mathscr{L} = \frac{I_+ \, I_-}{4\pi \, e^2 \, f_{rev} \, n_b \, \sigma_x \sigma_y} \tag{3.1}$$

with $I_\pm$ the total positron and electron currents, n_b the number of bunches per beam and σ_x and σ_y the horizontal and vertical beam sizes at the interaction point (IP). At LEP the vertical beam size varies between 2 and 6 μm, the horizontal beam size between 100 and 350 μm. The horizontal and vertical beam sizes depend on the value of the respective β-function at the IP and on the beam energy. Typical total beam currents are 4 to 6 mA. During the LEP1 phase the machine was operated with a $90^o/60^o$ optics. This optics guaranteed a stable running with high luminosities. The horizontal beam size scales as

$$\sigma_x^2 \; \propto \; \beta_x^* \, \frac{E_0^2}{J_x \, Q_x^3} \tag{3.2}$$

where β_x^* is the value of the horizontal β-function at the interaction point. To counteract an increase of beam size with energy either β_x^* has to be decreased or J_x and Q_x have to be increased. To reduce β_x^* the focusing strength of the quadrupoles at both sides of the experiments has to be increased which effectively leads to larger beam sizes in these quadrupoles. Since the energy loss from synchrotron radiation in quadrupoles is proportional to the beam size (eq. (7.7)) the stronger focusing leads to higher synchrotron radiation backgrounds in the experiments. The reduction of β_x^* is therefore limited by the requirements of the detectors. The increase of the horizontal damping partition number J_x (effectively a redistribution of damping, see eq. (2.35)) is limited by the energy acceptance of the machine since it leads to an increase of the energy spread. A very effective option to reduce the beam size is therefore to increase the tune Q_x using a lattice with higher phase advance. Higher phase advance however implies stronger quadrupole and sextupole fields. The nonlinear sextupole fields can induce an-harmonic oscillations, particularly if the distribution of the sextupoles is not optimal. A too strong dependence of the tune on the

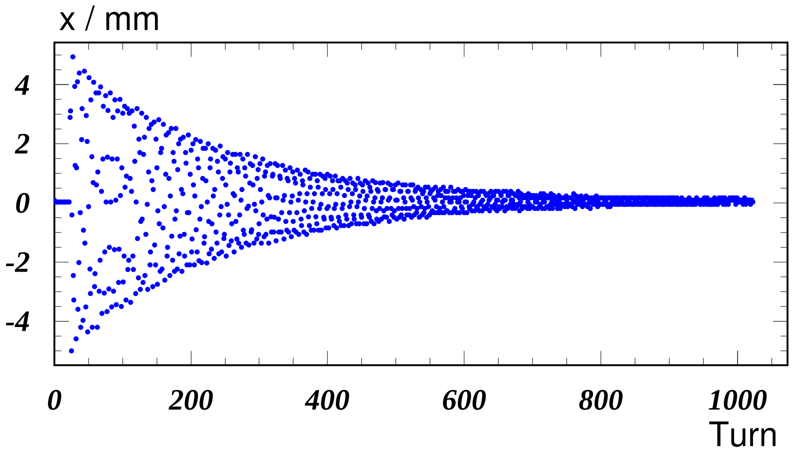

Fig. 3.1: *Center-of-charge position of a bunch versus turn number at an arc monitor. The kick and the subsequent damped oscillation are clearly visible.*

amplitude can drive particles on resonances and lead to particle losses. The *dynamic aperture* of a machine is defined as the maximum (phase-space) amplitude within which particles do not get lost as a consequence of single-particle-dynamics effects [14]. Ideally the dynamic aperture of a lattice should be larger than the *physical aperture* given by the vacuum chamber, in reality this is not always possible.

At LEP2 several lattices with a higher horizontal phase have been tested [15–18]: A $108^o/60^o$ optics had a too small aperture and a $108^o/90^o$ lattice had a large anharmonicity giving problems with resonances. Other lattices with even higher horizontal phase advances like a $135^o/60^o$ and a $131^o/90^o$ optics could only accumulate bunch currents of a few μA. Finally a $102^o/90^o$ optics was chosen for LEP2 since this optics was very stable and easy to operate. The dynamic aperture has turned out to be an important issue for the stability of an optics. This chapter concentrates on discussion and measurement of one parameter which is of importance for the understanding of the dynamic aperture of a machine optics: the horizontal detuning with amplitude or anharmonicity.

3.1 Damped Coherent Oscillations

The dependence of the tune on the particle amplitude (or detuning with amplitude) can be determined from an analysis of “1000-turn” measurements [19]. A coherent horizontal oscillation is excited by a single kick and the center-of-charge position of the bunch is observed over 1024 consecutive turns (fig. 3.1). The bunch positions along the ring are determined with 504 beam position monitors (BPMs, “pickups”) located near the horizontally defocusing quadrupoles (see fig. 3.2). The position data are recorded for each bunch and both beams separately. Each LEP BPM consists of four buttons as can be seen in figure 3.2. When a charged beam passes between two parallel conductors (or pickups), it induces a difference voltage on the plates which

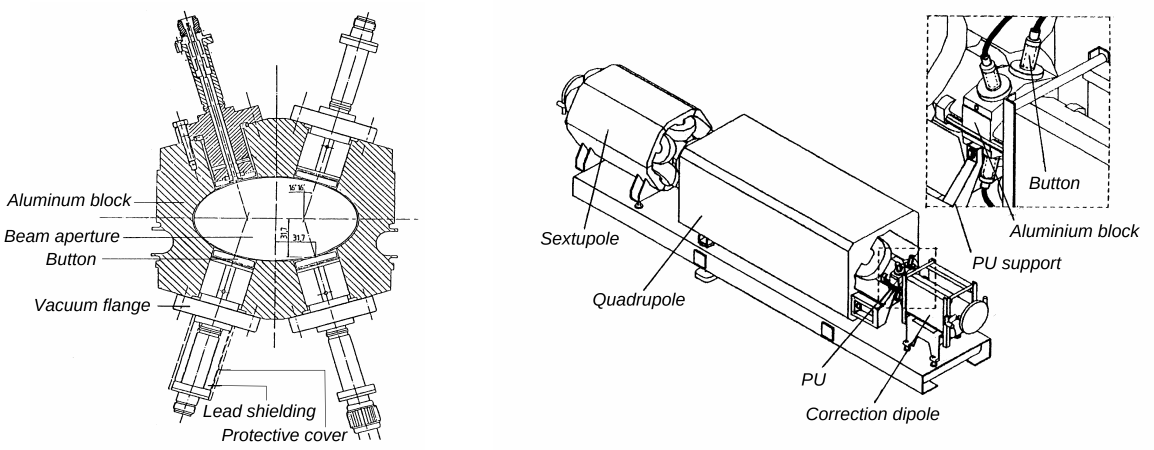

Fig. 3.2: *Cross section of a LEP four button beam position monitor (left). Location of a BPM near a quadrupole (right).*

is proportional to the displacement of the center of the beam with respect to the center of the plates. The LEP button electrodes are displaced with respect to the median plane in order to avoid destruction by synchrotron radiation. Combination of the signals of the four electrodes allows a position determination in both transverse planes.

Figure 3.1 shows a 1000-turn measurement for one BPM with the $102^o/90^o$ optics. The moment of the kick is clearly visible. A phase space representation of the same dataset is shown in figure 3.3 where the horizontal center-of-charge position of a bunch at two BPMs A and B with a distance of approximately 90^o in phase is plotted. For that case the Courant-Snyder invariant W was calculated from the measured positions at the two BPMs as mentioned in section 2.1.5:

$$W = \frac{1}{\beta_0}\left(x_A^2 + x_B^2\right) \tag{3.3}$$

Due to the damping of the oscillation the amplitude of the oscillation and with it W decreases from turn to turn. A Fourier analysis of the time evolution of W reveals the tune components (fig. 3.3). For this thesis the method of Lomb [20] was chosen to evaluate the power spectrum. Lomb's method performs a harmonic analysis of an arbitrary data sample without any constraints on the number of data points and the sampling times in contrast to the well established "Fast Fourier Transform" (FFT) [21]. It weights the data on a "per point" basis instead of on a "per time interval" basis like FFT methods. For N data points h_i measured at times t_i the so-called "Lomb normalized periodogram" $P_N(\omega)$ is defined by

$$P_N(\omega) = \frac{1}{2\sigma^2}\left\{\frac{\left[\sum_j d_j \cos(\omega(t_j-\tau))\right]^2}{\sum_j \cos^2(\omega(t_j-\tau))} + \frac{\left[\sum_j d_j \sin(\omega(t_j-\tau))\right]^2}{\sum_j \sin^2(\omega(t_j-\tau))}\right\} \tag{3.4}$$

with

$$d_j = h_j - \frac{1}{N}\sum_{i=1}^{N} h_i, \qquad \sigma^2 = \frac{1}{N-1}\sum_{i=1}^{N} d_i^2, \qquad \tan(2\omega\tau) = \frac{\sum_j \sin(2\omega t_j)}{\sum_j \cos(2\omega t_j)}.$$

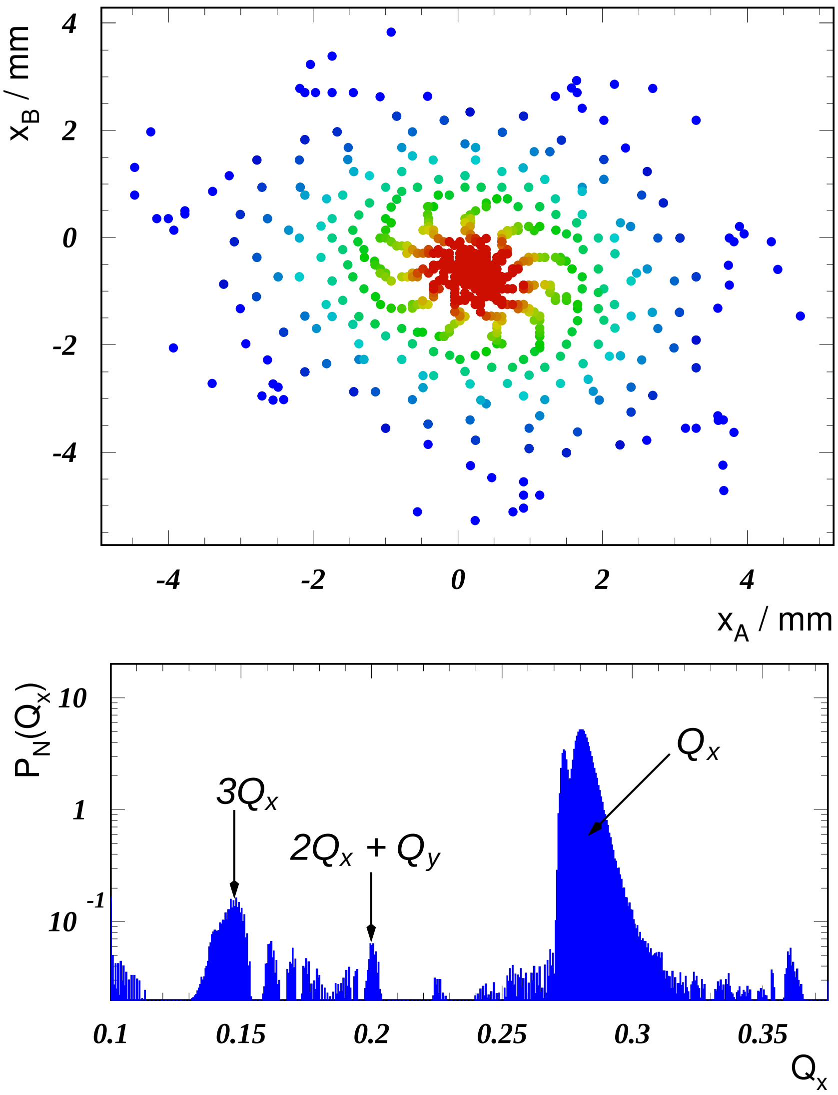

Fig. 3.3: *Upper plot: Center-of-charge position of a bunch after a kick at two BPMS with a distance of 90° in phase. Lower plot: "Lomb normalized periodogram"* $P_N(Q_x)$ *(see text) of the time evolution of the Courant-Snyder invariant W calculated with eq. (3.3) from the measured positions. The detuning with amplitude is clearly seen on the width of the* Q_x *peak. The third order resonances* $3\ Q_x$ *and* $2\ Q_x + Q_y$ *are also visible.*

This implies that for any test frequency ω (or tune Q_x in the case treated here) the content of that frequency in the given dataset is evaluated. The constant τ is constructed to make the value $P_N(\omega)$ independent of the phase of the original harmonic.
The bottom plot of fig. 3.3 shows such a Lomb normalized periodogram $P_N(Q_x)$ of the W calculated according to eq. (3.3) for the horizontal tune. The individual tune components are visible. The width of the Q_x peak is a direct indication of the change in horizontal tune with amplitude in the 1000-turn sample.

3.1.1 Measuring the Damping Time

The damping time τ of the coherent oscillation in units of the revolution can be determined by fitting the model of an exponentially damped oscillation with a frequency depending on the square of the amplitude to single BPM 1000-turn data. The position change at one location is parameterized as follows:

$$
\begin{gathered}
x(t) \;=\; x_0 \;+\; A_0\, e^{-t/\tau}\, \sin\left(2\pi\, \Phi(t) \;+\; \varphi\right) \\
\text{with} \\
\Phi(t) \;=\; \int_0^t dt' \left(Q_0 \;+\; \alpha_q\, A_0^2\, e^{-2t'/\tau}\right) \;=\; tQ_0 \;+\; \frac{\tau}{2}\, \alpha_q\, A_0^2 \left(1 \;-\; e^{-2t/\tau}\right)
\end{gathered}
\tag{3.5}
$$

where t is the turn number, A_0 the value of the amplitude at $t = 0$, x_0 the horizontal position offset at that pickup, φ a phase offset, α_q an effective detuning coefficient which includes a normalization to the local β-function and Q_0 the unperturbed horizontal tune. The dependence of the frequency of the oscillation on the square of the amplitude is due to the nonlinear nature of the sextupole fields. Figure 3.4 shows such a "global" fit. The first plot shows the measured data, the second one the results of the fit and the third an overlay of measurement and fit results. The last plot of fig. 3.4 shows the fit residuals. Obviously the damping behavior is very well reproduced by the fit model. The fit range is chosen to have a sufficiently large oscillation amplitude over the full range. In tests with datasets generated with the MAD (**M**ethodical **A**ccelerator **D**esign) simulation program [22] the fitting procedure performed reliably and reproduced the input damping times. The program package MAD is widely used for accelerator studies and design. MAD provides powerful tools for studies, design and diagnostics of charged-particle optics in accelerators and has been developed at CERN. Although it is necessarily based on a simplified model of the ring (for example rectangular magnets without fringe fields and without higher order multi-pole components and field errors) it generally reproduces relevant quantities reliably.

3.2 Horizontal Detuning with Amplitude

The global fit described in the previous section describes the damping behavior well but it lacks the numerical stability to extract a reliable value of the anharmonicity. Therefore a series of fits is needed to extract the horizontal detuning with amplitude from the 1000-turn datasets. Using the damping time determined with the global fit, the tune evolution with time is extracted by fitting exponentially damped harmonic oscillations according to eq. (3.5) to subsamples of 50 turns, this time keeping the initial amplitude A_0 fixed and assuming a constant tune over the subsample. The results of such fits to the data of fig. 3.1 are shown in fig. 3.5 where the resulting tune is plotted as a function of the turn number.

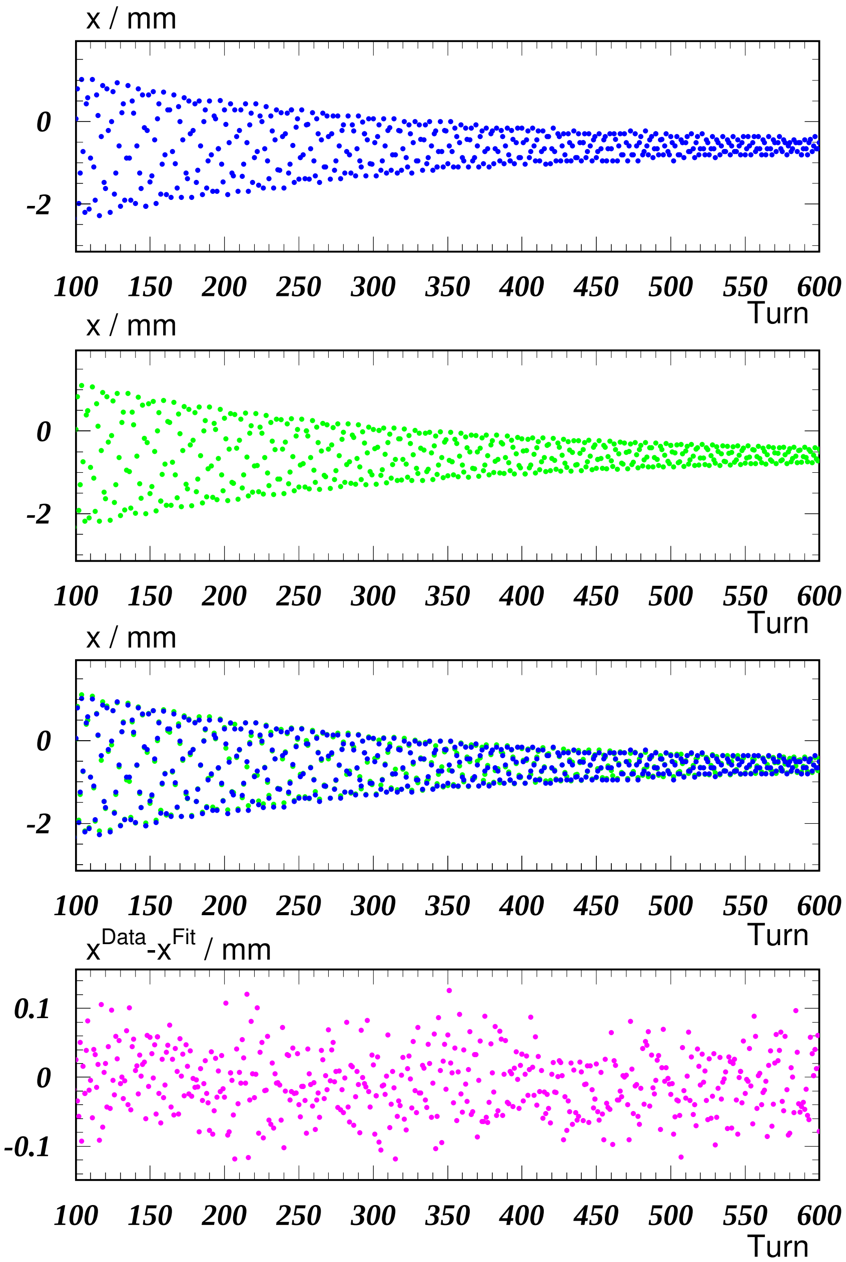

Fig. 3.4: *Center-of-charge position of a bunch versus turn number at an arc monitor. The upper two plots show data and the results of a "global" fit to the oscillation. The third plot is an overlay of data and fit results and the fourth shows the difference.*

The horizontal detuning with amplitude $(\partial Q_x/\partial W_x)$ can be derived from the dependence of the tune Q on the Courant-Snyder invariant W. The latter can be calculated using the measured damping time τ and the initial amplitude

$$W = \frac{A^2}{\beta} = \frac{1}{\beta} A_0^2 \, e^{-2t/\tau} \tag{3.6}$$

since A denotes the oscillation amplitude at a given t. Figure 3.6 shows the relation between tune

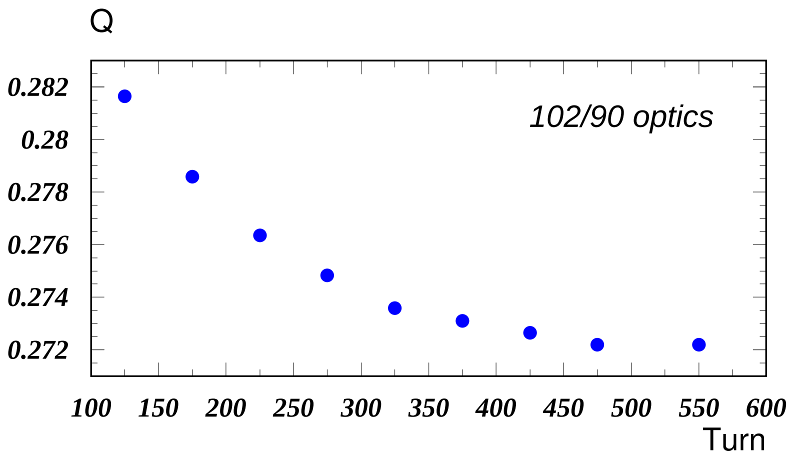

Fig. 3.5: *Tune evolution corresponding to the damped bunch oscillation shown in figure 3.1.*

Q and Courant-Snyder invariant W for one BPM. The apparent curvature for this particular measurement is absent in other measurements. Since

$$Q = Q_0 + \frac{\partial Q_x}{\partial W_x} W_x, \tag{3.7}$$

the slope $\partial Q_x / \partial W_x$ gives the detuning with amplitude. This analysis is applied to all 240 beam position monitors of the arcs in order to improve the statistics for a reliable measurement. Averaging over all arcs also cancels periodic perturbations like β-beating. The statistical error is given by the standard deviation of all single measurements divided by the square root of the number of measurements ($\sigma/\sqrt{N}$). Simulation studies of the systematic error with the MAD simulation program show that the method is reliable.

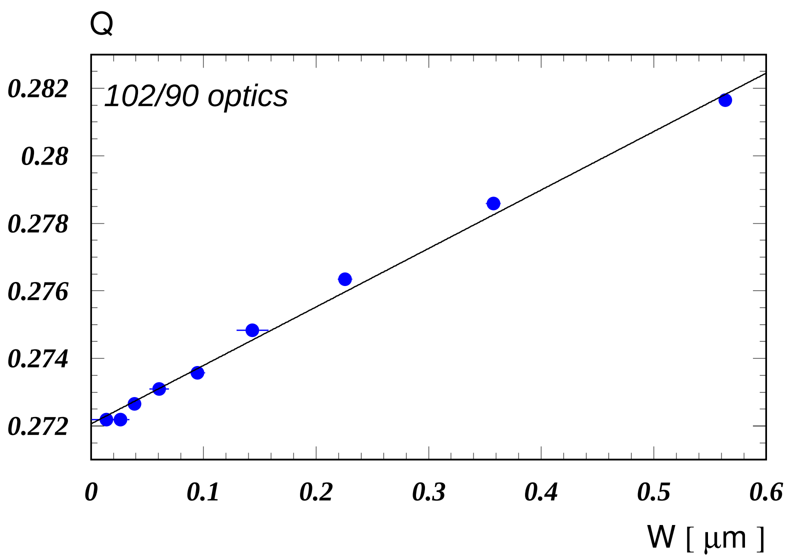

Fig. 3.6: *Tune as function of Courant-Snyder invariant for the data sample shown in fig. 3.1 and fig. 3.5 (the straight line is a fit to the data).*

3.3 Systematic Studies

To quantify the systematic uncertainty of this method, several effects have been considered like the dependence of the analysis on the damping time, on the tune spread and on binning effects in the tune evaluation.

To study a possible bias due to damping time and to verify the method it has been applied to datasets generated with MAD for several energies (and for all optics in question). The resulting bias due to damping time is small compared to the measurement error for all analyzed datasets. Furthermore the numerical results of this method are in good agreement with values predicted with MAD.

An estimate of the systematic error due to a tune spread was obtained by comparing datasets with identical bunch currents but different chromaticities. As the tune spread due to chromaticity ($\mathcal{O}(10^{-2})$) is about ten times larger than the tune spread due to natural emittance ($\mathcal{O}(10^{-3})$) this estimate yields an upper limit for the uncertainty caused by the tune spread. The influence of the chromaticity on the damping times is discussed later (see chapter 5 - fig. 5.2 for example shows damping rate determinations for different chromaticities at 45 GeV). The contribution to the systematic error on $\partial Q_x/\partial W_x$ is about 0.7 10^3/ m.

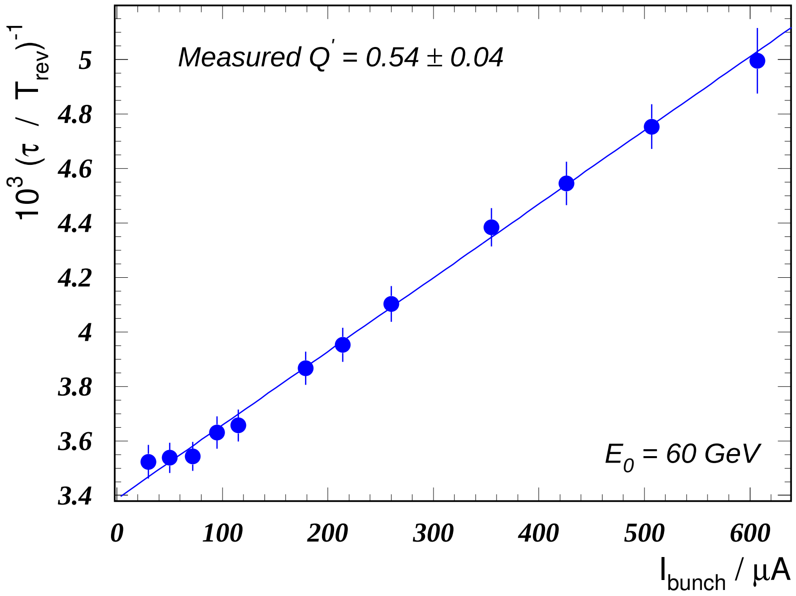

Fig. 3.7: *Damping rate as function of bunch current for a beam energy of 60 GeV and a measured chromaticity of $Q' = 0.54 \pm 0.04$. The linearity of the measured damping rate as function current indicates that filamentation effects do not play an important role for the used bunch currents. The revolution period is $T_{rev} =$ 88.9 μs. The results are based on turn by turn measurements.*

The influence of the size of the slices used for the fits in the tune evaluation has been studied by repeating the analysis on MAD datasets for a larger number of bins (18 instead of 9). The total systematic uncertainty is given by the spread of the results of all studies described above.

Since the anharmonicity is a single particle quantity and the measurements can be done for the center-of-charge only, it is important that the center-of-charge is representative of the single particle motion. This approximation is valid if the phase space is not filamented. The filamentation phenomenon keeps the local total phase space occupied by the beam constant while changing the originally elliptic boundary thus leading to larger effective beam sizes without actually increasing the phase space density. In this kind of configuration the tune change observed on the center-of-charge may not be an appropriate measure for the tune changes of the individual particles of the bunch. The probability for filamentation is expected to increase towards smaller bunch currents. However for the measurements presented here no filamentation effect was observed down to the smallest measurable currents and the decay of the oscillation is perfectly exponential. In addition filamentation is expected to vanish in the head-tail (see chapter 5) dominated regime [23, 24]. Figure 3.7 shows that the measured damping time over a wide range of bunch currents has a linear behavior which is the expectation for head-tail damping. In general the head-tail effect is the dominating damping mechanism in the datasets used for the detuning analysis.

3.4 Results

Datasets for several optics have been analyzed. The results are shown in tab. 3.1 and fig. 3.8. The histograms of fig. 3.8 represent the distributions of measurements for all arc monitors. The distributions have a Gaussian shape and are clearly separated. The plots show measurements

Optics	$\partial Q_x/\partial W_x$ [10^3/m]	
	MAD	Measured
$90^o/60^o$ (physics)	1.7	6.2 ± 0.8
$102^o/90^o$ (physics)	7.0	7.2 ± 1.0
$108^o/90^o$ (physics)	25.0	34.0 ± 1.0
$102^o/90^o$ (physics 97)	12.2	10.6 ± 1.2
$102^o/90^o$ (Δ KSF1/2 = ± 0.082)	12.5	18.8 ± 1.2
$102^o/90^o$ (Δ KSF1/2 = ± 0.165)	30.4	38.1 ± 1.3

Tab. 3.1: *Measured and predicted horizontal detuning with amplitude for LEP physics optics and two experimental optics where the sextupole strengths (KSF) had been changed by different amounts while keeping the chromaticity constant. The errors include statistical and systematic uncertainties.*

for the LEP physics optics and two experimental optics where the sextupole strengths (KSF) had been changed by different amounts while keeping the chromaticity constant. The correlation between the strength of the sextupole magnets and the horizontal detuning with amplitude is clearly visible. The measurement of the 1997 physics version of the $102^o/90^o$ optics shows a remarkably large spread. This is explained by the higher beam energy of 87 GeV for this measurement. Due to the higher beam energy the damping time is shorter and therefore the fit range and resolution are drastically reduced. Figure 3.9 gives an overview of the detuning measurements for the different optics. It shows the measured detuning with amplitude as function of the MAD expectation. Although the measured value is usually larger than the predictions for a perfect machine there is a reasonable agreement between measurements and predictions. A more detailed description of this topic can be found in [25].

3.5 Optimization of the Detuning

The sextupoles are grouped in so-called "families" which are powered together. The precise arrangement of these families depends on phase advance and must be chosen carefully to avoid a systematic excitation of resonances. Three sextupole families can be used to optimize the chromaticity and tune shifts with amplitude in the horizontal plane [26]. The detuning can be trimmed around its nominal value by changing the strength m ("KSF") of sextupole families in opposite directions while keeping the chromaticity constant ($N_1\, m_1 + N_3\, m_3 = \text{const.}$ where N_1 and N_3 are the number of sextupoles in the families). The horizontal detuning with amplitude has been measured for several such settings of the sextupoles. Figure 3.10 shows that the detuning can be changed in a controlled way. The measurement errors are smaller than the size of the symbols and the systematic uncertainty is shown.

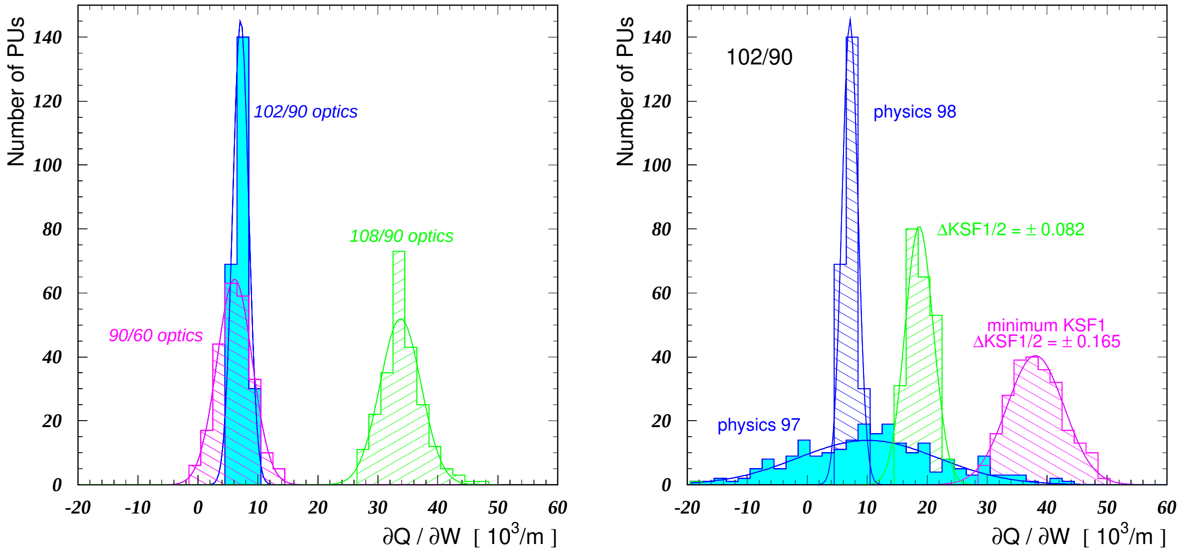

Fig. 3.8: *Distribution of the 240 arc pickups (PUs) as function of horizontal detuning with amplitude for the LEP physics optics with horizontal/vertical phase advance in the arcs of 90/60, 102/90 and 108/90 degrees (left) and the $102^o/90^o$ optics with different sextupole configurations (right).*

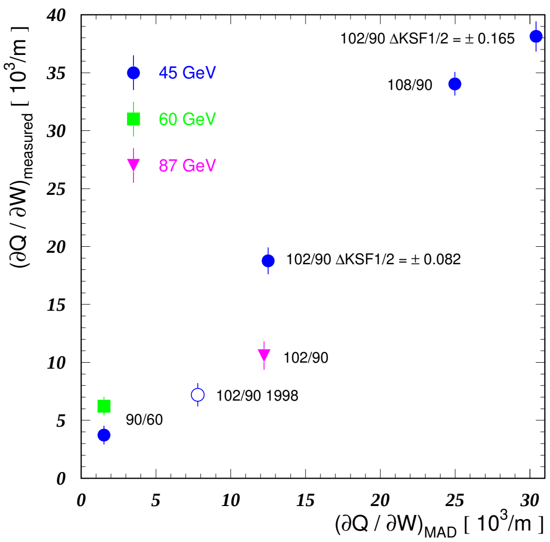

Fig. 3.9: *Measured horizontal detuning with amplitude as function of the* MAD *prediction for various optics.*

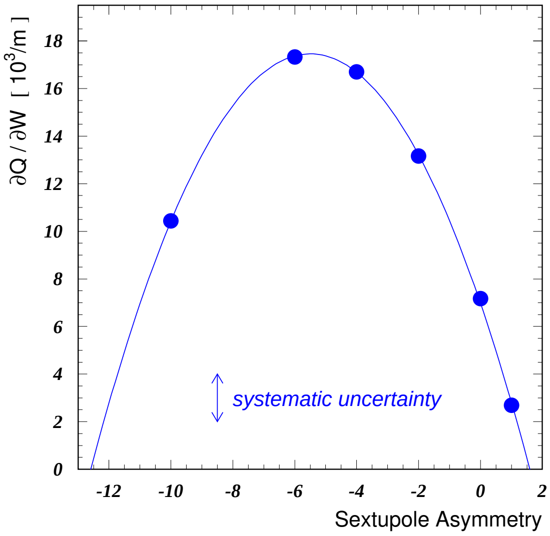

Fig. 3.10: *Measured horizontal detuning with amplitude for different sextupole settings. Measurement errors are smaller than the size of the symbols. The size of the systematic error is given.*

Chapter 4

Energy Calibration

The precise measurements of the Z and the W boson masses require an excellent knowledge of the center-of-mass energy at the interaction points. The average beam energy for ultra-relativistic particles is in a good approximation defined by the bending field along the closed orbit:

$$E_0 = \frac{ec}{2\pi} \oint ds\ B(s). \tag{4.1}$$

For a beam energy of 45 GeV the integral over the bending field is about 10^3 Tm. The most precise average beam energy measurement is based on the technique of resonant depolarization. For the energy calibration in the LEP1 phase relative accuracies of 10^{-5} have been achieved. However, this technique works only in the low energy regions, for the LEP2 phase extrapolation

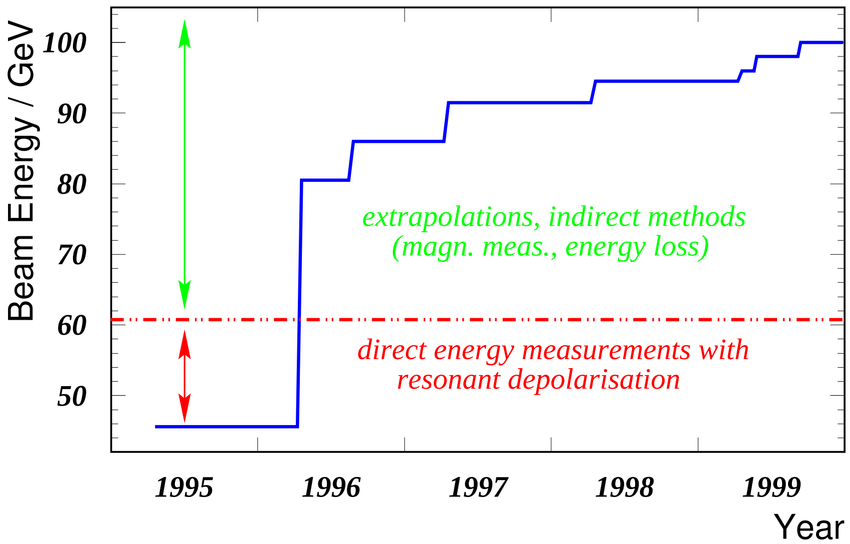

Fig. 4.1: *Beam energy of LEP as function of time. The transition to the LEP2 phase is clearly visible.*

methods have to be used to obtain the beam energy. Figure 4.1 shows the evolution of the maximum LEP beam energy over the years. The local energy may deviate from the measured average as the particles lose energy due to synchrotron radiation and gain energy from the RF system. This has to be taken into account as well as any difference in energy of the electron and positron beams. The change in center-of-mass energy has to be evaluated with adequate models.

This chapter describes the techniques used for LEP2 energy calibration. The different contributions and corrections are discussed shortly. A detailed description of energy calibration at LEP can be found in [27, 28].

4.1 Energy Calibration by Resonant Depolarization

4.1.1 Transverse Polarization

The quantum nature of synchrotron radiation leads to the buildup of transverse polarization in e^+e^- storage rings which was first described by Sokolov and Ternov [29]. The spin-flip probability due to the emission of synchrotron radiation is very small but has an asymmetry favoring the orientation of the magnetic moment parallel to the vertical magnetic field of the bending magnets. The maximum achievable level of transverse polarization for an ideal storage ring is given by the size of the asymmetry term and amounts to $8\ /\ 5\sqrt{3} \approx 92.4$ %. Initially the polarization level increases exponentially with time with a build up time of

$$\tau_p = \frac{8}{5\sqrt{3}} \frac{m_0^6\, c^{10}\, \rho^3}{\hbar\, r_c\, E_0^5} \tag{4.2}$$

where m_0 is the electron rest mass, r_c the classical particle radius and ρ the bending radius. For a beam energy of 46 GeV the build up time for polarization at LEP is 310 minutes.

The motion of the spin vector $\vec{s}$ of a relativistic electron in the presence of electric and magnetic fields $\vec{E}$ and $\vec{B}$ is described by the Thomas-BMT (Bargmann, Michel, Telegdi) equation [30, 31]:

$$\frac{d\vec{s}}{dt} = \vec{\Omega}_{\mathrm{BMT}} \times \vec{s}. \tag{4.3}$$

The spin precession frequency $\vec{\Omega}_{\mathrm{BMT}}$ can be written as

$$\vec{\Omega}_{\mathrm{BMT}} = -\frac{e}{\gamma m_0}\left[(1+a\gamma)\,\vec{B}_\perp + (1+a)\,\vec{B}_{||} - \left(a\gamma + \frac{\gamma}{1+\gamma}\right)\vec{\beta} \times \frac{\vec{E}}{c}\right] \tag{4.4}$$

as function of the components of the magnetic field perpendicular and parallel to the velocity $\vec{\beta}c$ of the particle $\vec{B}_\perp$ and $\vec{B}_{||}$ and the plane created by velocity and the electrical field. The factor a is given by $a = (g_e - 2)/2 = 0.001159652193(10)$ [32]. The average over all particles of the number of spin oscillation per revolution is defined as the spin tune $\nu = a\,\gamma$. The spin tune is proportional to the beam energy E_0.

In a real accelerator depolarizing resonances reduce the maximum polarization level. Also the buildup of transverse polarization at LEP during regular physics runs is prevented by effects due to beam-beam interaction. For high energies the maximum polarization level is further reduced by a large energy spread and strong synchrotron spin resonances. Figure 4.2 shows how the

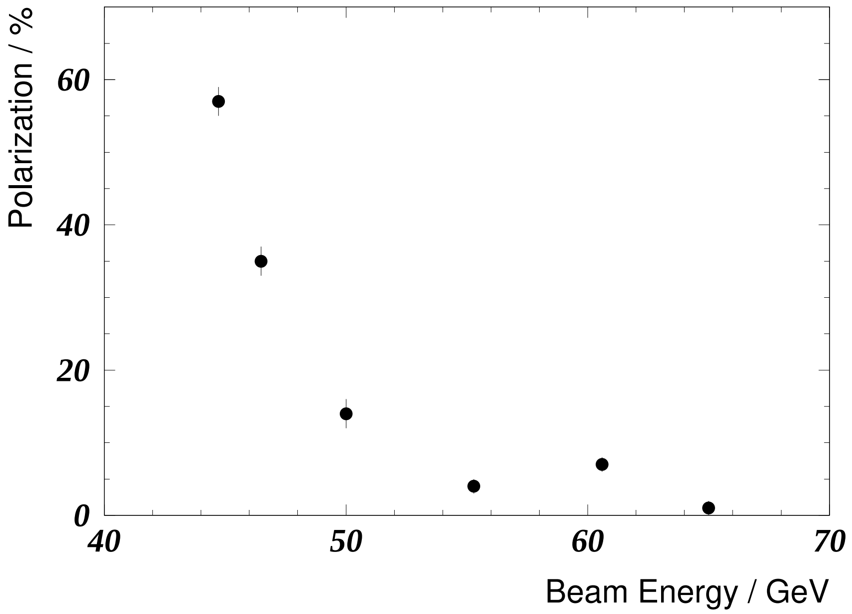

Fig. 4.2: *Maximum observed polarization level at LEP as a function of beam energy [11].*

maximum observed polarization level decreases with the beam energy. Up to now no significant polarization has been seen above 60 GeV.
Compton scattering of circularly polarized laser light is used to measure the level of the vertical polarization [33, 34]. The 532 nm wavelength laser pulses of a frequency doubled Nd-Yag laser operated close to 100 Hz are scattered under a small angle (3 mrad) on the particle bunches. Laser and beam polarization determine the distribution of the back-scattered photons. A Silicon strip and tungsten plates calorimeter located about 300 m downstream of the collision point detects the vertical profile of this distribution. By flipping the circular polarization of the laser beam the center-of-gravity position of the showers induced by the back-scattered photons is shifted proportionally to the polarization level of the beam.

4.1.2 Resonant Depolarization

The relation between spin tune and beam energy can be used to determine the average energy of a transversely polarized beam. To measure the spin precession frequency an RF-magnet with a field perpendicular to the bending field rotates the spins by small amounts. For a certain phase relation between the kicks of the magnet and the spin tune the small spin rotations add up coherently from turn to turn and the polarization is destroyed. The resonance condition for spin rotations is

$$f_{dep} = (k \pm [\nu]) \cdot f_{rev} \tag{4.5}$$

where f_{rev} is the revolution frequency and k an integer. The non-integer part of the spin tune is represented by $[\nu]$. To determine the spin tune, the frequency of the RF-magnet kicks is slowly varied with time over a given frequency range. If a depolarization occurs during such a scan, spin tune and beam energy can be determined from the corresponding frequency bin. This method is usually referred to as "energy calibration by resonant depolarization" (RDP).

4.2 Magnetic Extrapolations

For the energies of the LEP2 phase a direct energy calibration by resonant depolarization is not possible because the transverse polarization does not build up for these energies. Therefore the beam energy calibration has to be extrapolated from measurements at low energies. Equation (4.1) describes the dependence of the beam energy on the total bending field. It therefore seems natural to use measurements of the magnetic field at energies between 41 and 60 GeV cross-calibrated with resonant depolarization to predict the energy in physics conditions. In the following the magnetic measurement devices used in the process of energy calibration are described shortly. A detailed description can be found in [28].

4.2.1 NMR Probes

Since 1996 the dipole field is continuously monitored by NMR probes [35]. These probes measure the magnetic field by **n**uclear **m**agnetic **r**esonance (NMR). The location of such a probe in a

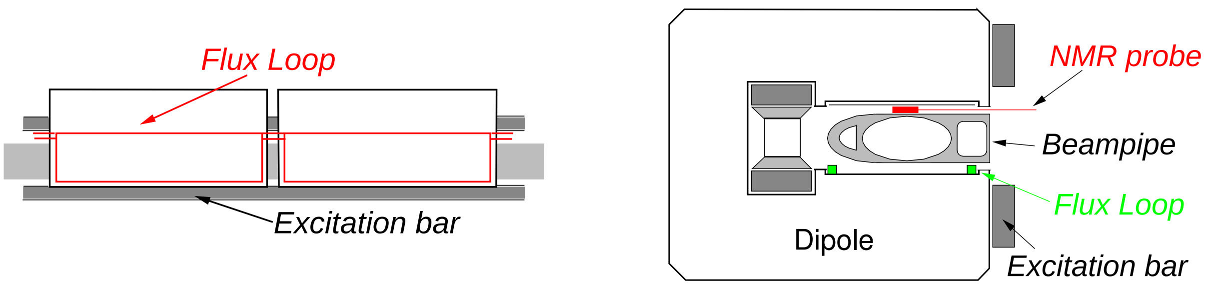

Fig. 4.3: *Location of magnetic measurement devices in the LEP dipole magnets (lengths don't scale). Left: Top view of a pair of dipole magnets, indicating also the layout of the flux loop cables inside the magnet. Right: Cross section of a dipole with NMR probe and flux loop cables.*

dipole magnet can be seen in the right plot of fig. 4.3. Sixteen NMR probes were installed in the arc sections of LEP in 1997 to track the bending field. These measurements however sample the bending field only at a few distinct locations which may not be entirely representative of the total field.

4.2.2 Flux Loop

Besides the local field measurements a *flux loop* system is installed in the LEP dipole magnets to measure the average bending field. Induction coils are located in all regular dipoles (see fig. 4.3) and are used to measure the magnetic field change during magnet cycling. The flux loop covers in total 96.5 % of the bending field.

4.2.3 Extrapolation to High Energy

To evaluate the beam energy in physics conditions, the magnetic field measurements are first calibrated with resonant depolarization between 41 and 60 GeV. The standard procedure used for the final energy files is described in detail in [27, 28]. An alternative method which was used to produce all energies derived from measurements of the magnetic field quoted in this thesis, is described here. As the NMR probes provide local measurements, the absolute field level depends on the exact location of the probe and may vary by a few permille. Some probes have systematically high or low readings. Missing measurements from a probe (essentially due to a failure caused by synchrotron radiation damage) with such a systematically shifted reading can lead to a significant bias of the average field. A normalization of the individual readings to the integral measurement of the flux loop should help to avoid this bias and reduce the scatter. To perform such a normalization of the NMR to the flux loop measurements, the fields of both instruments are recorded in dedicated experiments without beam as a function of the magnet current, respectively the machine energy ("dipole energy"). The coefficients for the normalization are obtained from fits flux loop versus NMR according to $B_{FL} = a^i \; B^i_{NMR} + b^i$ for each NMR probe. The thus normalized measurements of all sixteen NMR probes installed in LEP since 1997 are averaged: $B_{NMR} = \frac{1}{N} \sum_{i=1}^{N} \left(a^i \; B^i_{NMR} + b^i \right)$. This quantity B_{NMR} is an estimate for the flux loop field based on the NMR probe readings. The averages B_{NMR} are finally calibrated with RDP to yield an estimate for the beam energy. Figure 4.4 illustrates the calibration procedure.

An estimate of the systematic error of the energy based on measurements of the magnetic fields is obtained in the following way. As described above, the fields measured by the NMR probes are fitted to the flux loop data in the same region as the RDP data (41-60 GeV). The coefficients a^i and b^i are used in the high energy region to determine an expected value for the flux loop from the NMR field measurement: $(B^{expect}_{FL})^i = a^i \; (B^{high\ E}_{NMR})^i + b^i$. Since the flux loop also provides a direct field measurement B^{meas}_{FL} up to physics energies, the field inferred from the NMR probes can be directly compared to the measured flux loop field. The difference of the two $(\Delta^B_{NMR-FL})^i = (B^{expect}_{FL})^i - B^{meas}_{FL}$ provides an estimate for the systematic uncertainty of the extrapolation procedure. The average over the individual differences is Δ^B_{NMR-FL}. To make the effect of the field measurements on the beam energy directly visible, the residual difference Δ^B_{NMR-FL} can be converted from G to MeV to an "equivalent energy": $\Delta^E_{NMR-FL} = C_s \; \Delta^B_{NMR-FL}$. The scaling factor C_s can be calculated from eq. (4.1) with a total

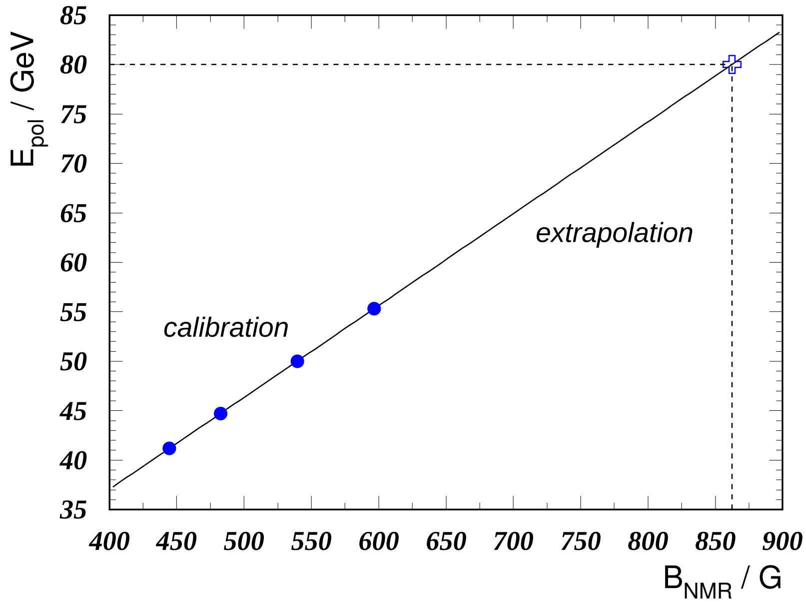

Fig. 4.4: *Beam energy obtained by resonant depolarization as function of the average magnetic field measured by the NMR probes. The field measurements are calibrated in the energy range from 41 to 60 GeV and are used to extrapolate to high energies.*

magnetic length of about 19 km. It also can be determined from a fit NMR versus resonant depolarization: $C_s = 92.6$ MeV/G. Figure 4.5 shows Δ^{E}_{NMR-FL} as function of the nominal beam energy. By construction Δ^{E}_{NMR-FL} is close to zero in the region 41-60 GeV. The difference between flux loop measurements and the NMR derived values is clearly visible, reaching about 15 MeV at 90 GeV beam energy. Figure 4.6 shows Δ^{E}_{NMR-FL} for a beam energy of 94.5 GeV for all flux loop measurements in 1998. Again the difference is in the 10-15 MeV region. Obviously a cross check for these extrapolations is needed.

4.3 The Beam Energy Model

The LEP beam energy as function of time is calculated according to the following formula:

$$\begin{aligned} E_{beam}(t) &= \left(E_{initial} + \Delta E_{dipole}(t)\right) \\ &\cdot (1 + C_{tide}(t)) \cdot (1 + C_{orbit}) \cdot (1 + C_{RF}(t)) \\ &\cdot (1 + C_{hcorr}(t)) \cdot (1 + C_{QFQD}(t)) . \end{aligned} \tag{4.6}$$

The initial dipole energy $E_{initial}$ is the beam energy corresponding to the dipole field integral at physics energy when “stable beams” have been declared. The shift in energy caused by changes in the bending dipole fields during a fill is given by $\Delta E_{dipole}(t)$. Both of these “dipole” terms are averaged over the energies predicted by each functioning NMR probe. The changes in the dipole bend field with time are due to temperature variations and parasitic currents

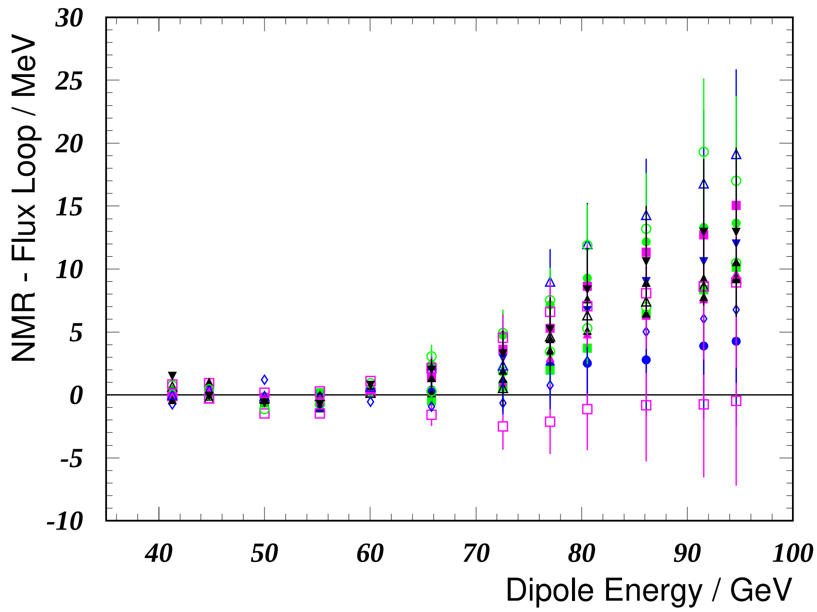

Fig. 4.5: *Difference Δ^{E}_{NMR-FL} (defined in the text) as function of nominal beam energy in 1998 [36]. A measurement sequence (denoted by different symbols) consists of one point per energy step. Each point is an average over all NMR probes, the errors represent the RMS scatter over all probes, divided by the square root of the number of probes. The points between 40 and 60 GeV are used to calibrate the NMR against the flux loop.*

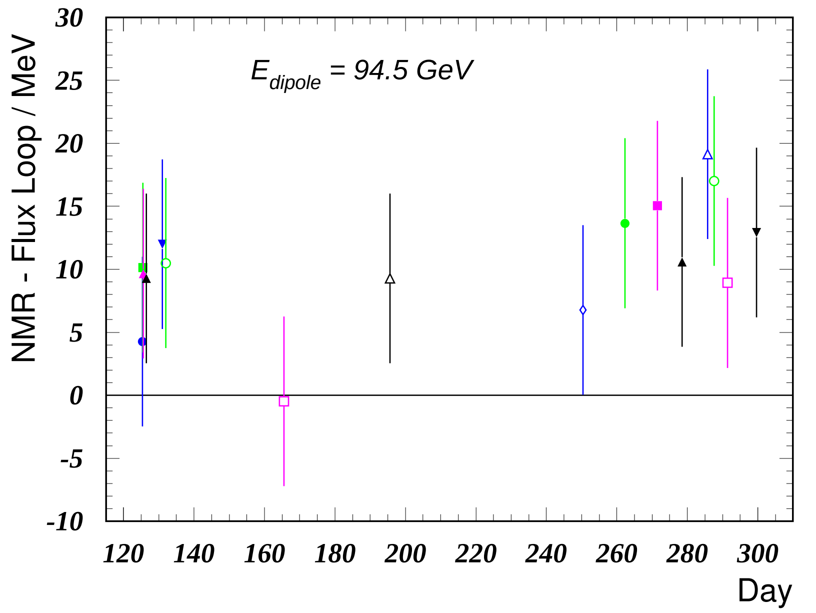

Fig. 4.6: *Difference Δ^{E}_{NMR-FL} also shown in fig. 4.5 at a beam energy of 94.5 GeV as function of day in year in 1998 [36].*

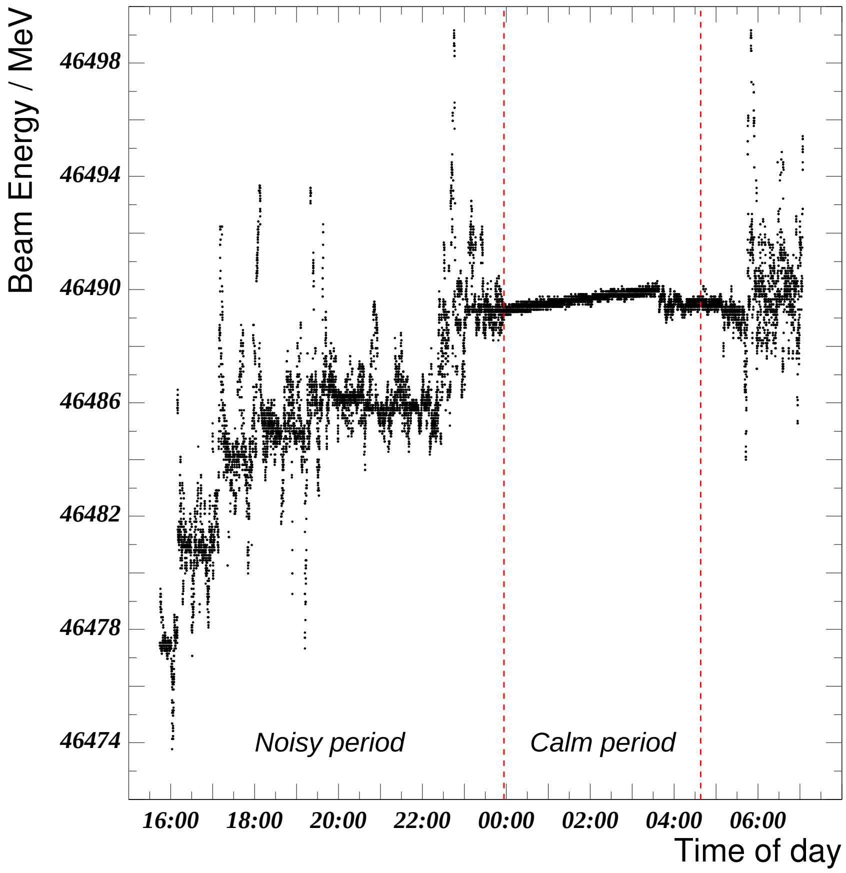

Fig. 4.7: *Beam energy as measured by a single NMR probe as function of day time. Noisy and calm periods where no jumps occur are clearly distinguishable. The sudden jumps in the field level are due to the so-called "vagabond currents" from neighboring railways [27].*

that flow on the LEP beam pipe. Figure 4.7 shows a measurement of the dipole field with a single NMR probe as function of time for a period of about fifteen hours. For convenience the field measurement has been translated into an energy. The measurement shows calm and noisy periods. All perturbations lead to an effective rise of the dipole field with time. The "jumps" in the fields were found to be caused by so-called vagabond currents originating from neighboring railways (see [27] and references therein). The dipole rise effect on the average beam energy is of the order of 4 MeV and an error of 1 MeV is assigned as its uncertainty. The remaining terms in eq. (4.6) are described briefly in the following sections.

4.3.1 Quadrupole and Corrector Effects

Machine Circumference, Earth Tides and Central Frequency

In LEP the particles are ultra-relativistic (the e^-rest mass can be neglected and $\mathtt{p} \approx \mathtt{E}$) and their velocity is practically constant. The beam revolution frequency and the length of the

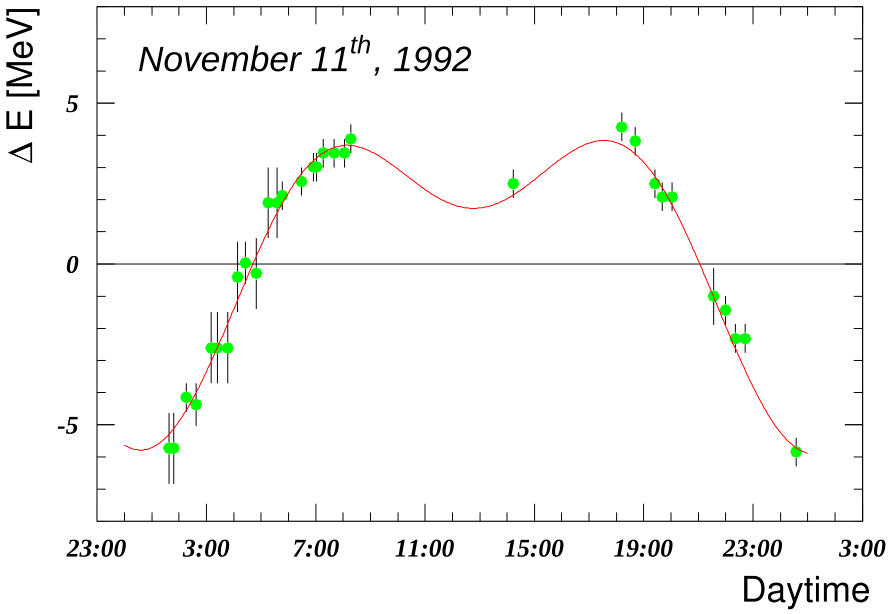

Fig. 4.8: *Energy shift due to tide effects measured with resonant depolarization during a full moon tide (taken from [38]). The curve is a prediction from a geological model.*

orbit are therefore defined by the frequency of the RF system (see eq. (2.23)). A change in circumference ΔC causes the beam to move on average off-center of the accelerator axis. According to eq. (2.2) this means an additional contribution to the integrated bending field as the field of the quadrupole magnets increases with the position offset. The change in energy can be written as

$$\frac{\Delta p}{p_0} \approx \frac{\Delta E}{E} = -\frac{1}{\alpha_c}\frac{\Delta C}{C} = -\frac{1}{\alpha_c}\frac{f_{RF}-f_{RF}^c}{f_{RF}^c} \tag{4.7}$$

where α_c is the momentum compaction factor, f_{RF} the actual frequency of the RF system and f_{RF}^c the "central frequency" corresponding to an orbit passing on average through the center of the quadrupoles ("central orbit").

Tidal effects due to the combined gravitational attraction of the Sun and the Moon cause deformations of the local Earth radius [37]. In the Geneva area the vertical motion can be as big as 25 cm peak-to-peak. This distortion changes the LEP circumference by about $\pm$ 0.5 mm [38,39]. The change in circumference is proportional to the change in the gravitational attraction Δg which can be predicted and measured with high accuracy:

$$\frac{\Delta C}{C} = \lambda_T \frac{\Delta g}{g} \tag{4.8}$$

where λ_T is a coupling parameter related to the three-dimensional elastic modulus of the surrounding geological formations. At high tide the change in gravitational attraction in the Geneva area reaches up to 1.5 μm/s^2 for an average gravitational attraction of $g = 9.805$ m/s^2. Figure 4.8 shows the energy shift due to tide effects measured with resonant depolarization

during a full moon tide. The curve is a prediction from a geological model. The parameter $C_{tide}(t)$ in eq. (4.6) corrects for the variation in energy due to tidal deformations as described by a program based on a CTE (Cartwright-Taylor-Edden) model [40] with some parameters adjusted to actual gravity measurements.
Besides the periodic tidal movements LEP is also subject to much slower long term circumference changes. In the LEP running period between May and November, the ring experiences circumference changes of up to 2 mm some of which are clearly correlated to rainfall and to fluctuations in the underground water table height. The changes in circumference are monitored by direct measurements of the central frequency [41] and interpolations based on measurements of the average horizontal beam position in the arcs of LEP ("X_{arc}") [39]. The changes in energy due to this effect are taken into account in the energy model of eq. (4.6) by the correction term C_{orbit} which is evaluated for each fill.

RF frequency shifts

To increase the luminosity by a reduction of the horizontal beam size the horizontal damping partition number J_x was routinely increased by changing the RF frequency (see eq. (2.37) in chapter 2). According to eq. (4.7) this frequency shift also changes the beam energy. A typical RF frequency shift of + 100 Hz gives a beam energy decrease of about 150 MeV. Occasionally, when an RF unit trips off, the RF frequency is temporarily decreased to increase the quantum lifetime. This effect is taken into account by the correction term $C_{RF}(t)$ in the energy model eq. (4.6).

Optics Dependent Effects and Correctors

The correctors are small dipole magnets which are used to steer the beam. The horizontal correctors influence the beam either through an additional contribution to the integrated dipole field or through a change of the orbit length [42]. The correction term $C_{hcorr}(t)$ accounts for these changes in the integral over the magnetic field along the closed orbit and thus in the beam energy (eq. (4.1)) from the horizontal correctors. When the focusing and defocusing quadrupoles in the LEP lattice are supplied with different excitation currents, the resulting stray fields of the power supply cables change the field integral. The effect of these stray fields is accounted for by $C_{QFQD}(t)$.
Both the correction for the horizontal correctors and the correction for current differences in the vertically and horizontally focusing quadrupoles depend on the machine optics and can cause differences of a few MeV between different optics. The majority of the measurements with resonant depolarization was done with a $60^o/60^o$ optics while the physics running was with the $90^o/60^o$ or the $102^o/90^o$ optics. The uncertainties due to the different optics assigned to the differences measured with resonant depolarization are listed in table 4.1.

4.3.2 Interaction Point Specific Corrections

The continuous energy loss due to synchrotron radiation in the arc sections and the discrete energy gains from the RF system lead to large local deviations from the average beam energy ("sawtooth", see detailed discussion in chapter 6). A model taking into account the actual voltage distribution and the energy gains as measured from shifts in horizontal position of the beam is used to calculate the effect on the center-of-mass energy at the individual interaction points (IP). The IP specific energy shifts from the RF model for a center-of-mass energy of 183 GeV for example are of the order of 10 MeV.
In the bunch train configuration, beam offsets at the collision points can cause shifts in the center-of-mass energy due to opposite sign dispersion [27]. Usually LEP is filled with four bunches per beam with equal spacing of 22 μs, in the bunch train scheme of 1997 it is filled with four "trains" consisting of up to three bunches with a spacing of 327 ns between two bunches of one train [43, 44]. The change in energy is evaluated from the calculated dispersion and the measured beam offsets at the interaction points. No corrections are applied for this effect and the assigned uncertainty is 2 MeV.

4.3.3 Energy Spread

The spread in center-of-mass energy is relevant for evaluating the width of the W boson which is about 2 GeV. The beam energy spread can be predicted for a particular optics, beam energy and RF frequency shift. For a center-of-mass energy of 183 GeV the predicted luminosity weighted average beam energy spread is (155 ± 8) MeV [28]. The corresponding spread in center-of-mass energy is (219 ± 11) MeV . The beam energy spread can also be derived from the longitudinal bunch size (longitudinal size of the interaction region σ_z^{IP}) measurable by the experiments (e.g. ALEPH). The beam energy spread can be written as [7, 28]

$$\frac{\sigma_\varepsilon}{E_{\mathrm{beam}}} = \frac{\sqrt{2}\ \omega_{\mathrm{rev}}}{c\ \alpha_c}\ Q_s\ \sigma_z^{\mathrm{IP}} \tag{4.9}$$

where ω_{rev} is the revolution frequency and Q_s the synchrotron tune. The average beam energy spread determined in this way for a center-of-mass energy of 183 GeV is (152 ± 8) MeV [28]. Besides the spread in center-of-mass energy, the beam energy spread also causes boosts of the center-of-mass system which are discussed in chapter 9.

4.4 1997 and 1998 Energies and Errors

The center-of-mass energy of LEP for a given IP is finally given by

$$E_{\mathrm{cm}}^{\mathrm{IP}}(t) \ = \ 2\ E_{\mathrm{beam}}(t) \ + \ \Delta E_{\mathrm{RF}}(t) \ + \ \Delta E_{\mathrm{disp}}(t) \ + \ \Delta E_{e^+} \tag{4.10}$$

where $\Delta E_{\mathrm{RF}}(t)$ is the energy shift calculated from the RF model, $\Delta E_{\mathrm{disp}}(t)$ the dispersion contribution and ΔE_{e^+} the energy difference of electrons and positrons (the measurements with

Source of uncertainty	Error [MeV] 1997	1998
Extrapolation from NMR-polarization:		
NMR rms/$\sqrt{N}$ at physics energy	10	8
different E_{pol} fills	5	4
Flux loop test of extrapolation:		
NMR-flux loop difference at E_{phys}	20	15
Field not measured by flux loop	5	5
Polarization systematic	1	1
e^+e^- energy difference	2	2
Optics difference	4	6
Corrector effects	3	4
Tide	1	1
Initial dipole energy	2	1
Dipole rise modeling	1	1
IP specific corrections ($\delta E_{cm}/2$):		
RF model	4	4
Dispersion	2	2
Total error	25	20

Tab. 4.1: *Contributions to the total beam energy errors for 1997 and 1998. The largest contribution is due to the difference of the flux loop - NMR extrapolation [28, 45].*

resonant depolarization are usually done with electrons). The individual contributions of the different effects on the total beam energy error are listed in table 4.1. The largest contribution to the total error is due to the differences Δ^E_{NMR-FL} discussed in section 4.2.3.

4.5 Methods and Cross-checks under Development

The differences between flux loop and NMR extrapolations make it desirable to have other methods with different, independent and hopefully smaller systematic errors. One approach was to install a dedicated beam spectrometer, another one, pursued for this thesis, is the energy determination based on measurements of the energy loss.

4.5.1 The LEP Spectrometer

The determination of the beam energy with a spectrometer is based on the dependence of the bending angle on the integral over the magnetic field of the respective magnet and on the beam energy:

$$\theta \propto \frac{\int B ds}{E_0}. \tag{4.11}$$

Magnetic field and bending have to be measured with the needed accuracy for a high precision energy measurement. Figure 4.9 shows the layout of the LEP spectrometer. The change in

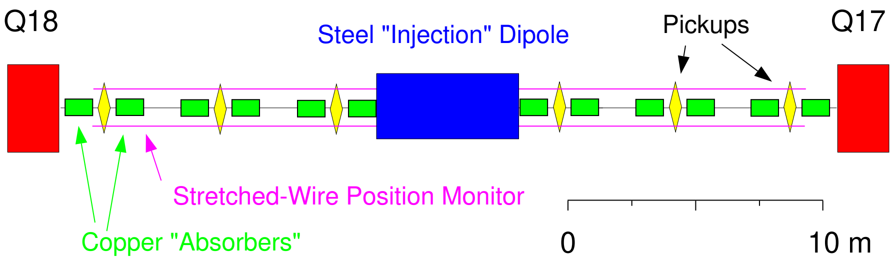

Fig. 4.9: *Layout of the LEP spectrometer. The change in bend angle in the steel injection type dipole magnet is measured with three beam position monitors on both sides of the magnet.*

bending angle in a steel injection type dipole magnet is determined with three high precision beam position monitors on both sides of the magnet. To achieve a relative energy uncertainty of $\Delta E/E = 1 \cdot 10^{-4}$ the beam position in the pickups has to be measured to 1 μm and the uncertainty on the magnetic field must not exceed $\Delta B/B = 3 \cdot 10^{-5}$. Field measurements on the spectrometer magnet showed the relative uncertainty of the integrated field determination to be smaller than the required $3 \cdot 10^{-5}$. To verify the accuracy of the position determination the so-called triplet residual is defined as the difference of the average horizontal beam position in the two outer pickups of one spectrometer arm and the position measured with the middle pickup:

$$T = \frac{x_1 + x_3}{2} - x_2.$$

The resolution of this triplet residual was found to be better than 1 μm. Studies and comparison with NMR and polarization measurements have shown the energy uncertainty of the spectrometer measurements to be of the order of 15 MeV at physics energies [46].

4.5.2 Energy Determination from Energy Loss Measurements

A different approach to the energy determination is based on measurements of the energy loss per turn. Because the energy loss from synchrotron radiation increases with the fourth power of energy (eq. (2.33)), observables sensitive to the energy loss per turn can be used to determine

the beam energy of LEP2.
Three different methods to measure the energy loss have been studied in the framework of this thesis and are described in detail in the following chapters. The first technique is based on measurements of the damping of horizontal coherent oscillations after an excitation, the second on the analysis of electron positron difference orbits and the last one on studies of the relation between synchrotron tune Q_s and total accelerating voltage. In contrast to the spectrometer all three methods make use of existing LEP equipment only.

Chapter 5

Damping of Coherent Oscillations

LEP2 provides a rather unique opportunity to study energy loss and synchrotron frequency in an environment with major synchrotron radiation losses and high Q_s. The main motivation for the studies presented in the following chapters however is the development of a reliable energy determination at the highest energies with an accuracy of 20 MeV or better. The presently used extrapolation methods using magnetic measurements cross-calibrated with resonant depolarization (see chapter 4) in the range from 40 to 60 GeV show systematic deviations of the order of 15 MeV at highest energies [28]. The methods described in the following chapters are alternative cross-checks, based mainly on determinations of the energy loss and using existing LEP equipment. This chapter concentrates on measurements of the damping of coherent oscillations of the beam. The damping time due to synchrotron radiation can be used to determine the energy loss. As a side product this technique yields accurate measurements of the transverse betatron tune dependence on the particle amplitude. This parameter is important for the understanding of the dynamic aperture of a machine optics. The measurements of the horizontal detuning with amplitude were discussed in detail in chapter 3.

5.1 Coherent Damping

The determination of the synchrotron radiation loss from the damping of coherent oscillations is based on the same so-called "1000-turn measurements" as the analysis of the horizontal detuning with amplitude: a coherent horizontal oscillation is excited by a single kick and the center-of-charge position of the bunch is observed over 1024 consecutive turns. Figure 5.1 shows four such 1000-turn datasets measured under the same conditions with different bunch currents. A fit to the data by a damped oscillation with amplitude dependent frequency (eq. (3.5)) yields the coherent damping time τ as described in chapter 3.

The coherent damping at LEP is composed of radiation and head-tail damping:

$$1/\tau_{\mathrm{coh}} = 1/\tau_0 + 1/\tau_{\mathrm{head-tail}}. \tag{5.1}$$

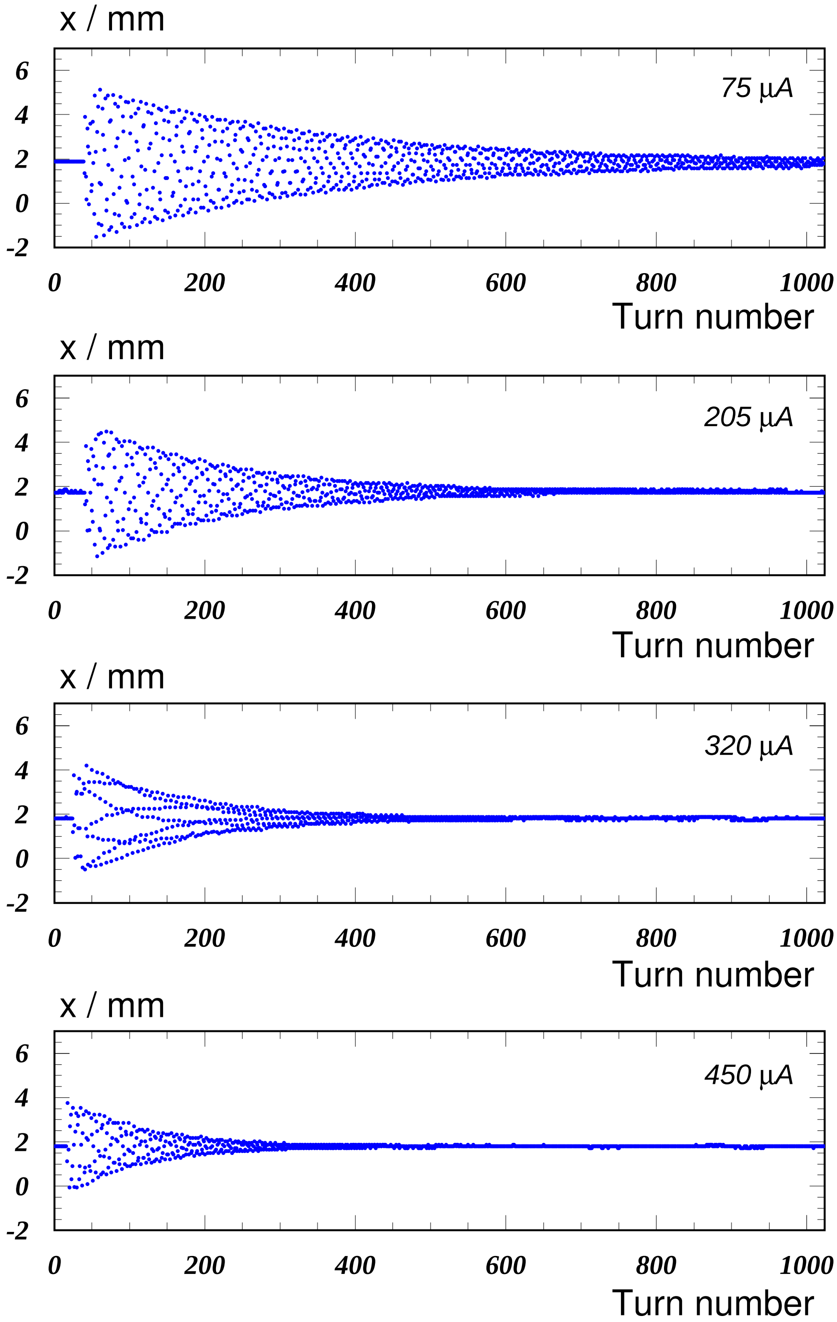

Fig. 5.1: *Center-of-charge position versus turn number for different bunch currents. The damping rate is proportional to the bunch current.*

The head-tail effect is based on the impact of electromagnetic wake fields generated by the head of a particle bunch on the transverse betatron motion of the tail. The bunch can be described as two macro-particles representing head and tail. The fields of the head particle act on the tail while the reverse is not true due to causality. However, the particles perform energy oscillations and half a synchrotron oscillation period later the roles of head and tail are reversed. Detailed descriptions of this effect can be found in [8] and [47]. Two transverse oscillation modes are

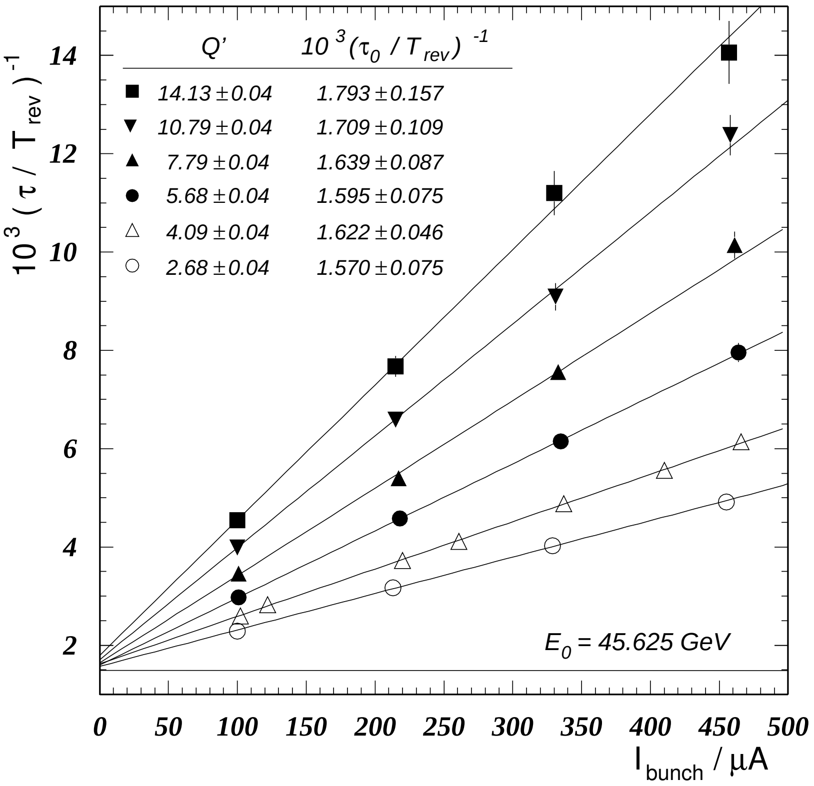

Fig. 5.2: *Damping rate (inverse damping time) τ^{-1} as function of bunch current for various chromaticities measured at a beam energy of 45.6 GeV. The revolution period is $T_{\mathrm{rev}} =$ 88.9 μs. The results are based on turn by turn measurements.*

observed: a dipole mode where head and tail oscillate in phase and a quadrupole mode where head and tail are 180° apart in phase. The 1000-turn measurements observe the dipole mode only. The dipole mode of the head-tail instability is damped for positive chromaticities and anti-damped for negative chromaticities. The head-tail damping rate τ^{-1} is finally given by

$$1/\tau_{\mathrm{head-tail}} \propto \frac{W_0 \sigma_s Q'}{E_0\ \alpha_c} I_b \tag{5.2}$$

where Q' is the chromaticity, I_b the bunch current, σ_s the RMS bunch length, W_0 a representation of the impedance in the time domain and E_0 the beam energy. The dependence on the bunch current is obvious from fig. 5.1: the higher the bunch current, the shorter the damping time. The seemingly different patterns of the 1000-turn datasets are generated by a stroboscope effect due to the sampling frequency (one position measurement per turn). The damping rate as function of bunch current for different chromaticities at a beam energy of 45.6 GeV is shown in fig. 5.2. The decrease of damping time with chromaticity is clearly visible. A table in the plot contains the measured chromaticities and the corresponding damping rates for zero bunch current. The scatter of the results contributes to the error of the method. Figure 3.7 on page 32 shows a similar measurement at a beam energy of 60 GeV.

As a side product the dependence of the head-tail damping rate on the chromaticity gives some hints on the tranverse resistive impedance of the machine: the so-called wake function W_0 in eq. (5.2) is linked to the impedance. Figure 5.3 shows the head-tail damping rate (see eq. (5.2))

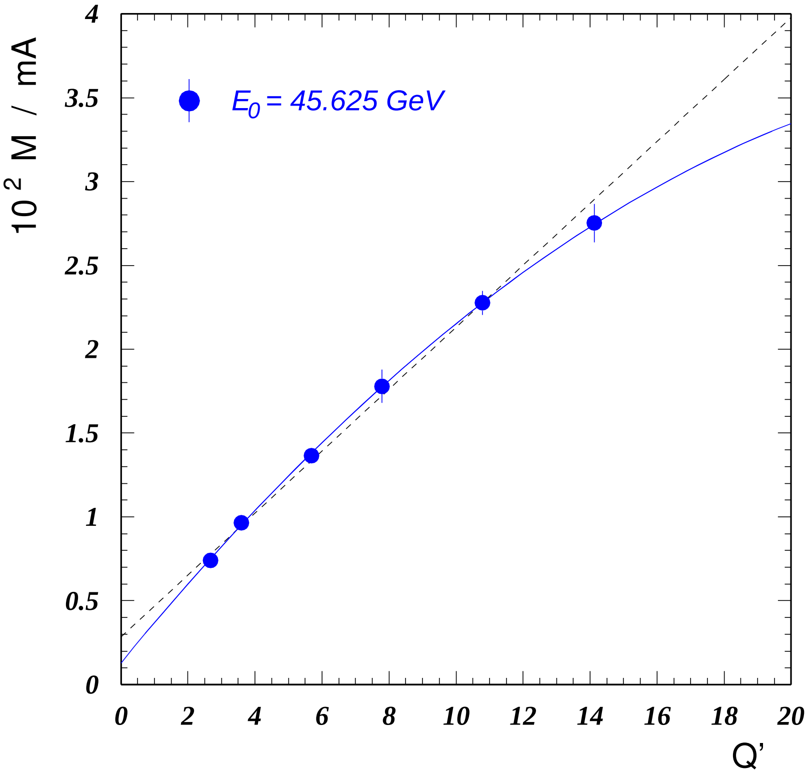

Fig. 5.3: *Head-tail damping rate divided by the bunch current M as function of measured chromaticity for a beam energy of 45.6 GeV. The dashed line is straight line fit to the data, the solid curve the fit of a sine function.*

divided by the bunch current as function of measured chromaticity: $M(Q') = \tau^{-1}_{\text{head-tail}}\, T_{\text{rev}}\, / I_b$. From the shape of this curve some general information on the transverse resistive impedance can be extracted which is however beyond the scope of this study.

5.2 Extraction of the Energy Loss

The head-tail contribution to the total damping rate eq. (5.1) depends on the bunch current. An extrapolation to $I_b = 0$ yields the damping rate due to synchrotron radiation τ_0^{-1} from which the energy loss or energy can be extracted. A straight line fit to the measurements of the damping rate as function of bunch current is used to extrapolate to a zero current. To guarantee identical machine conditions for all measurements LEP was filled with four bunches of different currents for these investigations.
The damping rate of the horizontal oscillation due to synchrotron radiation is given by

$$\tau_0^{-1} = \frac{1}{2}\,\frac{U_0\, f_{\text{rev}}}{E_0}\, J_x \tag{5.3}$$

where U_0 is the energy loss, f_{rev} the revolution frequency and J_x the horizontal damping partition number (see chapter 2). A comparison to a MAD prediction is used to evaluate the energy loss from the measurements of the radiation damping rate $\left(U_0 = U_0^{\text{MAD}}\ \tau_0^{\text{MAD}}/\tau_0^{\text{meas}}\right)$. To make a correct prediction the actual central frequency and shifts due to tide effects have to be taken into account. The frequency shift can be translated into a shift of horizontal damping partition with dJ_x/df_{RF} determined from MAD. The changes in damping partition number for the measurements discussed in this chapter are of the order of 7 %. The uncertainty of the central frequency measurement of 1 Hz is a major contribution to the total uncertainty of this method to determine the energy loss.

The damping rate determined by fits to the 1000-turn data does not depend on the initial amplitude of excitation of the coherent oscillation. This is shown by fig. 5.4 where the damping rate as function of bunch current was measured with four different kicker voltages. The initial

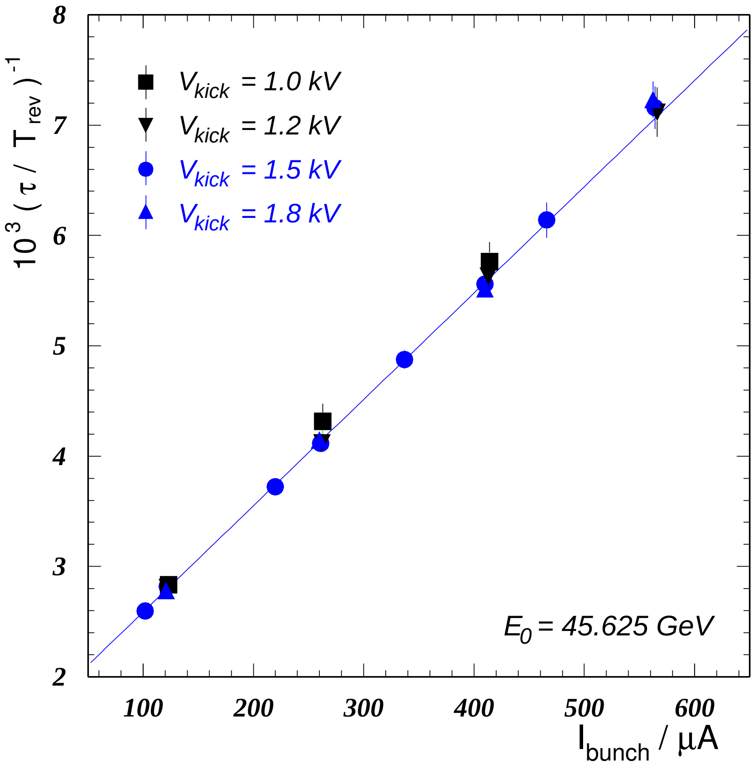

Fig. 5.4: *Damping rate τ^{-1} as function of bunch current for different kicker voltages. The start amplitude of the coherent oscillation is proportional to the injection kicker voltage.*

deflection and amplitude of the oscillation are proportional the kicker voltage. This insensitivity to the initial conditions shows that there is no influence on the measurement from filamentation effects.

As the energy loss increases with the beam energy, the contribution of the radiation damping to the total coherent damping time becomes more significant. Unfortunately the precision of the damping measurements degrades if the damping times are too short. This means that an energy loss measurement at high energies with this method becomes difficult. There is however a way to counterbalance the radiation damping with the head-tail damping: a combination of negative chromaticity and bunch current can be used to increase the total damping time. Figure 5.5

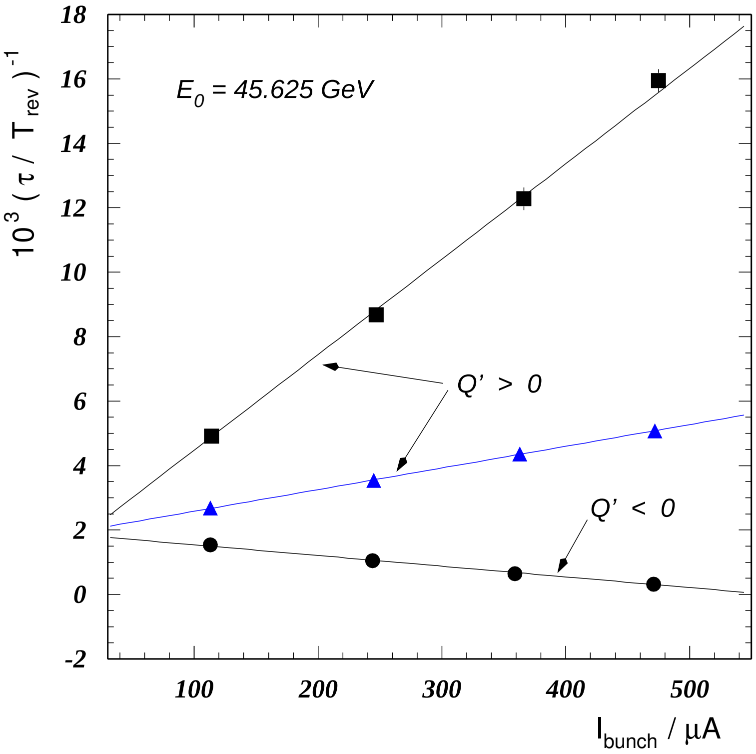

Fig. 5.5: *Damping rate τ^{-1} as function of bunch current for chromaticities of opposite sign. The change in slope is clearly visible.*

shows measured damping rates for chromaticities of opposite sign. The tunes have been kept constant for all measurements shown in the figure, the chromaticity was changed with sextupole magnets (see sections 2.2.3, 3.5). The 1000-turn dataset with the highest bunch current and a negative chromaticity is almost undamped.

5.3 Results

Measurements of the damping time of transverse coherent oscillations for different bunch currents have been performed at beam energies of 45.6 and 60 GeV. A major contribution to the uncertainty of the energy loss is the error on the central frequency measurement of 1 Hz which translates into an uncertainty on the horizontal damping partition number of the order of 0.01. Table 5.1 gives the results of the energy loss determinations in comparison with predictions of

energy [GeV]	energy loss [MeV]	
	MAD	measured
45.625	127	126 ± 9
60.000	380	382 ± 4

Tab. 5.1: *Results and* MAD *predictions of the energy loss due to synchrotron radiation at 45.6 and 60 GeV beam energy.*

the MAD program. Both measurements are in very good agreement with the expectation. The uncertainty of these energy loss determinations however yields a relative uncertainty on the energy of the order of 1 %. Although the method works reliably the uncertainty is too large to make it useful as a cross-check for energy calibration.

Chapter 6

The Energy Sawtooth

The horizontal beam position is a function of the local beam momentum. The continuous energy loss due to synchrotron radiation in the arc sections and the discrete energy gains from the RF system lead to sawtooth-like horizontal orbits in the LEP ring. This is illustrated by fig. 6.1. It shows the calculated positions of electrons and positrons at the quadrupoles. The horizontal and

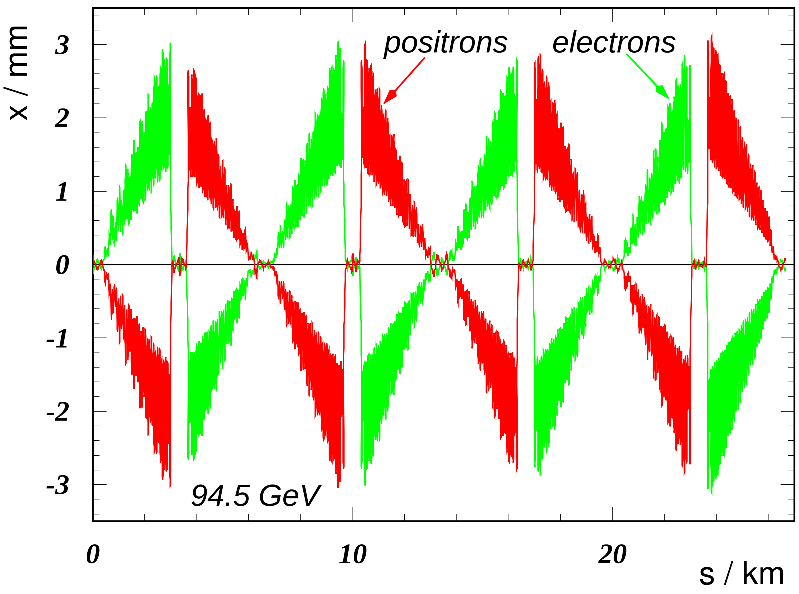

Fig. 6.1: *Electron and positron positions at the quadrupoles calculated with the* MAD *program for a beam energy of 94.5 GeV.*

vertical positions of electrons and positrons are measured with the 504 beam position monitors ("pickups") distributed around the ring (see chapter 3). In the arcs, the monitors are located near the horizontally defocusing quadrupoles. This implies that the measured horizontal orbit reflects a minimum position offset in a cell rather than an average, because the horizontal dispersion and β-function are minimal at the defocusing quadrupoles.

The sawtooth cannot be observed accurately in the orbit measurement of a single beam because the position offset due to the sawtooth is superposed by the closed orbit. For that reason the e^+e^- difference orbit must be used to analyze the sawtooth. The difference of measured electron and positron positions in the arc sections for a fill at a beam energy of 94.5 GeV is shown in fig. 6.2 with the pickup number as longitudinal coordinate. The energy loss in the arcs is as clearly visible as the energy gain from the RF system, located at the even interaction points (IPs). The difference between the positron and electron orbits can be used to determine the

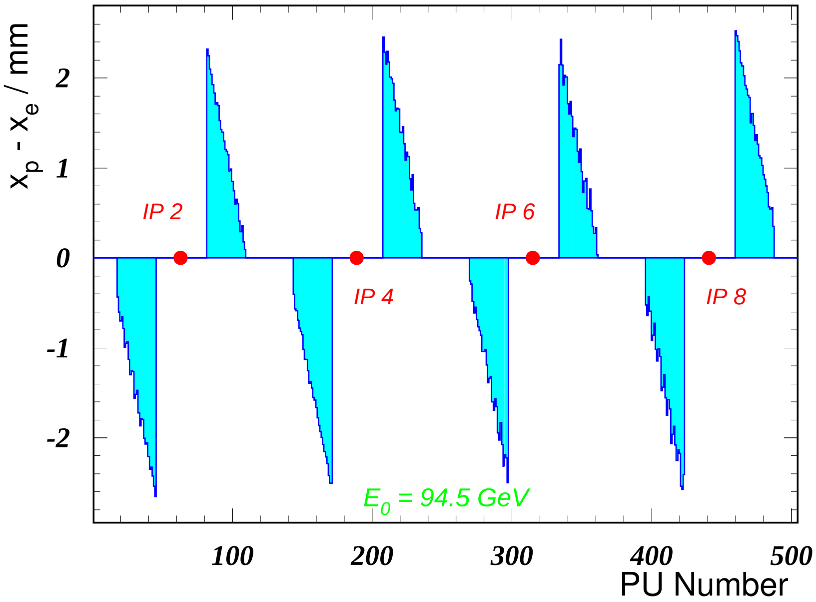

Fig. 6.2: *Measured electron-positron difference orbit for a beam energy of 94.5 GeV. Only data for arc quadrupoles are displayed.*

energy loss with the help of the horizontal dispersion D_x. The basic equation for particle motion with energy offsets $\Delta x = D_x\ (\Delta E/E_0)$ yields a relation for the energy loss where Δx is defined as change in position of a particle due to a relative change in energy $\Delta E/E_0$. The energy change over one arc section is calculated from the change in difference orbit between the two extreme points of the arc: $\Delta(\delta x) = (x_{e^+} - x_{e^-})_{\text{end}} - (x_{e^+} - x_{e^-})_{\text{start}}$. As electron and positron positions are of opposite sign, the position change of the difference orbit has to be divided by two. The energy loss ΔE per arc section is given by

$$\Delta E \ = \ \frac{\Delta(\delta x)}{2D_x}\, E_0 \ = \ \frac{\Delta(x_{e^+} - x_{e^-})}{2D_x}\, E_0. \tag{6.1}$$

The total energy loss U_0 in the arcs is given by the sum over the losses in all arc sections. The beam energy follows the scaling law $E_0 = \kappa\ \sqrt[4]{U_0}$. To translate the energy loss extracted from the sawtooth into a beam energy the constant κ has to be determined from cross-calibrations with resonant depolarization measurements at low energies. The sawtooth can then be used for extrapolations to high energy.

6.1 Fitting the Sawtooth

For an accurate extraction of the energy loss from the sawtooth an adequate functional form must be fitted to the orbit difference. The use of the difference orbit has the advantage that systematic effects due to mechanical and electronic offsets cancel out. Since in general a residual betatron oscillation is superposed onto the sawtooth the difference orbit can be parameterized by

$$\delta x(s) = ms + b + A\sin(\mu(s)) + B\cos(\mu(s)) \tag{6.2}$$

where δx is the difference orbit as function of the longitudinal coordinate s and $\mu(s)$ is the phase advance. The slope of the fit m is used to calculate the position change in the individual octants

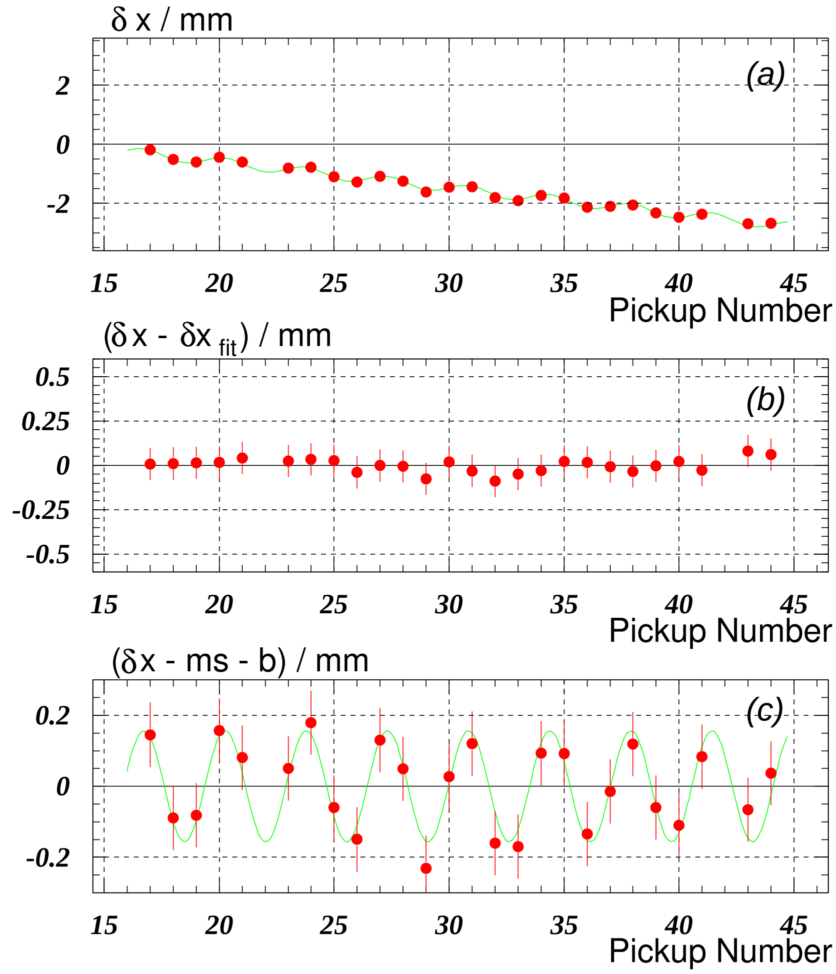

Fig. 6.3: *Details of the sawtooth fit for the first octant. (a) Measured difference orbit and fit. (b) Fit residuals. (c) Only the oscillation part of data and fit is shown.*

which is then translated into an energy loss using eq. (6.1). Only the 240 monitors located in the arc sections are used. The horizontal dispersion is assumed to remain constant in the arcs and the value is taken from MAD. Figure 6.3 shows the result of a fit to the difference orbit in the

first octant for a fill at 96 GeV. Plot (a) shows the measured difference orbit and the fit result. The difference between the measurement and the fit is displayed in plot (b). The oscillation part of data and fit is shown in plot (c).
During regular LEP operation, the orbit is measured automatically every 40 to 60 seconds and an on-line fit program evaluates the energy loss according to the model every 4 minutes. The results are stored in the LEP ORACLE database. For the on-line fits only obviously outlying pickups are rejected and the set of rejected monitors is determined individually for each orbit measurement. A pickup measurement is accepted, if the measured position at pickup i differs by less than 80 % from the position of either pickup i-1, i-2 or the first pickup of the arc. A measurement is rejected if the absolute average of electron and positron position exceeds the value of 2 mm. For consistent results however a careful selection – by visual inspection of many fits – of the monitors to be used in the fits must be done off-line. For the final analysis the same set of outlying pickups is rejected for all fits. This technique reduces the scatter of the individual fits effectively.

6.2 Systematic Errors of the Orbit Measurement

The determination of the energy loss from sawtooth fits relies on the accuracy of the orbit measurements. To take into account electronic offsets the monitors are calibrated several times a year. For this calibration, test pulses of a defined amplitude are sent to the buttons of the beam position monitors and the electronic's response is analyzed. The resulting offsets are defined for positrons but are expected to be the same for electron signals so that the net effect on the difference orbit should be zero. Figure 6.4 shows an example of pickup offsets determined with test signals. Plot (a) shows the offsets in mm for all LEP monitors, plot (b) only the pickups used for the energy loss fits. A hint to the stability and reliability of these measurements is given by plot (c): it shows the difference between two such tests performed within 5 minutes. The noise level to be estimated from these results is about 10 to 20 μm. This can also be seen in fig. 6.5, which shows the scatter of the difference between two successive orbit simulations.
The measured difference orbits show no dependence on the beam current. This is illustrated by fig. 6.6 where the energy loss from sawtooth fits (explained in the previous section) is plotted as function of the total beam current and of the difference between electron and positron current. The points are averages over all measurements in a fill. The errors are estimated from the distribution of the results within a fill. The scatter of the averages is larger than the individual errors. This points at a systematic problem that will be addressed in detail later. To take into account effects from the long term stability of the orbit measurement system as well as the read out uncertainty an error of 50 μm is assigned to the measurements of the e^+e^- beam position difference.

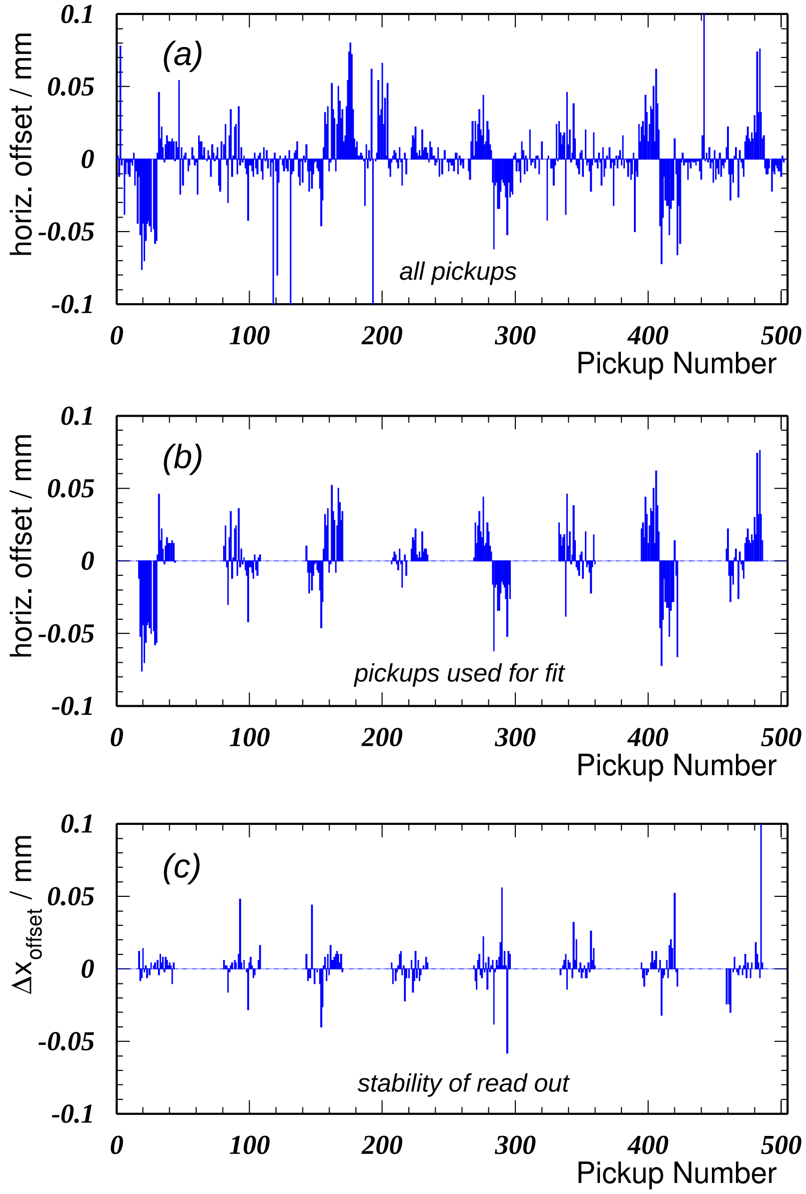

Fig. 6.4: *Offsets in the positions measurements as determined from simulated orbits, obtained by injecting test pulses to the BPM buttons.*
(a) Offsets for all monitors. (b) Only the pickups used in the sawtooth fits are shown. (c) Difference between successive measurements in the arc regions.

6.3 Results

Results of off-line fits to the sawtooth are shown in figure 6.7 where the energy loss is plotted as a function of the day in the year and in fig. 6.8. The fit results scatter around a central value but there are clear "jumps" some of which correspond to BPM calibrations (dashed lines). The other jumps could not yet be accounted for. Although the scatter of the energy loss could be reduced by careful selection of the pickups used in the fits, the jumps indicate additional pickup

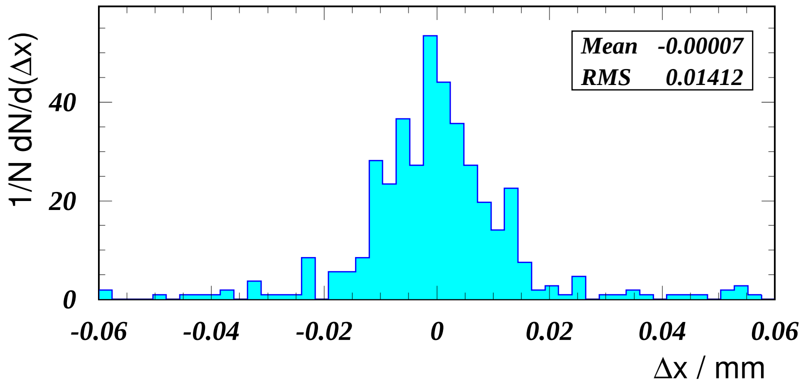

Fig. 6.5: *Scatter of difference between successive orbit simulations of fig. 6.4, plot (c).*

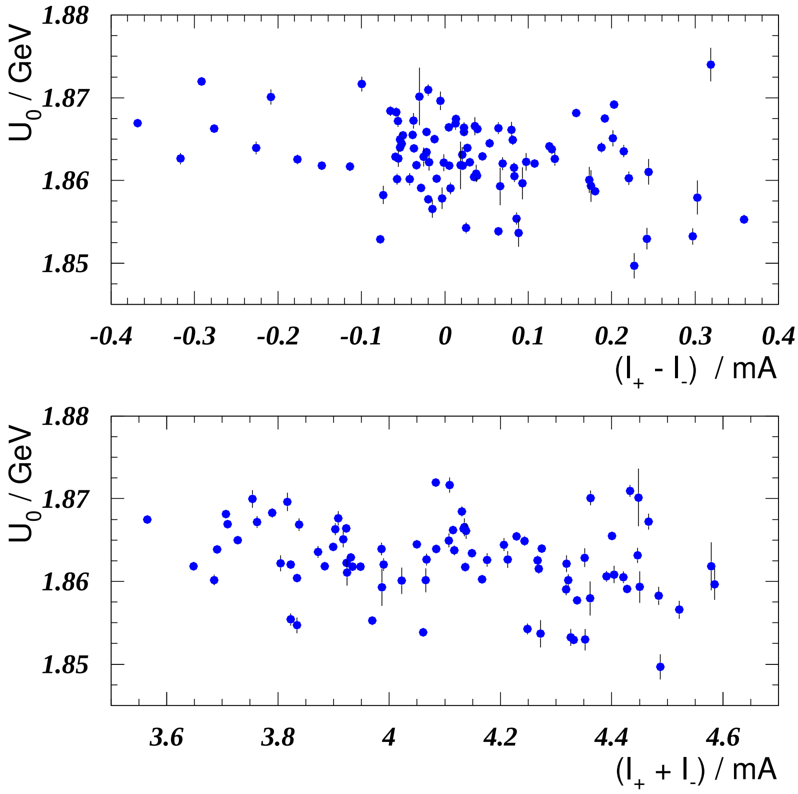

Fig. 6.6: *Energy loss from measured difference orbits as function of difference between electron and positron current (top) and of total beam current (bottom). The points are averages over all measurements in a fill. The errors represent the scatter of the fit results within a fill.*

systematics. Furthermore the fit results differ between the octants. This could indicate that the average dispersion is not the same in all octants. A more equal distribution of the energy loss around the machine would be expected. The rejection of a single monitor can change the resulting energy loss considerably. This effect as well as the difference of the energy loss in the octants is illustrated by fig. 6.9. It shows the fitted energy loss for octants 5 to 8. For octant 7

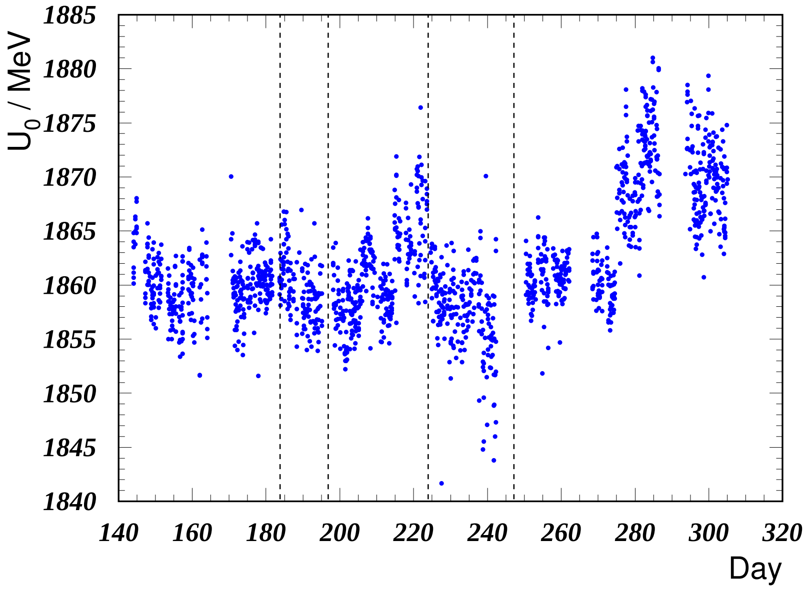

Fig. 6.7: *Energy loss from the sawtooth fits in MeV as function of day in year. The dashed lines denote BPM calibrations. The points are the results of fits to individual orbit measurements.*

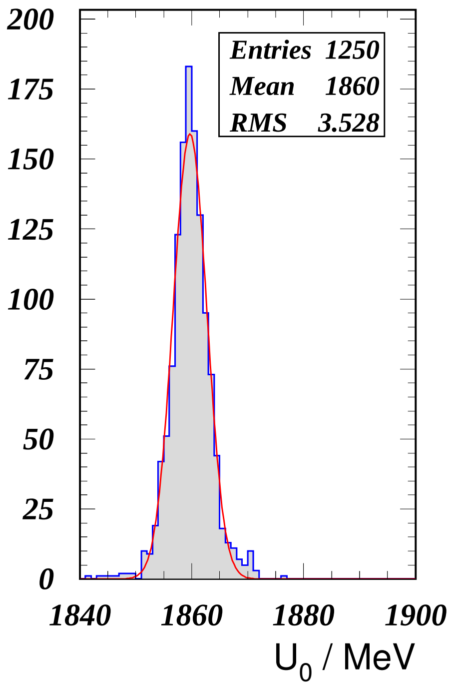

Fig. 6.8: *Distribution of the energy loss resulting from fits to the sawtooth before the large jump around day 275 for a beam energy of 94.5 GeV. The relatively small RMS of this distribution yields a relative uncertainty for a possible energy determination of the order of 5 10^{-4}.*

the effect of the rejection of one pickup with sometimes spurious reading is shown: The average energy loss is shifted by ~ 2 MeV.
In spite of these problems the results of fig. 6.8 can be used to estimate an uncertainty of a possible energy determination using this method. Figure 6.8 shows the distribution of the energy loss before the last jump around day 275. The RMS of this distribution is relatively small and corresponds to a relative uncertainty of the energy of the order of 5 10^{-4}.
Though promising, this method is strongly limited by systematic effects. The fit results differ between the octants, depend on the rejection of faulty BPMs and exhibit jumps sometimes correlated to BPM calibrations. Especially the selection of monitors has to be done carefully. It is not clear that even a more sophisticated algorithm for the identification of faulty pickups could solve the problem. The good intrinsic accuracy and the parasitic measurement favor this method but the systematics are not yet under control.

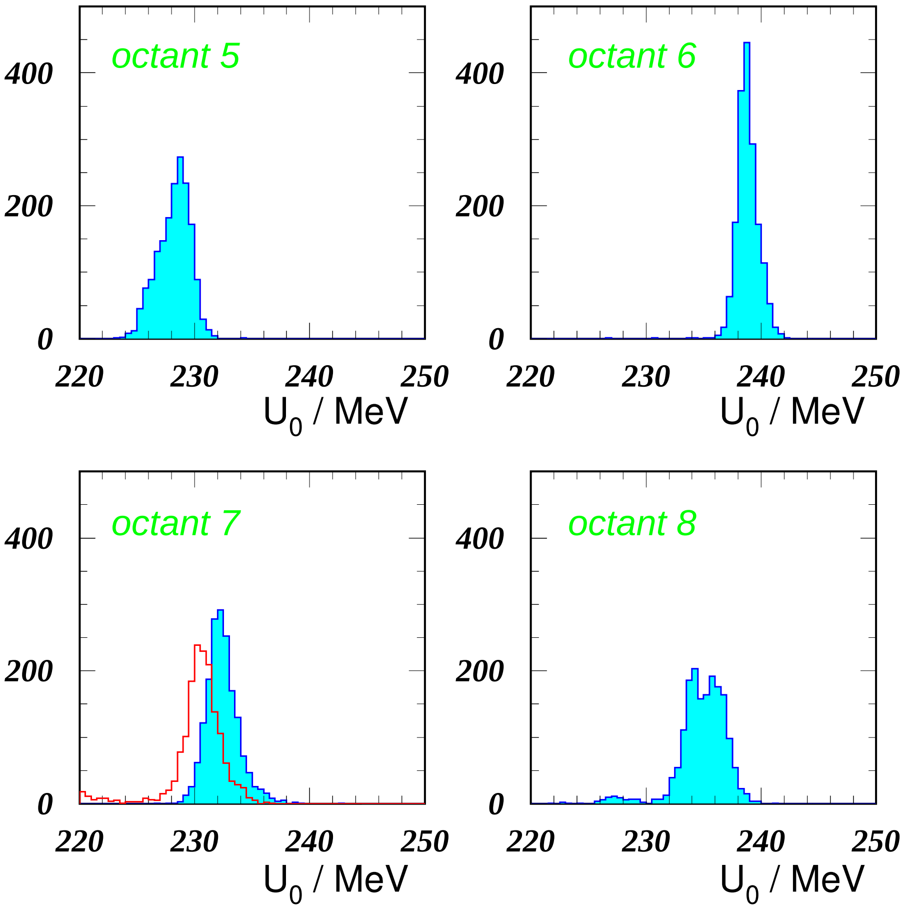

Fig. 6.9: *Distribution of energy loss from the individual fits to the sawtooth in octants 5 to 8. The filled histograms represent the nominal set of accepted position monitors, the unfilled histogram is a case where one additional pickup was excluded in octant 7. This omission caused a shift of the distribution by ~ 2 MeV.*

Chapter 7

Energy Determination from Q_s

For a given machine optics the synchrotron tune depends mainly on the total RF voltage V_{RF} and the beam energy. The synchrotron tune is particularly sensitive to the energy for low RF voltages since the relation between Q_s and the total accelerating voltage V_{RF} is given by

$$Q_s^2 = \left(\frac{\alpha_c h}{2\pi E}\right) \sqrt{e^2\ V_{RF}^2 - U_0^2} \tag{7.1}$$

where $U_0 = (C_\gamma/\rho)\ E^4$ is the energy loss, α_c the momentum compaction factor, h the harmonic number and ρ the average magnetic radius. In this thesis measurements of Q_s as function of

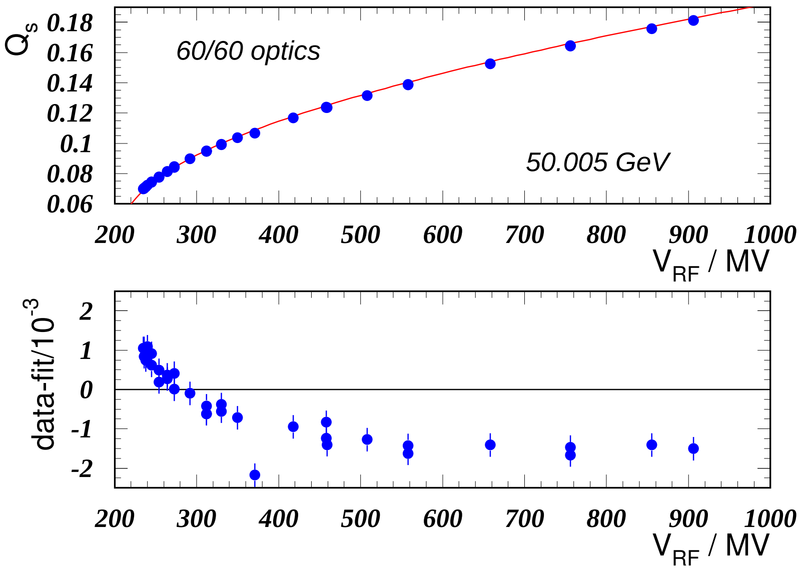

Fig. 7.1: *Upper plot: Synchrotron tune as function of total RF voltage measured at 50.005 GeV. The curve is a best fit according to eq. (7.1). Lower plot: Difference between data and fit for the same range.*

V_{RF} are used to extract the beam energy. The upper plot of fig. 7.1 shows a measurement of the synchrotron tune as function of total RF voltage at 50.005 GeV. The curve is a best fit according to eq. (7.1). The bottom plot of fig. 7.1 shows the difference between data and fit. The fit residuals clearly show that the simple model of eq. (7.1) yields only a first order description of the synchrotron tune. Equation (7.1) is not suited for a high precision energy determination since it assumes that the RF voltage is homogeneously distributed along the ring, that the synchrotron oscillation amplitudes are small and since it neglects a damping term related to the synchrotron radiation (see derivation in chapter 2). At LEP2 however these assumptions no longer hold true: the RF cavities are concentrated in the four even straight sections and synchrotron radiation losses of the order of a percent of the beam energy are non-negligible. Obviously an effective description of Q_s is needed which takes all these effects into account. This chapter discusses the individual contributions and corrections to eq. (7.1) needed for an appropriate description of the synchrotron tune and the fit methods employed to extract the beam energy as precisely as possible. The last section contains an overview of all datasets discussed in the following.

7.1 Measurement of the Synchrotron Tune

The measurement of the synchrotron tune is based on a measurement of the phase between a bunch and the RF frequency (a good description of the general principle of the detection of synchrotron oscillations can be found in [9]). Figure 7.2 shows a block diagram of the LEP

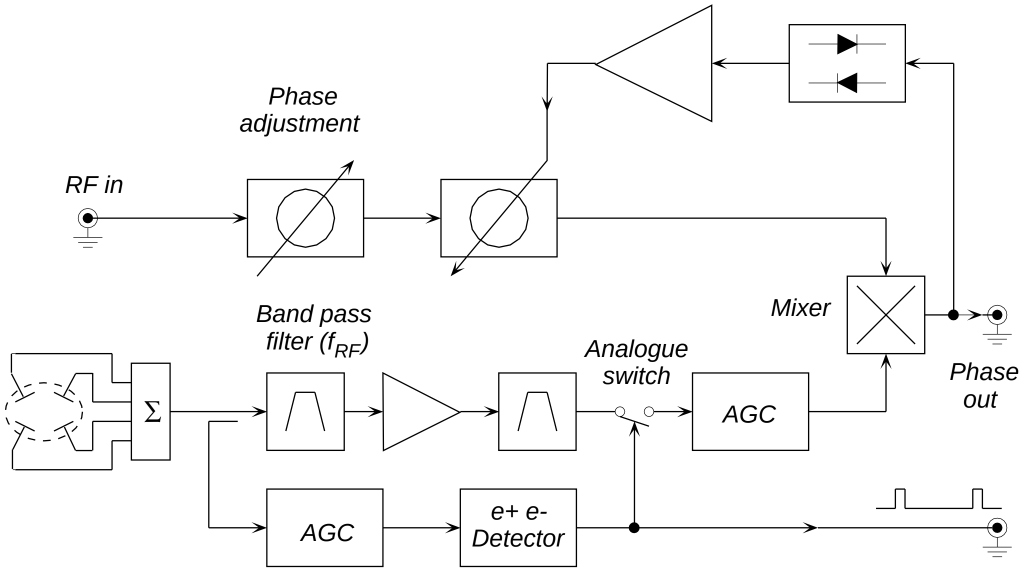

Fig. 7.2: *Block diagram of the synchrotron oscillation detector [48].*

bunch phase measuring system [49]. The sum signal from a pickup (four button monitor, see fig. 3.2) is processed with band pass filters centered at the RF frequency (352 MHz), amplifiers and an automatic gain control (AGC) loop. The phase of the resulting signal, a 352 MHz burst, is compared to the RF frequency (mixer). The amplitude of the output signal is proportional to the phase difference. Phase differences of less than 0.1 degree at 352 MHz, corresponding to differences in Q_s of about 10^{-5}, can be measured for bunch currents between 5 μA and 2.5 mA [49]. The output of the phase detector is Fourier analyzed with a spectrum analyzer. Figure 7.3 shows a photograph of the spectrum analyzer output. In general the signal is averaged over several turns and over all bunches. The current in different bunches should therefore be chosen approximately equal for a reliable energy determination since otherwise certain current dependent contributions to the energy loss cannot be determined appropriately for the analysis. The bunch-RF phase measuring system,triggered by the pickup signal, contains an e^+e^- detector

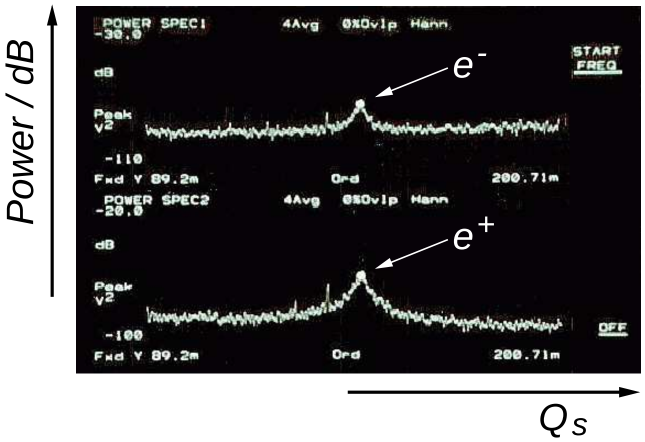

Fig. 7.3: *Synchrotron tune spectrum. The upper graph shows the signal of the electron channel, the lower graph the signal of the positron channel. This photograph was taken with a positron bunch current of 140 μA but without electrons.*

to distinguish between electron and positron signal. However there is residual cross-talk and the measurements should preferably be performed with only one beam in the machine to avoid this. Figure 7.3 gives a good illustration of this effect. The photograph shows the power spectrum of the synchrotron tune as derived from the phase detector output measured for a positron bunch current of 140 μA but without electrons. In the ideal case, no electron signal would be present. The Q_s peak is clearly visible on both channels. The uncertainties of a measurement of Q_s are estimated to be 0.0003 from the RMS scatter of the manual reading.

7.2 Voltage Calibration

The energy determination s from Q_s are based on measurements of the synchrotron tune as function of the total RF voltage V_{RF}. The effective voltage however can be significantly different from the "naive" total RF voltage (the sum of all individual cavity voltages) due to voltage calibration, phasing and longitudinal alignment errors. A first crucial correction to eq. (7.1) consists therefore in introducing a "voltage correction factor" $V_{RF} \rightarrow g\ V_{RF}$. This factor g is mainly determined by the region of high Q_s where $Q_s^2 \propto g\ V_{RF}$. The energy measurement is strongly correlated to g as can be seen in figure 7.4 when the energy extracted from the fit is

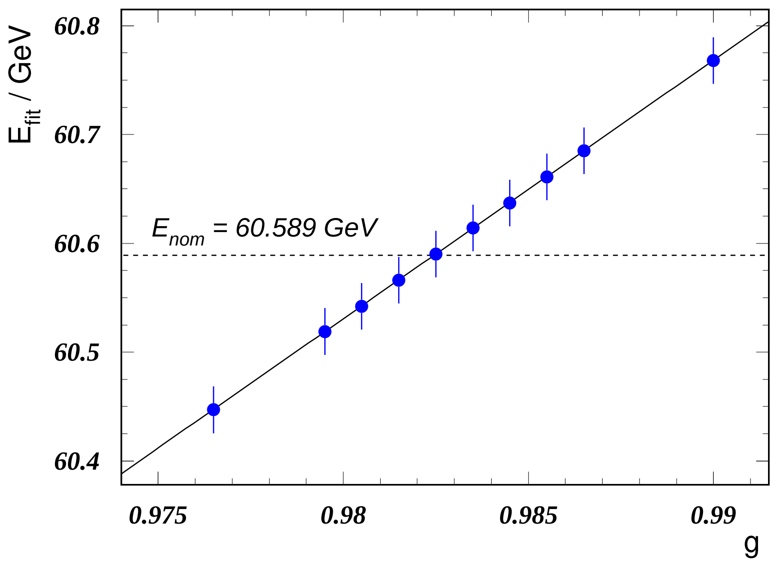

Fig. 7.4: *The fitted energy as function of the input parameter g for a test dataset taken at 60.589 GeV. The χ^2 of the fit increases strongly for extreme values of g.*

plotted as function of the voltage calibration g. At extreme values of g of course the χ^2 of the fit increases strongly. For a proper energy determination the value of g has to be determined from separate datasets. For that purpose measurements are performed at beam energies which have been previously determined very precisely with resonant depolarization. Using these calibration datasets the voltage correction factor is adjusted such that the known energy is reproduced by the fit. If several datasets are available the resulting g is the average over all values. The energy uncertainty due to the voltage correction factor is generally of the order of 10 MeV.

7.3 Total Energy Loss

Besides the main dipoles which are responsible for most of the energy loss, other smaller sources cannot be neglected. These additional losses originate from:

- synchrotron radiation due to beam position offsets in quadrupoles
- synchrotron radiation in corrector magnets used for beam steering
- parasitic mode losses caused by the resistive part of the longitudinal impedance
- synchrotron radiation due to finite beam sizes
- synchrotron radiation from energy offsets for non-central orbits

The energy loss due to synchrotron radiation in sextupole magnets is negligible. The total energy loss U_0 used in eq. (7.1) has to be written as

$$\tilde{U}_0 = \frac{C_\gamma}{\rho} E^4 + K \tag{7.2}$$

where K is the sum of all additional energy losses. The individual contributions to K are discussed in more detail below. The value K is assigned an overall uncertainty of 0.5 MeV which covers the uncertainties of the individual contributions. The energy error due to this uncertainty is of the order of 15 MeV.

7.3.1 Synchrotron Radiation Losses in Quadrupoles due to Position Offset and Finite Beam Size

To determine the energy loss in quadrupoles due to position offset and finite beam size it is useful to consider the basic equation for the instantaneous synchrotron radiation power:

$$P_\gamma = \frac{C_\gamma}{2\pi}\, c\, \frac{E^4}{\rho^2}. \tag{7.3}$$

With eq. (2.1) and eq. (2.3) the horizontal and vertical magnetic fields of a quadrupole can be written as $B_x = \frac{k\,p}{e}\, y$ and $B_y = \frac{k\,p}{e}\, x$ with k the normalized quadrupole strength eq. (2.3). The radius of curvature in the quadrupole field is $1/\rho = k\, u$ with $u \in \{x, y\}$ and the instantaneous synchrotron radiation power is

$$P_\gamma = \frac{c\, C_\gamma}{2\pi}\, E^4\, k^2\, u^2\,.$$

Integration over the time of flight through the magnetic field gives the expression for the energy loss per quadrupole

$$\Delta E_i = \int_{\Delta t_i} dt P_\gamma \;=\; \frac{c\, C_\gamma}{2\pi}\, E^4\, k^2\, u^2\, \frac{l_i}{c} \tag{7.4}$$

where l_i is the length of the quadrupole (l_i is 1.6 to 2 m in the case of LEP). This expression for the energy loss of a single particle can be generalized for a bunch with a Gaussian charge distribution, yielding the following integral:

$$\Delta E_i = \frac{C_\gamma\, l_i}{2\pi}\, k^2\, E^4 \int du\, \frac{1}{\sqrt{2\pi}\,\sigma_u}\, u^2\, e^{-\frac{1}{2}\frac{(u-u_0)^2}{\sigma_u^2}}. \tag{7.5}$$

A standard substitution $u = \sqrt{2}\sigma_u \xi, + u_0$ reduces this integral to a sum of tabulated integrals. It follows that the energy loss of a Gaussian bunch in the transverse coordinate u of a single quadrupole magnet is finally given by the quadratic sum of the center-of-charge position of the bunch and a contribution equivalent to the shift of the bunch position by one beam size:

$$\Delta E_i = \frac{C_\gamma\, l_i}{2\pi}\, k^2\, E^4 \left(\sigma_u^2 + u_0^2\right). \tag{7.6}$$

This example for a Gaussian distribution represents a special case of general properties of probability density functions. The same result holds for any non-negative function $f(x)$ with a normalization $\int_a^b dx\; f(x) = 1$, provided mean μ and variance σ_μ^2 exist. In general $a = -\infty$

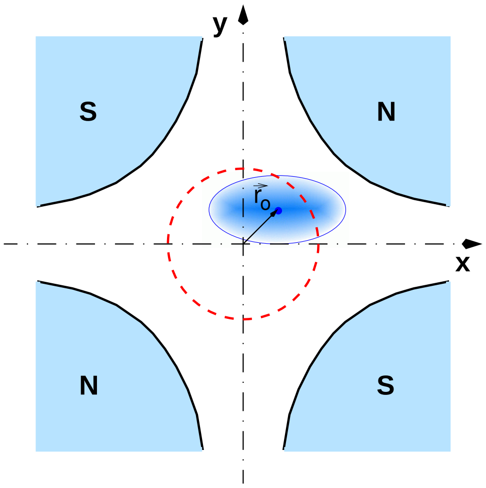

Fig. 7.5: *Sketch of a two-dimensional Gaussian charge distribution inside a quadrupole. The vector $\vec{r_0}$ points to the center-of-charge of a bunch of size (σ_x, σ_y). The dashed circle shows the equivalent radius for the energy loss due to finite beam size.*

and $b = +\infty$, for a realistic accelerator the limits are given by the physical boundaries of the vacuum chamber. The mean of the distribution $f(x)$ is defined by:

$$\int_a^b dx\ x\ f(x) = \mu.$$

The result (7.6) follows immediately from the definition of the variance:

$$\begin{aligned}
\int_a^b dx\ (x-\mu)^2\ f(x) &= \sigma_\mu^2 \\
&= \int_a^b dx\ \left\{x^2\ f(x)\right\}\ -\ \mu^2 \\
\Rightarrow \int_a^b dx\ x^2\ f(x) &= \mu^2 + \sigma_\mu^2.
\end{aligned}$$

Using this result the two-dimensional case is easily dealt with. Since the problem possesses a rotational symmetry in the $x-y$ plane ($P_\gamma \propto k^2(x^2+y^2)$), one can always find a transformation such that the two-dimensional distribution factorizes: $h(x,y) = f(x)g(y)$, where g fulfills the same conditions as f with mean ν and variance σ_ν^2, the integral can be written as

$$\begin{aligned}
&\int_a^b \int_c^d dx\ dy\ \left(x^2\ +\ y^2\right)\ h(x,y) \\
&= \int_a^b \int_c^d dx\ dy\ x^2\ f(x)\ g(y)\ +\ \int_a^b \int_c^d dx\ dy\ y^2\ f(x)\ g(y) \\
&= \int_a^b dx\ x^2\ f(x)\ +\ \int_c^d dy\ y^2\ g(y) \\
&= \mu^2 + \sigma_\mu^2\ +\ \nu^2 + \sigma_\nu^2.
\end{aligned}$$

For the limits c and d the same constraints as for a and b apply. The energy loss in two dimensions (transverse planes x and y) is finally:

$$\Delta E_i = \frac{C_\gamma\ l_i}{2\pi}\ k^2\ E^4 \left(x_0^2\ +\ y_0^2\ +\ \sigma_x^2\ +\ \sigma_y^2\right). \tag{7.7}$$

Equation (7.7) describes the complete energy loss in a quadrupole due to a position offset (x_0, y_0) and the finite beam size. The sketch of fig. 7.5 illustrates this result for a Gaussian charge distribution inside a quadrupole. The vector $\vec{r_0}$ points to the center-of-charge of a bunch of size (σ_x, σ_y) with the position offset (x_0, y_0). The dashed circle shows the equivalent radius for the energy loss due to finite beam size as described by eq. (7.7).

7.3.2 Synchrotron Radiation Loss due to the Sawtooth

The only systematic position offset in quadrupoles is caused by the energy sawtooth (see chapter 6). As the maximum amplitude of the sawtooth in quadrupoles for the optics in use and at energies up to 90 GeV does not exceed 2.6 mm (the horizontal beam size is often larger), this correction is small. Even at high energies its contribution to the energy loss is still small in comparison to the other contributions. The effect of the sawtooth is included in the loss due to closed orbit distortion (see 7.3.3).

7.3.3 Synchrotron Radiation Loss due to Closed Orbit Distortion

The total energy loss due to closed orbit distortions is estimated by summing up the individual contributions of all 808 quadrupoles, calculated from the measured closed orbit RMS of the transverse planes according to eq. (7.4). The closed orbit RMS is typically 0.5 mm in both planes with extremes of 0.3 and 0.9 mm. For a beam energy of 94.5 GeV an arc quadrupole generates an energy loss of 0.4 keV for a position offset of 0.5 mm. As the measured RMS is determined only from position measurements close to the defocusing quadrupoles the actual positions at the focusing quadrupoles are extrapolated using the local β-function. The losses due to sawtooth and closed orbit distortion add linearly due to the statistical nature of the latter: $\langle (u \pm \varepsilon)^2 \rangle = \langle u^2 \rangle + \langle \varepsilon^2 \rangle$ where u stands for a position offset and ε for a normal distributed variable (as estimate for the local orbit distortion). Since the energy sawtooth is part of the measured closed orbit, this effect is automatically taken into account and no additional sawtooth correction has to be applied. The uncertainty due to the measurement and the β-function extrapolation is estimated to be $\pm$ 15% for this contribution to the energy loss .

7.3.4 Synchrotron Radiation Loss due to Momentum Offset

A momentum offset $\Delta p/p$ can be introduced by a difference between the operation frequency f_{RF} and the central frequency f_{RF}^c. Such a difference can (among other causes) be due to tidal deformations of the earth. Figure 7.6 shows the calculated change in frequency due to tide effects for the duration of one series of measurements (see [37,38]). The offset in momentum or, neglecting the electron's rest mass, in energy is given by eq. (4.7):

$$\frac{\Delta p}{p} = -\frac{1}{\alpha_c} \frac{(f_{RF} - f_{RF}^c)}{f_{RF}^c}.$$

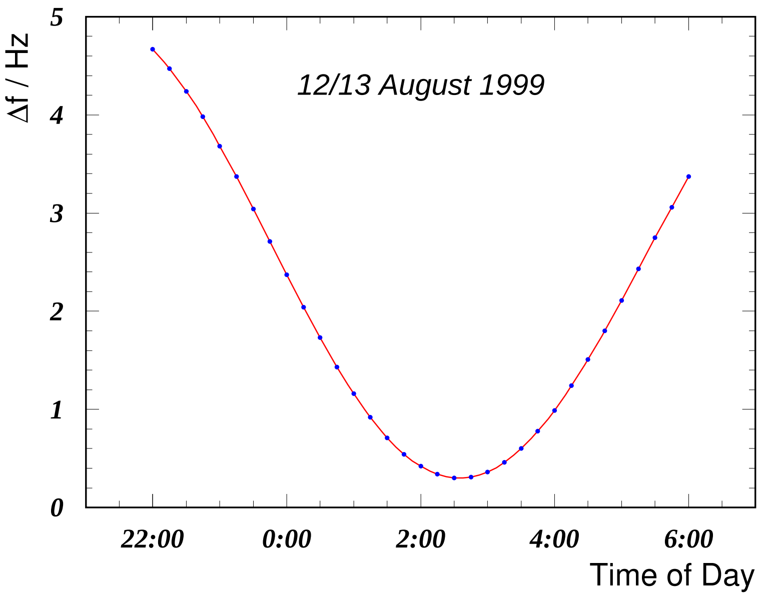

Fig. 7.6: *Calculated variation of the central frequency due to tidal deformations during one series of measurements.*

In such a case of non-zero momentum offset the energy is not matched to the dipole energy and the beam moves off-center in the quadrupoles. Since the position offset is proportional to $\Delta p/p$, one expects a quadratic dependence of the energy loss on $\Delta p/p$ according to eq. (7.6). Figure 7.7 shows how the relative energy loss changes with momentum deviation for two different energies. The deviation at low and high beam energies is sufficiently similar to find a common parameterization on which the calculation of corrections can be based. Usually the

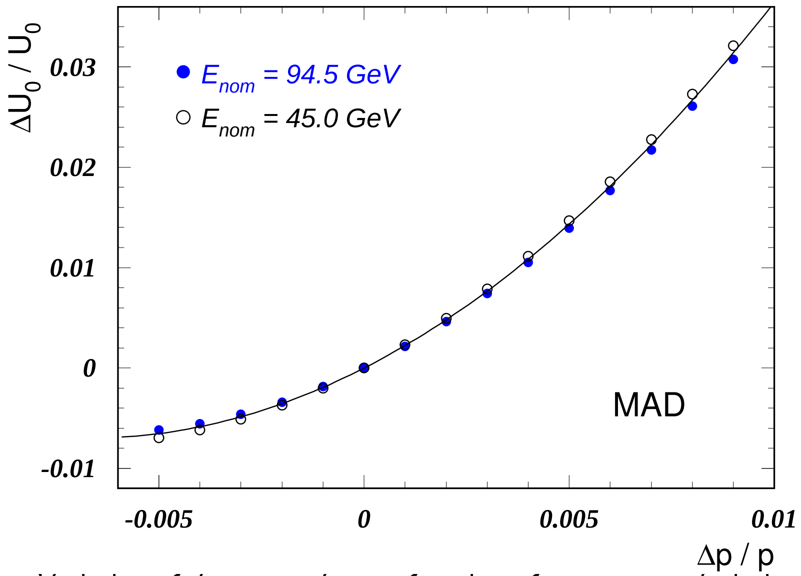

Fig. 7.7: *Variation of the energy loss as function of momentum deviation for 45 and 94.5 GeV as calculated with* MAD*.*

momentum deviation from frequency shifts is small ($\mathcal{O}(10^{-4})$) and therefore the contribution to the additional energy losses is also small. For a non-central orbit the energy E in eq. (7.1) must be replaced by

$$E_c = E + \Delta E = E\,(1 + \Delta p/p) \tag{7.8}$$

for $E = pc$, the energy E being by definition the energy on the central orbit. The relative uncertainty of the energy loss due to momentum offsets is ± 10%.

7.3.5 Synchrotron Radiation Loss in Corrector Magnets

Corrector magnets are small dipoles providing a deflection θ over a length l_i. The energy loss is easily calculated from $1/\rho = \theta/l_i$ with eq. (7.4):

$$\Delta E_i = \frac{c\,C_\gamma}{2\pi}\,E^4\,\left(\frac{\theta}{l_i}\right)^2\,\frac{l_i}{c} \;=\; \frac{C_\gamma}{2\pi}\,E^4\,\frac{\theta^2}{l_i}.$$

The length of a corrector magnet is $l_i^{\rm eff} = 51$ cm. A typical vertical correction is about 10 µrad which corresponds to an energy loss per vertical corrector of 22 eV at 50 GeV. Typical horizontal corrections are about 20 µrad corresponding to an energy loss of 0.1 keV per horizontal corrector for the same energy. 260 horizontal and 310 vertical correctors are installed in LEP. The actual energy loss is calculated from the measured kick RMS and is assigned an uncertainty of ± 5%.

7.3.6 Parasitic Mode Losses

Besides the synchrotron radiation in the bending dipoles the so-called parasitic mode losses are the largest contribution to the total energy loss. A beam traversing an impedance loses a certain amount of energy [7, 8, 14, 47]. This impedance consists of resistive wall contributions as well as of contributions from any resonator-like structure. The energy loss per turn of revolution period $T_{\rm rev}$ and particle is given by $U_{\rm pm} = e\,T_{\rm rev}\,I_b\,\kappa_{||}$. The longitudinal loss factor $\kappa_{||}$, usually given in units V/pC, is

$$\kappa_{||} \;\propto\; \int_0^\infty d\omega\;{\rm Re}Z_{||}(\omega)\;h(\omega,\sigma)$$

where $h(\omega,\sigma)$ is the spectral power density of the bunch of RMS length σ and ${\rm Re}Z_{||}(\omega)$ the longitudinal resistive impedance. In order to determine the effective parasitic mode losses, measurements of Q_s as function of RF voltage at an energy of 60.589 GeV were repeated for five bunch currents (10, 42, 100, 140 and 640 µA). Figure 7.8 shows these measurements. The curve represents a prediction of the MAD program. At first look there is no difference between the datasets. A closer look to the low voltage region (fig. 7.9) however reveals the difference in energy loss due to parasitic mode losses. The curves in fig. 7.9 are individual fits of the final fit model eq. (7.10) to the 10 and 640 µA datasets. A global (simultaneous) fit to all five datasets allows to extract an effective loss factor $\tilde{\kappa}_{||} = 10^3\,e\,T_{\rm rev}\,\kappa_{||}$ in MeV/mA. The model describes the data very well as indicated by the fit residuals of the simultaneous fit in fig. 7.10 on page 75.

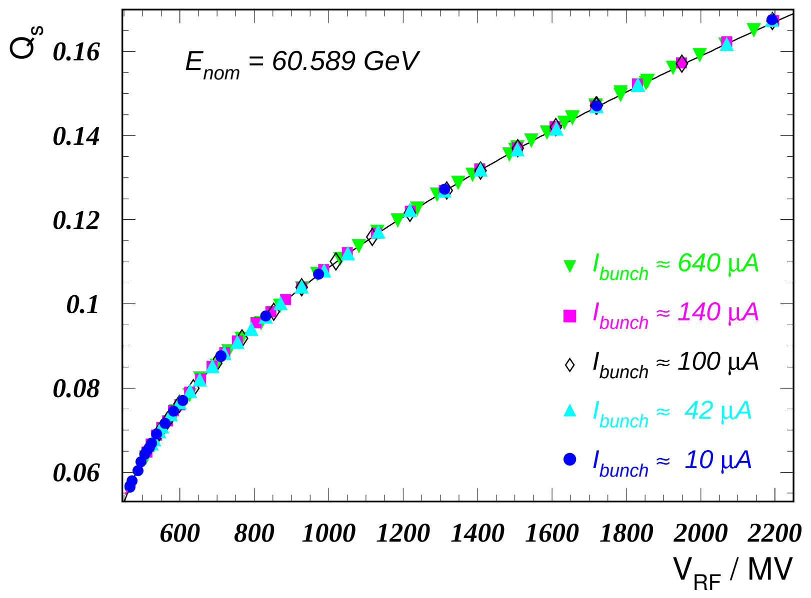

Fig. 7.8: Q_s *as function of total RF voltage. Measurements for five different bunch currents at a beam energy of 60.589 GeV are shown. The black curve is a prediction of the* MAD *program.*

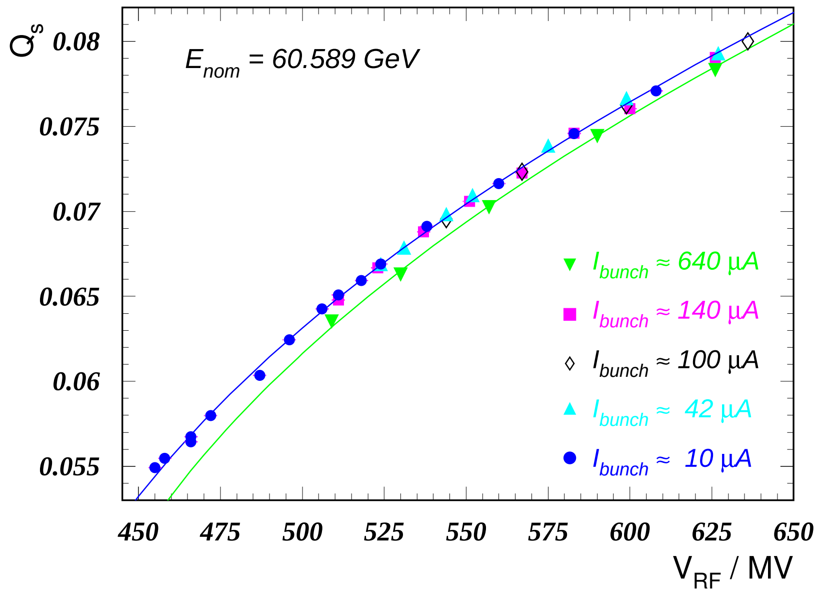

Fig. 7.9: Q_s *as function of total RF voltage. Same data as in fig. 7.8 but only the low voltage region is plotted. The two curves are individual fits to the 640 μA and 10 μA datasets. The difference in energy loss (parasitic mode losses) is clearly visible.*

The total loss factor determined from the fit is $\tilde{\kappa}_{||} = (18.5 \pm 2.0)$ MeV/mA. This $\tilde{\kappa}_{||}$ is composed of contributions from the arcs of the machine and contributions from the superconducting and

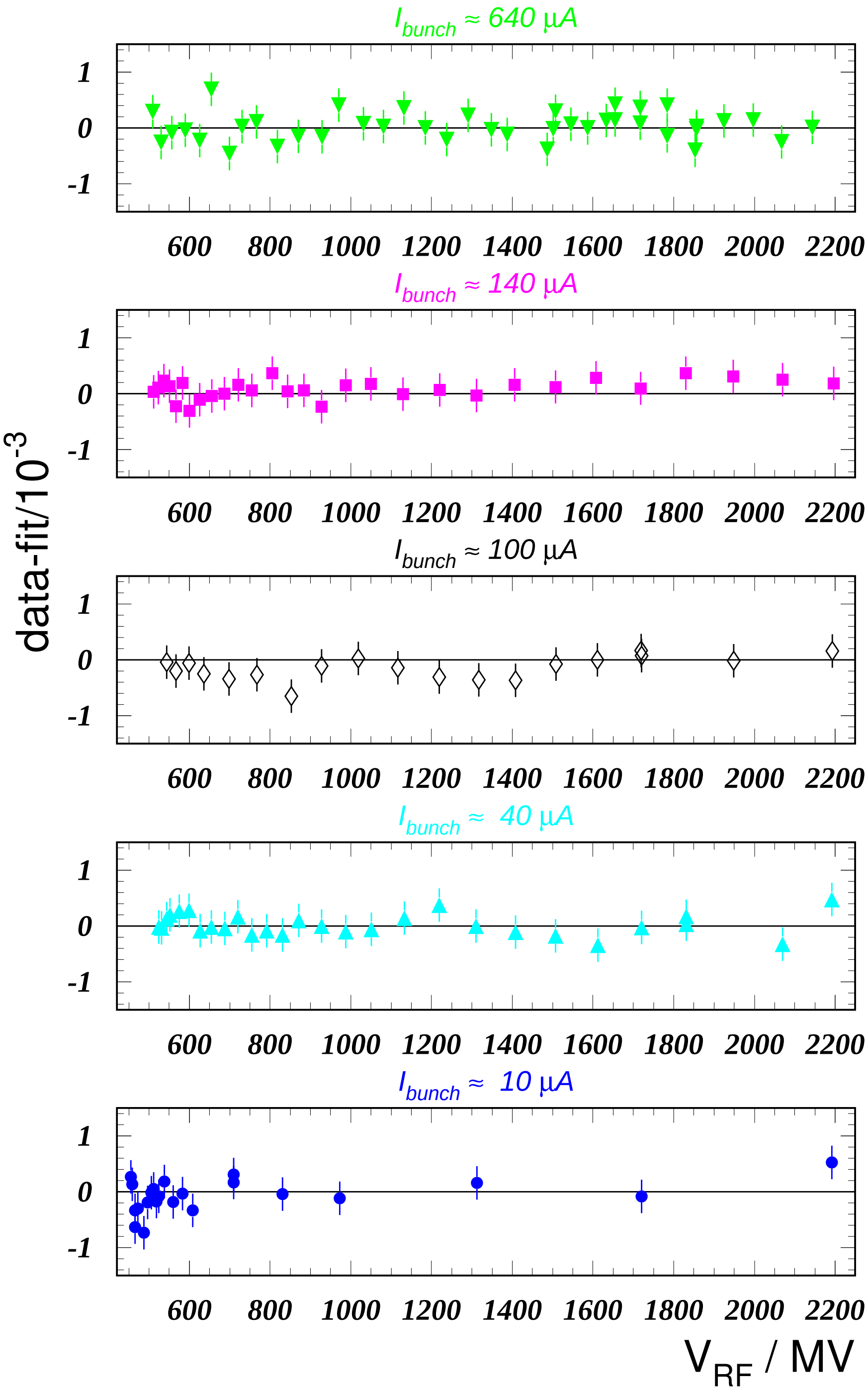

Fig. 7.10: *Differences between data and fit for a global (simultaneous) fit to all five datasets of fig. 7.8. The residuals of the individual datasets are shown in different plots.*

copper RF cavities. The contribution of the arcs (from pumping holes, beam pipe, etc.) is small (6.1 MeV/mA for all arcs according to [50]). The effective loss factor determined in the global fit was assumed to be constant over one dataset. In fact, this is only approximately the case: For

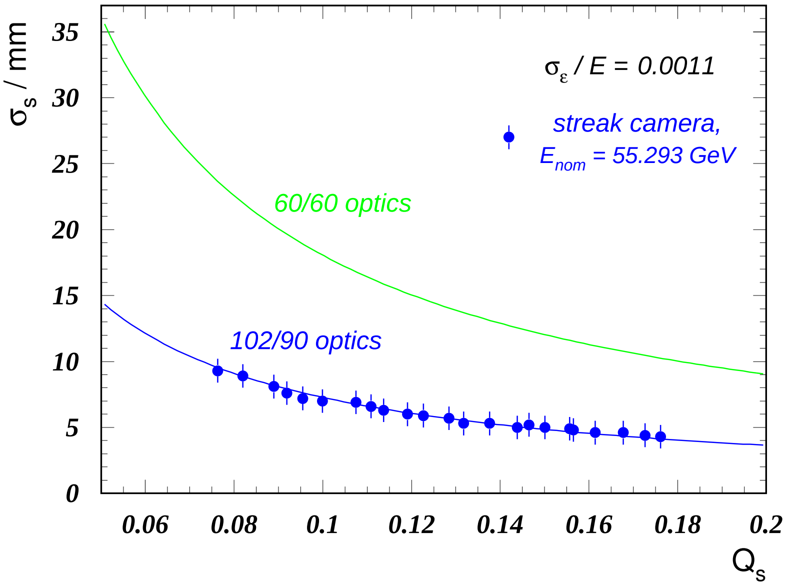

Fig. 7.11: *Evolution of bunch length as function of Q_s for an energy spread of 0.11% for different optics as calculated using eq. (7.9) and measurements with the streak camera.*

a resonant cavity in a storage ring, $\kappa_{||}$ is given by a sum over modes up to the cut-off frequency, plus a high frequency diffraction [51,52] contribution leading to $\kappa_{||} \propto 1/\sqrt{\sigma_s}$ [14]. The loss factor is expected to vary with the bunch length which changes considerably over the Q_s range of the measurements. The relation between Q_s and bunch length is

$$\sigma_s = \frac{1}{Q_s} \frac{c\ \alpha_c}{\omega_{rev}} \frac{\sigma_\varepsilon}{E_0} \tag{7.9}$$

with σ_ε/E_0 the energy spread . Due to the dependence on the momentum compaction factor the bunch length depends on the machine optics. Figure 7.11 shows the calculated bunch length as function of the synchrotron tune for the $60^o/60^o$ and the $102^o/90^o$ optics which were used for the measurements. The calculations for the $102^o/90^o$ optics are overlaid by direct measurements with the streak camera (a device to measure the bunch length using synchrotron light [53]). To test the dependence of $\kappa_{||}$ on the bunch length, the loss factor in the global fit was replaced by $\kappa_{||} = \kappa_{||}^0\ (\sigma_s/\sigma_s^0)^{\alpha_L}$, where σ_s^0 is an arbitrary normalization. The resulting exponent was $\alpha_L = 0.05 \pm 0.19$ (consistent with zero) with a 99% correlation between α_L and $\kappa_{||}^0$. A single dataset shows no sensitivity to the bunch lengthening. This fact can be understood as a feature of the fit method: the parasitic losses are a small contribution to the total energy loss and the fit is not very sensitive to small variations which can in addition be effectively absorbed by other parameters. In a single dataset there is no dependence on σ_s to be taken into account. For the comparison of datasets of different optics however, the measured loss factor is rescaled with the inverse ratio of the square roots of the average bunch lengths for each optics. The calculated energy loss due to parasitic mode losses is assigned a relative error of $\pm$ 20%.

7.3.7 Synchrotron Radiation Loss in Dipole Fringe Fields

The effective average magnetic radius of the bending dipoles in eq. (7.2) extracted from MAD is 3025.85 m. Figure 7.12 shows a sketch of the dipole field. Ideally the field of a magnet of

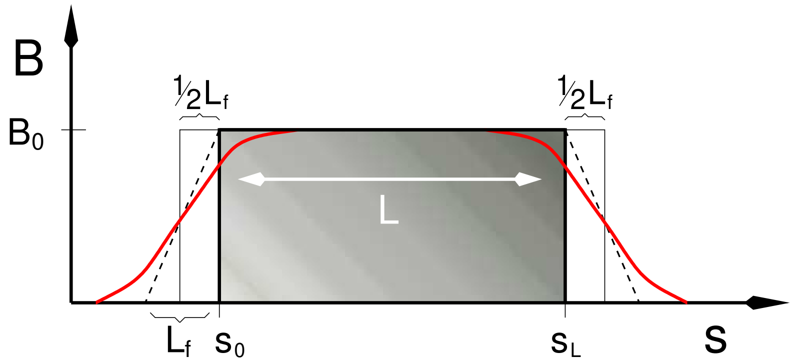

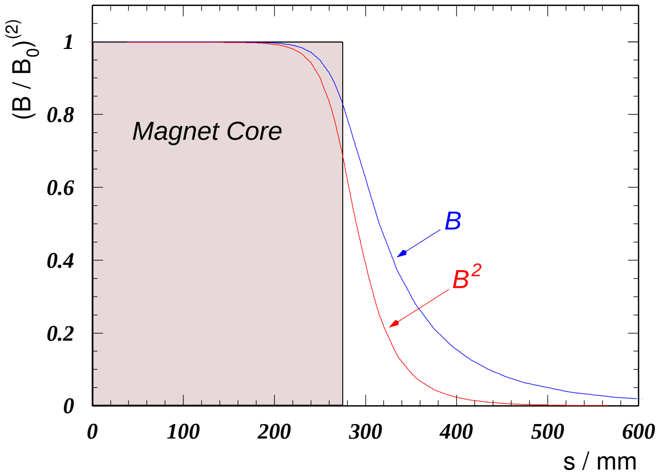

Fig. 7.12: *Sketch of the magnetic field of a bending dipole. Field distributions with and without (shaded area) fringe fields are sketched (top). Field distribution at the end of a dipole magnet as modeled for the LEP dipoles [54]. The magnetic field and the square of the field are shown (left).*

length L should jump to its nominal value B_0 at the start of the magnet s_0 and back to zero at the end s_L. In reality the field "leaks" out as indicated by fig. 7.12. This field is known as "fringe field". To keep the integral of the magnetic field over the length of the magnet $(\int B ds)$ constant, a simulation program can use either magnets of an effective length $L + L_f$ with the constant field B_0 or magnets of length L with a higher field B_1 where $B_0(L + L_f) = B_1 L$. The latter option is used in the simulation program MAD. The energy loss is proportional to the integral over the square of the magnetic field $(\int B^2 ds)$. Obviously the square of the magnetic field can be approximated by the square of the rectangular field of length L (see bottom plot of fig. 7.12). There remains however a small difference between this approximation and the real energy loss which was calculated by numerically integrating the actual magnetic field taking into account the measured fringe fields in between the LEP dipole pairs. The determination of this correction and the measurement of the fringe fields are described in detail in appendix C. The inverse radius determined that way is 1.6 % smaller than the value extracted from MAD. However the fits clearly prefer a smaller value of the correction as is shown in C.2. The correction of ρ^{-1} used in the fits was based on a preliminary estimate of 0.28%. The study of appendix C indicates how the radius correction can be determined by future measurements. For the time being the uncertainty (bias) in the energy due to the imperfect knowledge of the radius is assumed to be $\delta E = 15$ MeV, which corresponds to a change in ρ^{-1} by 0.1%.

7.4 The Momentum Compaction Factor

The momentum compaction factor α_c shows a small energy dependence which is due to a difference between the true and the nominal dipole field and thus the actual energy. This difference leads to a mismatch of quadrupoles and dipoles in the lattice which in turn leads to a small change of α_c. Usually the energy shift is small ($\mathcal{O}$(20 MeV)). Figure 7.13 shows the momentum compaction factor from a MAD simulation [36] for a 102°/90° optics as function of the difference between nominal and true beam energy. If no correction for this effect is applied in the fit, a bias-type uncertainty of $\delta E \sim 10$ MeV has to be added to the energy.

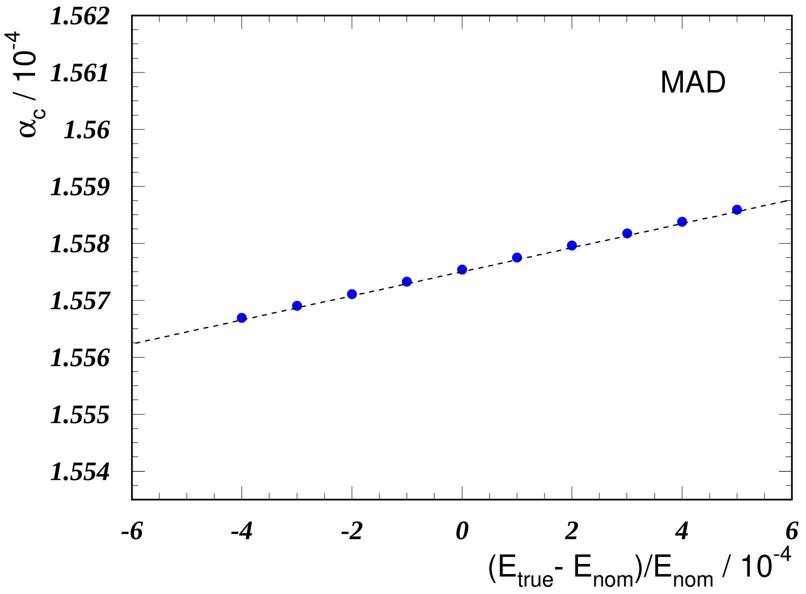

Fig. 7.13: *Momentum compaction factor on the central orbit for a fixed tune from a MAD simulation for a 102°/90° optics as function of the difference between nominal and true beam energy from [36]. For a beam energy of 100 GeV a value of $5{\cdot}10^{-4}$ corresponds to an energy shift of 50 MeV.*

If the energy is known from other measurements (resonant depolarization) the same fits can be used to extract the momentum compaction factor. The relative uncertainty resulting from this method is $\Delta\alpha_c/\alpha_c \approx 1{\cdot}10^{-3}$ whereas conventional measurements have relative uncertainties of 1 - 2%. All measurements of the momentum compaction factor are in good agreement with the MAD value.

7.5 RF Distribution

In LEP the RF cavities are concentrated in four straight sections. The MAD program was used to study the dependence of Q_s on the distribution of the RF voltage. Figure 7.14 shows Q_s generated for a beam energy of 50.005 GeV with different RF configurations: a realistic case with the standard LEP RF distribution, a case where the same total voltage is concentrated in one point and the limit of a homogeneous distribution where the voltage is distributed over the whole ring. To account for the RF distribution, a term proportional to V_{RF}^4 has to be added to

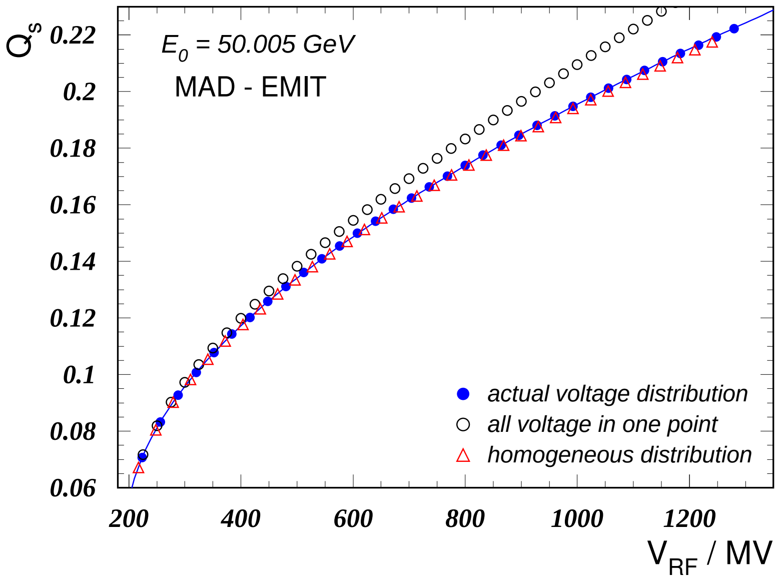

Fig. 7.14: *Synchrotron tune as function of total RF voltage as calculated with* MAD *for different RF configurations. The curve is a fit to the "realistic" RF distribution using the fit model eq. (7.10) with appropriate input parameters.*

eq. (7.1) beneath the square root. The weight factor M is taken from a fit to the MAD dataset. This factor includes the corrections of the model needed to account for the approximations in the derivation of the analytical model of eq. (7.1).

7.6 Final Model, Fit Parameters and Constraints

Taking into account all effects described in the previous sections the final model reads as follows:

$$Q_s^4 = \left(\frac{\alpha_c h}{2\pi}\right)^2 \left\{ \frac{g^2 e^2 V_{RF}^2}{E_c^2} + M g^4 V_{RF}^4 - \frac{1}{E_c^2}\,\tilde{U}_0^2 \right\} \tag{7.10}$$

with the relations from equations (7.8,7.2). A fit of this model to simulation data shows a good agreement between the extracted fit energy and the input energy. The momentum compaction factor α_c and the voltage nonlinearity factor M are taken from MAD. All other parameters are allowed to vary in the fit. External knowledge is incorporated in the fit by introducing constraints

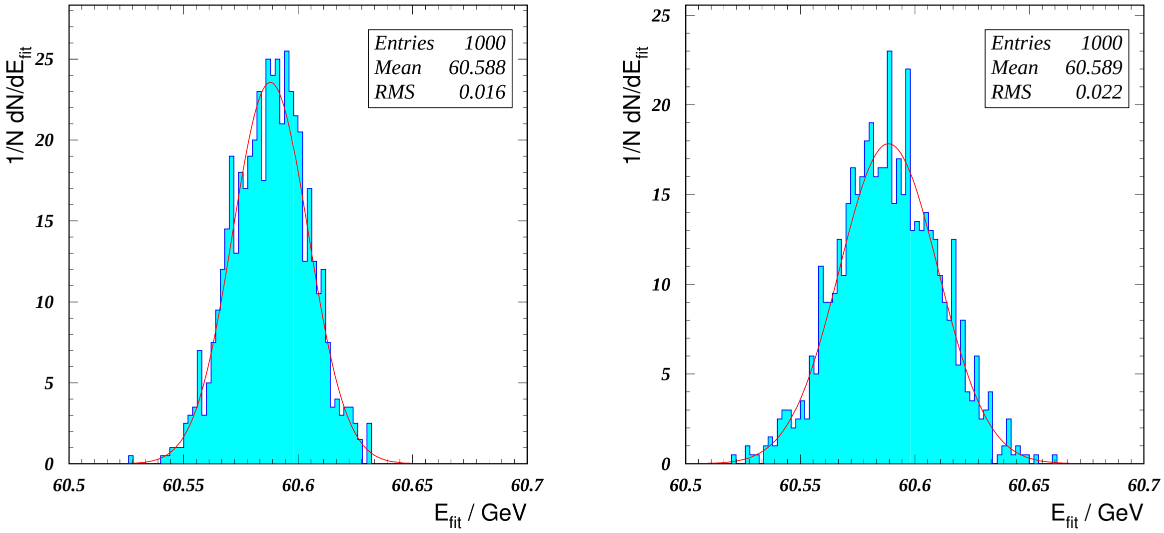

Fig. 7.15: *Result of the Monte Carlo simulation with variation of all fit parameters on the left side and an additional variation of the measured data on the right side. In either case the fit to the same dataset was repeated 1000 times with the same input parameters varied within their uncertainties.*

of the type $(a - a_{\text{nom}})^2/\sigma_a^2$ for all parameters where a stands for a fit parameter and σ_a for its uncertainty. The value the parameter is constrained to is denoted by a_{nom}. The parameters for additional energy losses, voltage calibration and the weight factor M are constrained in the described way. Table 7.3 contains a detailed overview over all input parameters and constraints used for energy determinations.

A Monte Carlo technique was used to estimate the systematic contributions of the parameter constraints to the error of the fit energy. The test dataset gave a beam energy of 60.588 ± 0.0023 GeV with the "standard" fit. The regular fit to the same dataset was repeated 1000 times with the input parameters varied within their uncertainties, the Q_s data were left unchanged. Only α_c and M were kept constant. The result of this Monte Carlo is shown in the left hand plot of fig. 7.15. The RMS uncertainty of the resulting fit energy caused by the parameter variations is 16 MeV in this case. This error is the systematic contribution of all input parameters. To verify the method the Monte Carlo simulation was repeated, this time with additional variation of the measured Q_s within its error. The resulting RMS uncertainty of 22 MeV is in good agreement with the regular fit error. The distribution of the resulting fit energies is shown in the right hand plot of figure 7.15. The final error on the beam energy is composed of a "statistical-type" uncertainty $\pm\Delta E$ due to the uncertainties of Q_s, g and K and a "bias-type" uncertainty $+\delta E$ due to the momentum compaction factor and the dipole fringe fields. This "bias-type" uncertainty $+\delta E$ is of the order of 18 MeV.

7.7 Results

All measurements used for voltage calibration or an energy determination are listed in tab. 7.1. The datasets are given in chronological order with optics, nominal beam energy and a comment describing its purpose if the data quality was sufficiently good. The input parameters for the

No.	E_{nom} / GeV	optics	year	comment
1	50.005	$60^o/60^o$	1998	voltage calibration, energy determination
2	60.589	$60^o/60^o$	1998	voltage calibration, energy determination
3	66.046	$102^o/90^o$	1998	voltage calibration
4	90.419	$102^o/90^o$	1998	energy determination
5	60.589	$102^o/90^o$	1999	determination of loss factor, five currents
6	50.005	$102^o/90^o$	1999	unstable conditions
7	55.293	$102^o/90^o$	1999	voltage calibration
8	60.589	$102^o/90^o$	1999	voltage calibration
9	80.000	$102^o/90^o$	1999	energy determination

Tab. 7.1: *All datasets used for analysis. Nominal energy, optics and purpose of the datasets are given.*

different fits were determined in the way described in the previous sections. Table 7.2 gives estimates of the different contributions to the total energy loss other than the synchrotron radiation loss in dipoles. The values in tab. 7.2 were calculated for a $102^o/90^o$ optics and comparable bunch currents. Whenever possible, the voltage calibration factor g was determined from one or more independent measurements (see tab. 7.1). All constraints and input parameters

energy loss mechanism	energy loss [MeV]		
	50.005 GeV	60.589 GeV	80.000 GeV
quad. / closed orbit (included sawtooth)	0.1 (0.002)	0.2 (0.015)	0.6 (0.25)
correctors	0.05	0.1	0.3
mom. offset (f_{RF}^c / tide)	-0.1	-0.3	-0.9
beam size	0.1	0.3	1.7
parasitic mode loss	1.1	1.07	1.02
$\sum = K$	1.25	1.37	2.72

Tab. 7.2: *Estimates of the additional energy losses for beam energies of 50.005, 60.589 and 80.000 GeV with comparable momentum offsets and bunch currents of around 50 μA. The individual contributions were calculated for a $102^o/90^o$ optics. The overall uncertainty assigned to the sum K is $\Delta K = \pm$ 0.5 MeV.*

No.	E_{nom} / GeV	$g \pm \Delta g$	$K \pm \Delta K$ / MeV	M / GV^{-4}	E_0 / GeV
1	50.005	0.9511 ± 0.0006	0.94 ± 0.50	6.278 10^{-6}	50.020
2	60.589	0.9511 ± 0.0006	1.65 ± 0.50	2.520 10^{-6}	60.597
9	80.000	0.9730 ± 0.0019	3.36 ± 0.50	0.081 10^{-6}	80.012
4	90.419	0.9494 ± 0.0006	3.77 ± 0.50	0.090 10^{-6}	90.458

Tab. 7.3: *Constraints and inputs for all datasets used for an energy determination. The parameters were allowed to vary in the fit within their uncertainties. E_0 is the reference energy from polarization or magnetic measurements.*

used for energy determinations are shown in tab. 7.3, ordered by beam energy.
The upper plot of figure 7.16 on the next page shows datasets 1 and 2 (the measurements at 50.005 and 60.589 GeV with the 60°/60° optics). The curves are best fits using the final model of eq. (7.10). The voltage calibration factor for datasets 1 and 2 is given by the average, its error by the half distance of the values determined from the two datasets. The bottom plot of fig. 7.16 shows the residuals of the fit to the 50.005 GeV data (note that the ordinate scale is different from the scale of fig. 7.10 on page 75). It is clearly visible that the model is able to reproduce the measurements accurately.
The datasets 6 to 9 are shown in fig. 7.17 on page 84. The data were taken in parallel to a cryogenics plant regeneration. The voltage calibration factor was determined from datasets 7 and 8, the first dataset 6 yields a g value completely inconsistent with the other two datasets and is ignored. The bottom plot of fig. 7.17 shows the difference between data and fit of dataset 9 at 80.000 GeV. The low and high voltage regions seem to be consistent but the region between 1450 and 2200 MV shows a strange behavior which could also be due to an influence of the cryogenics plant regenerations (for example induced cavity oscillations). Nonetheless an energy was determined for dataset 9 (see tab. 7.4).
Figure 7.18 shows the datasets labeled as 3 and 4. The measurements were done with two beams with four bunches each and eight different bunch currents. Only electron signals are used. As

No.	E_{nom}/GeV	optics	E_{pol}/GeV	E_{nmr}/GeV	E_{fit} ± stat. ± sys. / GeV	$\Delta E/E$
1	50.005	60°/60°	50.020	50.015	50.044 ± 0.014 ± 0.029	6.4 10^{-4}
2	60.589	60°/60°	60.597	60.594	60.586 ± 0.012 ± 0.021	4.0 10^{-4}
9	80.000	102°/90°	–	80.012	79.995 ± 0.011 ± 0.018	2.6 10^{-4}
4	90.419	102°/90°	–	90.458	90.444 ± 0.007 ± 0.017	2.0 10^{-4}

Tab. 7.4: *Results of the fits using the model of eq. (7.10). The contribution to the error labeled as "sys." represents the error due to the uncertainties of the model parameters. An additional overall bias-like uncertainty due to uncertainties in machine parameters is of the order of 18 MeV. The NMR energies are determined in the way described in chapter 4.*

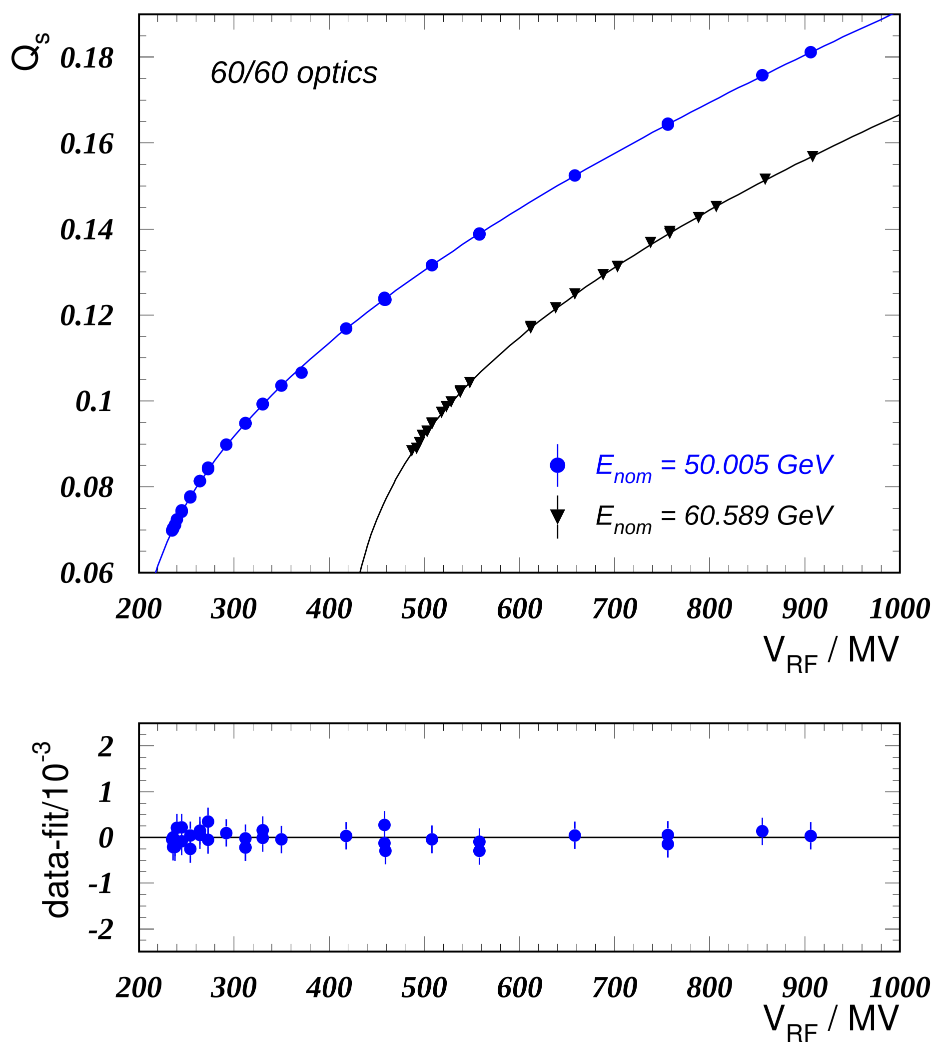

Fig. 7.16: *Measurements of Q_s as function of total RF voltage with the 60°/60° optics. The curves are the results of the fits according to eq. (7.10) (top). Difference between data and fit for the fit to the 50.005 GeV data (bottom).*

was already mentioned in section 7.1, these measurement conditions can lead to systematic uncertainties. The systematic effect on the beam energy due to the different e^- bunch currents was estimated from the difference in fit energy for fits with the assumption of minimum and maximum bunch current: $\Delta E_{sys}(I_b) \approx \pm$ 3 MeV. The voltage calibration factor was determined from dataset 3. The lower plot of fig. 7.18 shows the residuals of the fit to the 90 GeV data.
In table 7.4 the fit results are compared to the nominal machine energy (obtained from the magnet calibration curves) and to the energies measured with resonant depolarization in the following fill or estimated with magnetic measurements as described in chapter 4. For all measurements the fitted energies agree within their errors with the energies obtained from other methods. The absolute error is essentially energy independent and of the order of 20 MeV. The overall systematic bias-like error due to the uncertainties in the machine parameters (α_c, ρ),

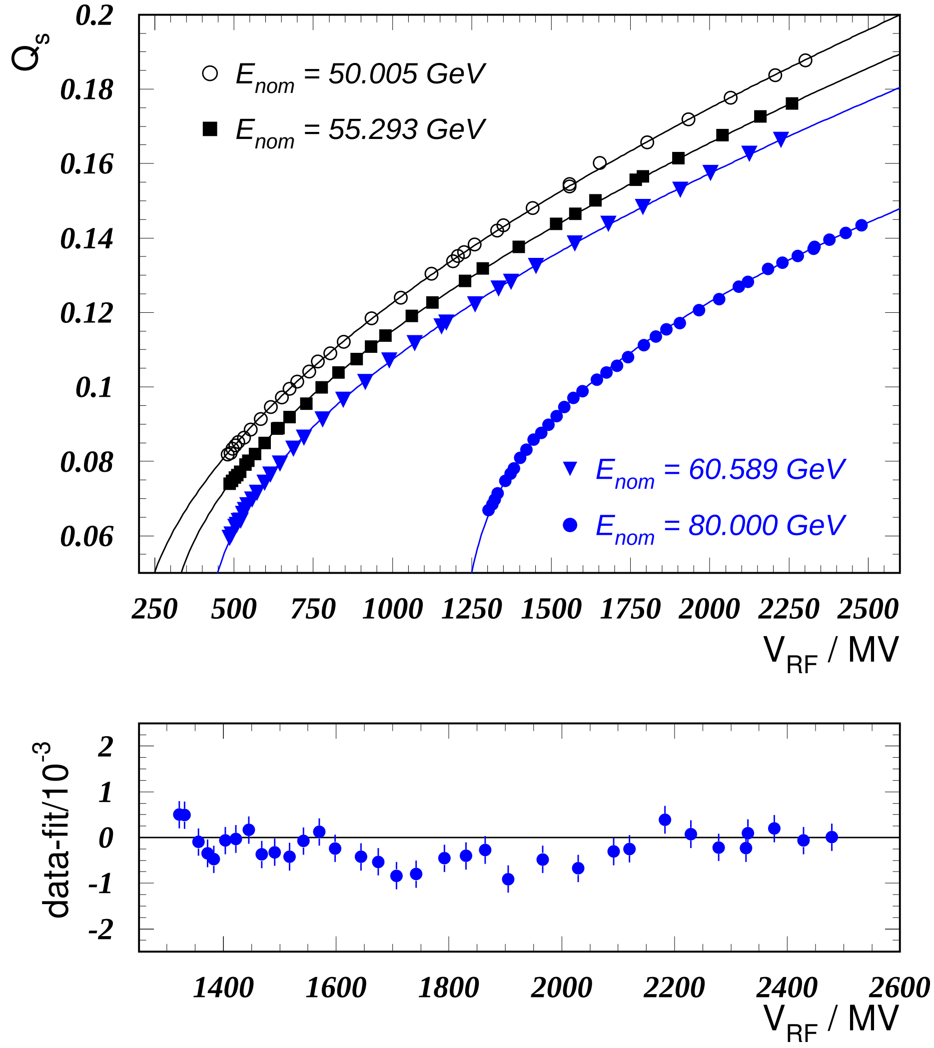

Fig. 7.17: Q_s *as function of total accelerating voltage measured with the* $102^o/90^o$ *optics. Datasets of measurements at different energies are shown (dataset no. 6-9). The curves are fits to the individual datasets (top). Differences between data and fit for the fit to the 80 GeV data (bottom).*

currently of the order of 18 MeV, is expected to be reduced significantly by further studies. The radius can be determined by a dedicated measurement and the dependence of the momentum compaction factor on the difference between true and nominal beam energy can be incorporated into the fitting procedure.

This method to extract the beam energy directly from a fit to the measured synchrotron tune as function of total accelerating voltage represents a precise cross-check for the energy calibration of LEP. The systematics and uncertainties of the method are understood and under control. The error on the beam energy is of the required magnitude and can potentially be reduced by a better understanding of the momentum compaction factor and the bending radius of the LEP dipoles.

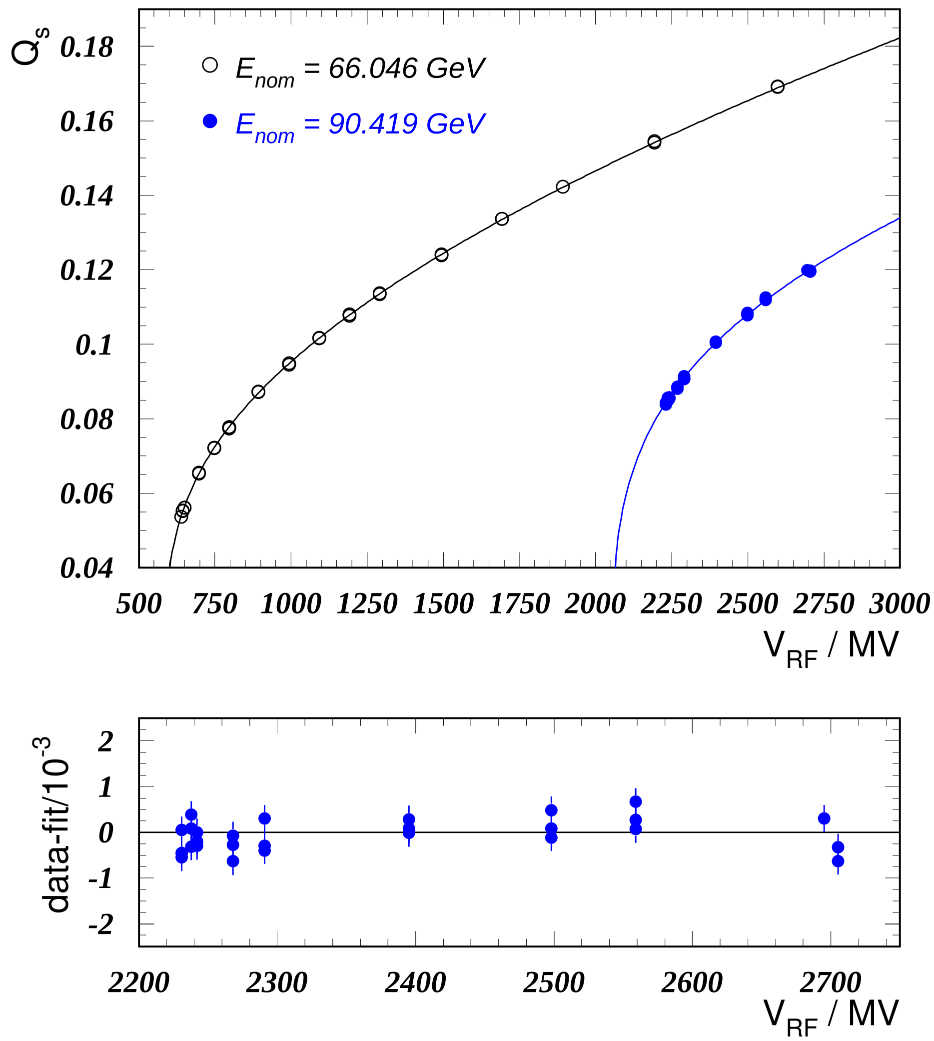

Fig. 7.18: Q_s *as function of total accelerating voltage measured with the* $102^o/90^o$ *optics. Datasets of measurements at different energies are shown (dataset no. 3,4). The curves are fits to the individual datasets (top).*
The residuals for the fit to the 90 GeV data are shown in the bottom plot.

Chapter 8

The Measurement of the W Mass

Before describing the measurement of the W mass a short description of the ALEPH detector and its sub-detectors will be given.

8.1 Layout of the ALEPH Detector

ALEPH like most collider detectors is a multi purpose instrument for particle identification and the detection of neutral and charged energies over the full solid angle. The detector has a cylindrical symmetry around the interaction point. A solenoidal magnetic field is used for a measurement of the particle momenta. High resolution vertex detectors are needed to reconstruct the decay of short lived particles (like for example the B meson). Detailed descriptions of the ALEPH detector can be found in [55, 56]. Figure 8.1 shows a cross-section of the ALEPH detector.

8.1.1 Definition of the Coordinate System

The ALEPH coordinate system is a right handed Cartesian system. The positive x axis points horizontally towards the center of the LEP ring, the positive z axis along the electron direction. The y axis denotes the vertical direction. Alternatively the system of choice is often a polar coordinate system (r, ϕ, θ) defined in the usual way:

$$x = r \sin\theta \cos\phi \qquad y = r \sin\theta \sin\phi \qquad z = r \cos\theta.$$

8.1.2 Vertex Detector and Inner Tracking Chamber

ALEPH's silicon strip vertex detector VDET provides coordinates of charged particle tracks very close to the interaction point. The high-precision of this position measurement is needed

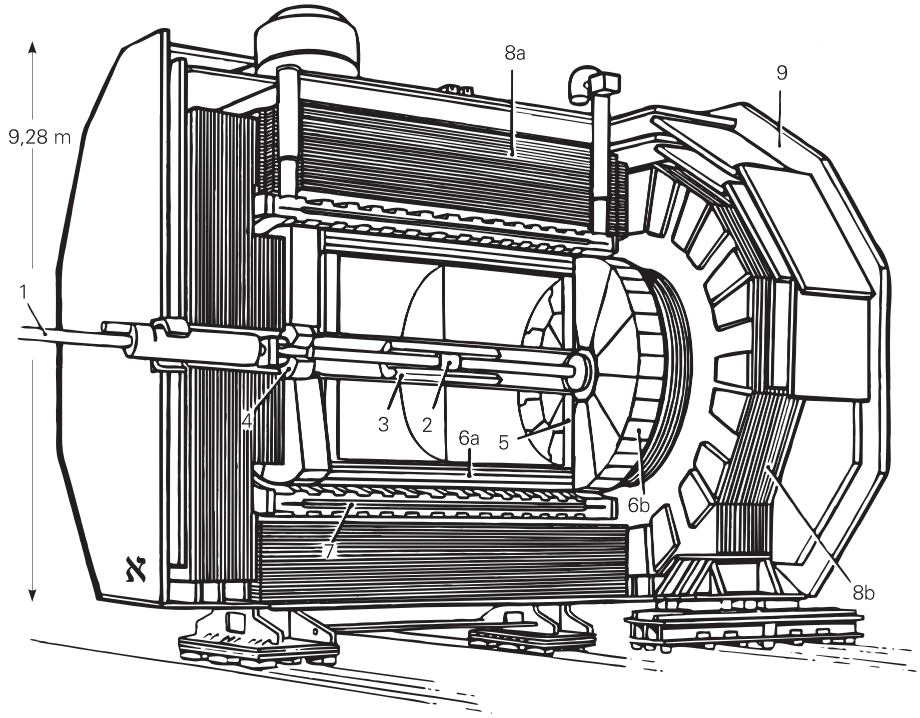

Fig. 8.1: *Cross-section of the ALEPH detector. The numbers denote the different sub-detectors or parts of ALEPH: (1) beam-pipe, (2) silicon vertex detector VDET, (3) inner tracking chamber ITC, (4) luminosity monitor LCAL, (5) time projection chamber TPC, (6a) electromagnetic calorimeter ECAL (barrel part), (6b) ECAL (end-cap), (7) superconducting magnetic coil, (8a) hadronic calorimeter HCAL (barrel part), (8b) HCAL (end-cap), (9) muon chambers.*

for the determination of the decay lengths of short lived particles like τ leptons or B mesons. VDET (upgraded in 1995) consists of two concentric layers of silicon wafers with an average distance of 63 mm and 110 mm from the beam axis. Each layer provides position information in the z direction and in the $r\phi$ plane. The 144 silicon wafers (dimension 52.6mm $\times$ 65.4mm) are double-sided detectors with one side measuring the azimuthal coordinate ($r\phi$), the other the impact point in beam direction (z). The spatial resolution obtained with VDET for a 90 degree incident particle is 15 μm in z direction and 10 μm in th $r\phi$ plane. The detector covers a sensitive region which extends to $\pm$ 20 cm in z direction, corresponding to an angular range of $-0.95 < \cos\theta < 0.95$.

The inner tracking chamber ITC is a cylindrical drift chamber which provides up to 8 $r\phi$ coordinates of charged particle tracks with 160 mm $\leq r \leq$ 260 mm and a fast signal for the level 1 trigger. The chamber is filled with 80% argon and 20% carbon dioxide at atmospheric pressure. The wires of the eight layers of drift cells are mounted parallel to the beam axis. The active length of the ITC is 2 m and its transverse resolution is 150 μm. The resolution in z direction - measured from the arrival time difference of the pulses on both sides of the ITC - is approximately 5 cm.

8.1.3 Time Projection Chamber and Magnetic Coil

The measurement of particle momenta needs a high-resolution tracking chamber inside a solenoidal magnetic field. ALEPH's central tracking chamber is a time projection chamber (TPC). The TPC is a hollow cylinder with an inner radius of 30 cm, an outer radius of 180 cm and a total length of 440 cm. The chamber is filled with an argon-methane mixture (91% : 9%) at atmospheric pressure. As figure 8.2 shows, the drift volume is divided into two halves by a central electrode that has a negative potential of about 26 kV with respect to the cathode wires of the planar drift chambers at both end caps. The voltage has been chosen to maximize the electrons drift velocity in the chamber gas. The particles produced in the e^+e^- collision

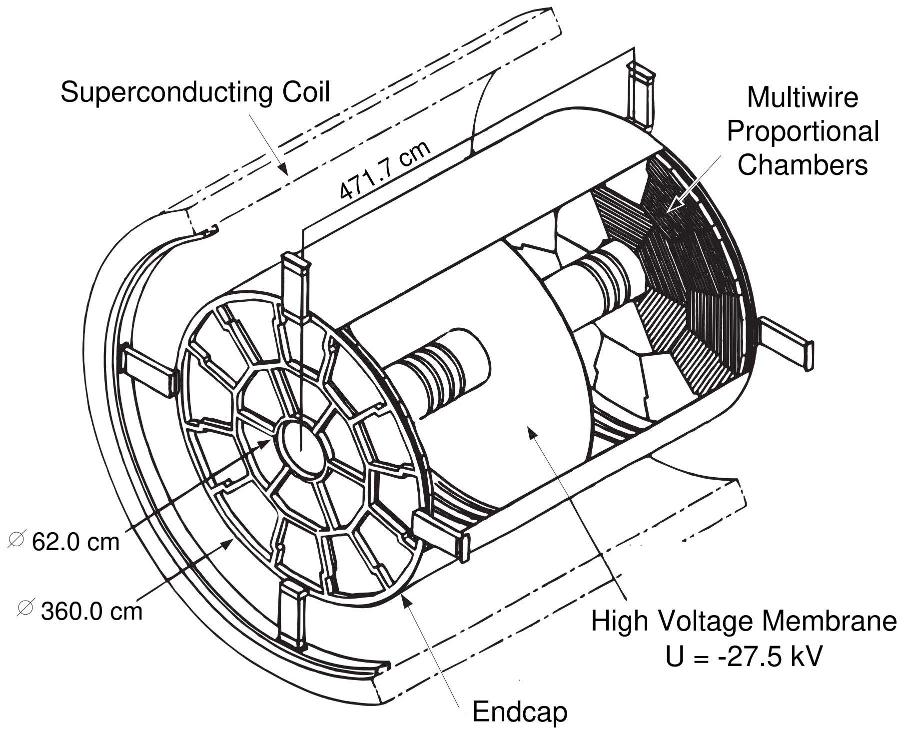

Fig. 8.2: *Layout of the ALEPH time projection chamber (TPC).*

create electron-ion pairs along their tracks. In the electric field of 115 V/m these free electrons drift towards the end cap with a velocity of about 5 cm/µs. Each end cap consists of 18 multi-wire proportional chambers ("sectors"). Each sector is composed of three layers: the first layer contains gating wires, the second cathode wires and the third layer consists of signal wires and field wires. The signal wires' potential difference with respect to the cathode wires is +1500 V. The "cells" work in the proportional mode which enables a measurement of charge and specific energy loss $\mathsf{dE/dx}$ of the particles crossing the TPC volume.

Under the signal wires reside cathode pads of the dimension 6.2 mm $\times$ 30 mm. The pads are grouped in 21 rows of constant radii. The electron avalanches produced at the signal wires induce pulses at the pads which are used for a position measurement in the $r\phi$ plane (transverse to the beam axis). The precision of this position measurement is approximately 180 μm. A drift time measurement yields the z coordinate (along the beam axis) with a precision of about 1mm. Each track passing through the chamber does therefore create a set of three-dimensional coordinates.

The momenta of the charged particles are determined from the curvature of their tracks in the magnetic field. The momentum resolution for a field of 1.5 T is

$$\frac{\Delta p_T}{p_T^2} = 1.2 \times 10^{-3} \ (\mathrm{GeV/c})^{-1}$$

with p_T the transverse momentum of the track with respect to the beam axis. Together with the coordinates obtained from ITC and VDET the resolution can be improved to be

$$\frac{\Delta p_T}{p_T^2} = 0.6 \times 10^{-3} \ (\mathrm{GeV/c})^{-1}.$$

The magnetic field of 1.5 T is generated by a superconducting solenoidal coil with a field homogeneity of

$$\frac{\Delta B}{B} < 0.2\%.$$

The energy stored in the magnetic field is 136 MJ. Solenoid and cryostat weigh 55 t.

8.1.4 Electromagnetic Calorimeter

The electromagnetic calorimeter (ECAL) is used for detection and identification of photons and electrons and the measurement of the energies of these particles. It consists of a central (barrel) part and two end caps. The ALEPH ECAL is a 45 layer sampling calorimeter made of lead sheets and proportional chambers. The chambers are operated with a mixture of 80% Xenon and 20% CO_2. Below the wires are cathode pads of the size 3×3 cm^2. The layers are clustered in stacks of 10, 23 and 12 layers from the inside to the outside. The amount of material in radial direction corresponds to 21.5 radiation lengths (X_0) in total. In the $\phi - \theta$ direction the ECAL is divided in towers of a granularity of 10 mrad $\times$ 10 mrad (end caps) to 17 mrad $\times$ 17 mrad (barrel) which slightly depends on the angle of the particle track. The towers point to the interaction vertex. For the readout the towers are clustered in storeys. The ECAL allows the measurement of the longitudinal and transverse (to the incident particle direction) shower profile which is needed for the distinction of photons, electrons and hadrons or muons. The energy resolution of the electromagnetic calorimeter is

$$\frac{\Delta E}{E} = 0.9\ \% + \frac{18\ \%}{\sqrt{E(\mathrm{GeV})}},$$

the angular resolution

$$\sigma_\phi = \frac{\sigma_\theta}{\sin\theta} = 0.25 + \frac{2.5}{\sqrt{E(\mathrm{GeV})}}\ \mathrm{mrad}.$$

The ECAL covers the angular range $|\cos\theta| \leq 0.976$.

8.1.5 Hadronic Calorimeter and Muon Chambers

Like the ECAL the hadronic calorimeter (HCAL) consists of a barrel part and two end caps. The HCAL is a 23 layer iron and streamer tube sandwich calorimeter. The iron also serves as yoke for the magnetic flux and as muon filter. The streamer tubes are filled with a mixture of 22.5% Argon, 47.5% CO_2 and 30% Isobutane. For hadrons with an incident angle of 90° the HCAL is 7.16 interaction lengths (λ_0) thick. Each layer of streamer tubes is equipped with pad readout for integrated energy flux measurement and with strips, parallel to each tube for digital reconstruction of the track pattern. The pads of each layer are connected together to form towers pointing to the interaction vertex. The tower granularity is typically $3.7^o \times 3.7^o$. The energy resolution of the HCAL is

$$\frac{\Delta E}{E} = \frac{85\ \%}{\sqrt{E(\mathrm{GeV})}}.$$

The HCAL covers the angular range $|\cos\theta| \leq 0.9899$.

The muon chambers outside the hadronic calorimeter are used to identify muons since only muons (and neutrinos) can penetrate the HCAL material. The muon chambers consist of two layers of chambers with stereo planes of streamer tubes yielding three-dimensional coordinates. The spatial resolution is 0.35 cm (to be compared with the multiple scattering uncertainty of 23 cm / p $(\mathrm{GeV}/c)^{-1}$).

8.1.6 Luminosity Monitors

The luminosity is determined by measuring the rate of small angle Bhabha scattering. This QED process is well understood. The Bhabha cross-section rate is largest under small angles because the cross-section has a $\sin^{-4}(\theta/2)$ dependence. To distinguish beam background a good energy resolution and a good electron identification are needed. The luminosity calorimeters (LCAL) are located at a distance of $\pm$ 2.67 m from the interaction point and cover an angular range of 45 mrad $< \theta <$ 160 mrad. They consist of 38 layers of lead and proportional chambers and have a thickness of 24.6 radiation lengths. The silicon calorimeters (SiCAL) are located at a distance of $\pm$ 2.5 m from the interaction point and cover an angular range of 24 mrad $< \theta <$ 58 mrad. They consist of twelve layers silicon and tungsten corresponding to 24 radiation lengths. Since the LCAL rate is not sufficient for a luminosity measurement during the running, two additional Bhabha calorimeters (BCAL) have been installed at a distance $\pm$ 7.7 m from the interaction point covering an angular range of 5.1 mrad $< \theta <$ 6.7 mrad. These calorimeters consist of ten layers tungsten and plastic scintillators with a thickness of 22 radiation lengths.

8.2 Description of the Standard ALEPH W Analysis

Since the analysis described in this thesis is done with purely hadronic events the brief description of the standard ALEPH analysis will concentrate on $W^+W^- \to q\bar{q}q\bar{q}$ events. Figure 8.3 shows

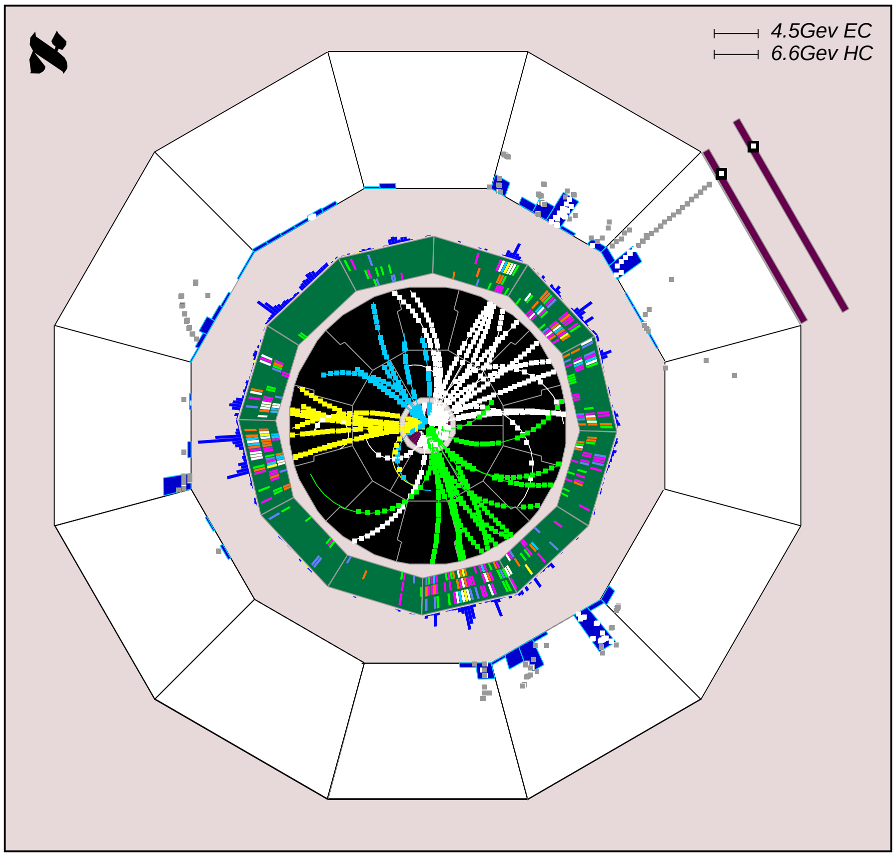

Fig. 8.3: *Hadronic decay of a W pair in the ALEPH detector at a center-of-mass energy of 189 GeV. The plot shows a cross section of the detector in a representation of the `DALI` program. The four jets of the event are clearly visible.*

such a hadronic W decay for a center-of-mass energy of 189 GeV. The four jets corresponding to the four initial quarks are clearly visible. A detailed description of the ALEPH analysis procedure can be found in [57] and [58].

The W mass is extracted by comparing the experimental invariant mass distributions to the corresponding Monte Carlo distributions, where generated events are processed through a full simulation of the ALEPH detector response and through the same reconstruction chain as real data. The `KORALW` [59] event generator is used to produce reference W events. At energies well above the W pair production threshold the main source of background is the process $e^+e^- \to q\bar{q}(\gamma)$. To select hadronic decays preselection cuts are applied. To mention the most important cuts: the longitudinal momentum $p_{||}$ of the event relative to the beam axis must satisfy $|p_{||}| \leq 0.95\ (m_{vis} - m_Z)$ where m_{vis} is the so-called visible mass (reconstructed invariant mass of the total observed energy in the detector) and the event sphericity has to be larger than 0.03. The sphericity is proportional to the sum of the transverse momenta squared with respect to the event axis which minimizes this sum. Formally it is defined as

$$S = \frac{3}{2} \min \left(\frac{\sum \vec{p}_\perp^2}{\sum \vec{p}^2} \right) .$$

A di-jet event has a sphericity $S \approx 0$, an isotropic event $S \approx 1$. The cut on $S > 0.03$ excludes therefore di-jet events. A neural network is used to tag the preselected events. The events remaining after the cuts are forced into four jets using the `DURHAM-P` algorithm [60] (see following chapter) where the objects are clustered by their three-momenta and then each jet four-momentum is recalculated taking the object masses into account (called `DURHAM-PE` scheme).
To improve the mass resolution a four-constraint ("4C") kinematic fit employing Lagrange multipliers is performed on each event. The constraints used are the conservation of the three-momentum of the four jets and the total center-of-mass energy. The fit assumes that the jet velocities remain constant. The four jets are combined into two di-jet systems in all three possible ways. For each of the combinations two rescaled masses are determined according to

$$m_{ij}^{\mathrm{resc}} = m_{ij} \frac{E_{\mathrm{beam}}}{E_i + E_j} \tag{8.1}$$

where E_{beam} is the beam energy and E_i and E_j the jet energies. The jet pairing algorithm selects the combination with the smallest difference between the two rescaled masses unless this combination has the smallest sum of the two di-jet opening angles. In this case the combination with the second smallest mass difference is selected. In the case of the analysis of the 183 GeV data both masses of the selected combination must lie within a mass window of 60 to 86 GeV/c^2 and at least one mass must be larger than 74 GeV/c^2. A binned Maximum Likelihood Monte Carlo reweighting procedure is finally employed to find the value of m_W which best fits the observed invariant mass distribution. Systematic uncertainties arise from the description of the fragmentation of the $W \to q\bar{q}$ decays, from calorimeter calibrations, from jet corrections before the kinematic fit, from initial state radiation, from reference Monte Carlo statistics and background contamination, from color reconnection and Bose-Einstein effects ("theoretical uncertainty"). The relative error of the LEP beam energy translates into the same relative uncertainty on the fitted mass because the beam energy is used directly in the kinematic fits. For the beam energy error of 1997 ($E_{cm} = 183$ GeV) this means that the beam energy error of $\Delta E_{\mathrm{beam}} = 25$ MeV translates into a systematic uncertainty of $\Delta m_W = 21$ MeV/c^2. The final result for the 183 GeV data is [58]

$$m_W^{\mathrm{hadronic}} = 80.461 \pm 0.177(\mathrm{stat.}) \pm 0.045(\mathrm{sys.}) \pm 0.056(\mathrm{theory}) \pm 0.021(\mathrm{LEP})\ \mathrm{GeV}/c^2.$$

For the 1998 data ($E_{cm} = 188.6$ GeV) the beam energy error was 20 MeV and the corresponding uncertainty of $\Delta m_W = 17$ MeV/c^2. The W mass for this dataset is [61]

$$m_W^{\mathrm{hadronic}} = 80.561 \pm 0.116(\mathrm{stat.}) \pm 0.053(\mathrm{sys.}) \pm 0.056(\mathrm{theory}) \pm 0.017(\mathrm{LEP})\ \mathrm{GeV}/c^2.$$

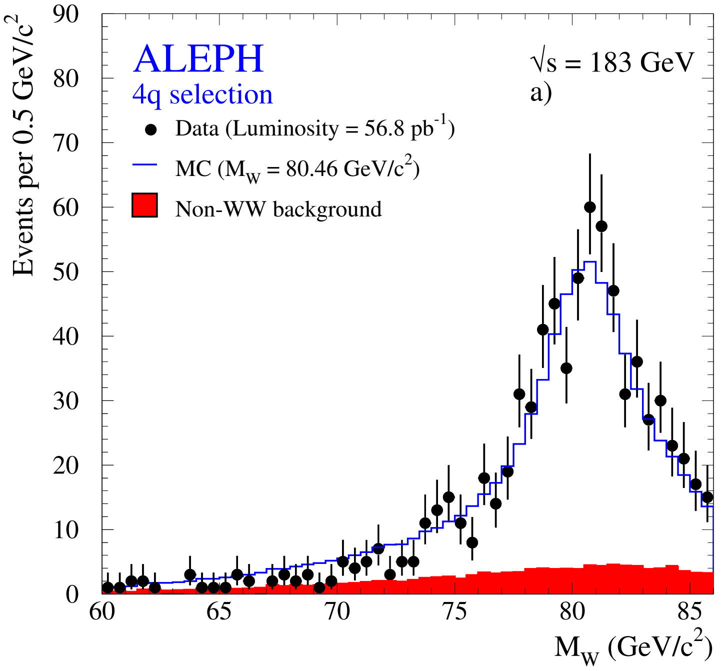

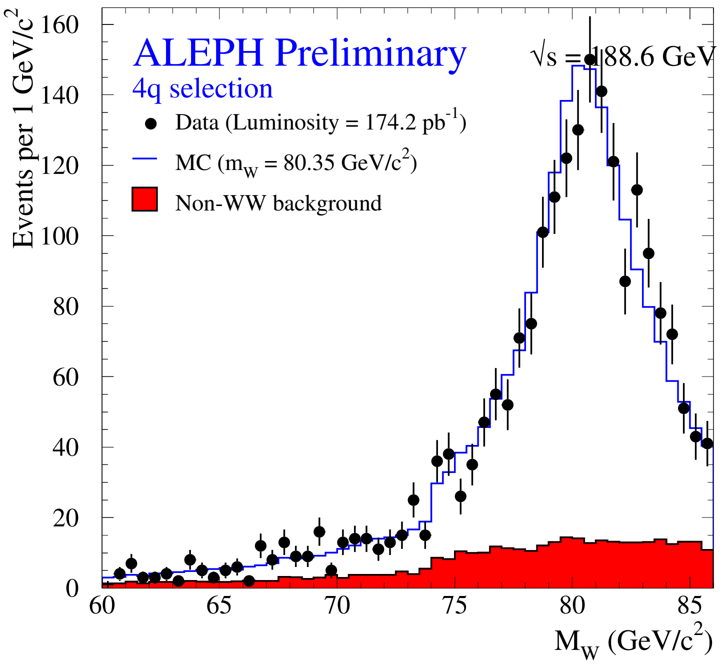

Fig. 8.4: *Distributions of the W mass for data taken at a center-of-mass energy of 183 GeV [58] and an energy of 188.6 GeV [61]. Measured data and Monte Carlo distributions are shown.*

Figure 8.4 shows the measured distributions of m_W at center-of-mass energies of 183 and 188.6 GeV for data and Monte Carlo.

The errors of these results for the fully hadronic ("4q") channel for data taken at two different center-of-mass energies are composed of a statistical, a systematic (as described above: fragmentation, jet corrections, etc.), a "theoretical" (from final state interactions (FSI) like color reconnection and Bose-Einstein effects) and a beam energy contribution. The statistical error is given by the natural width of the W, the detector resolution in invariant masses and the number of selected events. The uncertainty due to final state interactions is expected to decrease with a better theoretical understanding of the underlying physics. The systematic contributions can be reduced by a more involved analysis. The error arising from the uncertainty of the LEP beam energy and measures to reduce it are the main subject of this thesis and are discussed in detail in chapters 4 to 7.

The results of the m_W measurements given above and in fig. 8.4 represent the result of the fully hadronic ("4q") channel of the ALEPH experiment for two different center-of-mass energies or, respectively for data taken in two different years (1997 and 1998, see fig. 4.1 which shows the beam energy as a function of year). To reduce the statistical error, these results can be combined with measurements in other decay channels (semi-leptonic $W^+W^- \to q\bar{q}l\nu_l$ and fully leptonic $W^+W^- \to l\nu_l l\nu_l$). The fully leptonic decay channel yields a result on m_W which has a large uncertainty due to the undetectable neutrinos and the contribution to a weighted average of all measurements would be almost negligible. The combined result therefore consists only of contributions from the fully hadronic and the semi-leptonic channel. To further reduce the uncertainty, the combined LEP W mass result includes measurements of all four LEP experiments (ALEPH, DELPHI, L3 and OPAL). This weighted average of all results reduces effectively the total error on the W mass, due to the increased statistics and the appropriate treatment of correlations between systematic and theoretical uncertainties of the four LEP experiments (like a Monte Carlo program used by all experiments). The combined mass value from all channels ("4f", four fermions) for all measurements up to 1998 is [62]

$$m_W^{4f} = 80.347 \pm 0.036(\text{stat.}) \pm 0.036(\text{sys.}) \pm 0.020(\text{theory}) \pm 0.017(\text{LEP})\ \text{GeV}/c^2.$$

In comparison to the ALEPH results given earlier, this shows clearly that the error arising from the beam energy uncertainty will become a significant contribution when increased statistics reduces systematic and statistical uncertainties.

Figure 8.5 shows the evolution of combined LEP W mass and the corresponding error as function of time. Each point in the figure includes the statistics from the previous years. In this thesis only W mass measurements from direct reconstruction have been discussed. In 1996, LEP was operated close to the production threshold for W pairs and an indirect determination of m_W from the measured cross sections (see fig. 1.2) was possible. The result from the indirect determination ($80.400 \pm 0.220 \pm 0.025$(LEP) GeV/$c^2$ [63]) is also included in the LEP combined value.

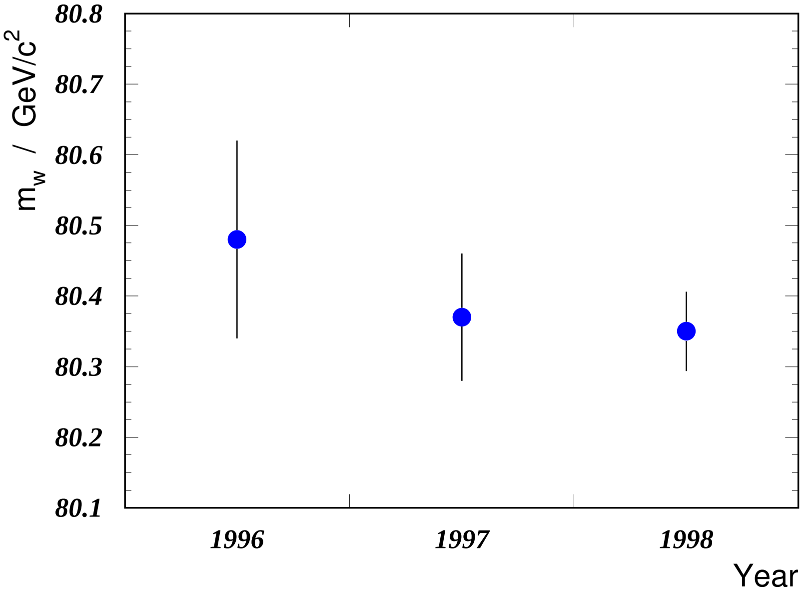

Fig. 8.5: *Evolution of the combined LEP W mass and corresponding error as function of time. Each point includes the statistics from the previous years. Values were taken from [62–64]*

Until 1998 the LEP experiments accumulated an integrated luminosity ($\int \mathscr{L} \mathrm{d}t$) of about 240 pb^{-1} per experiment. Including the data accumulated in 1999 the total integrated luminosity is 480 pb^{-1} per experiment. This is expected to reduce the statistical and systematic error on the W mass to about 25 MeV/c^2 [65, 66] which is comparable to the error from the beam energy. For the final measurement of m_W it thus is important to reduce the error on the LEP beam energy to a significantly lower value, ideally below 12 MeV.

Chapter 9

Impact of Beam Parameters on the Measurement of m_W

9.1 Analysis Strategy

An important way to improve the resolution of the W mass distribution is the kinematic fit which introduces a dependence on the accuracy of the LEP energy measurement. The rescaling of the jet masses further links the resulting W mass to the beam energy. To probe the impact of beam parameters like the energy on the measurement of m_W a generator level analysis on Monte Carlo events was performed.

9.1.1 Selection

A total number of 20000 $WW \to 4f$ events was generated with `KORALW` [59] and purely hadronic events were selected. The generator level analysis was performed on this sample. Only tracks of stable particles were considered. Figure 9.1 shows the mass distribution as generated from the MC. The following cuts for detector acceptance have been applied: A track is accepted if the angle to the beam axis is larger than 20^o. Furthermore a charged track must have a transverse momentum of more than 200 MeV/c with respect to the beam axis in order to be accepted and a neutral object must at least have an energy of 250 MeV.

9.1.2 Jet Clustering

The individual particle tracks of an event have to be combined into four jets originating from the two mother Ws. In an iterative procedure two particles out of a total number of N with the smallest distance according to a chosen metric are combined in a single new object reducing the number of objects to $N-1$. This procedure continues until the number of remaining objects is

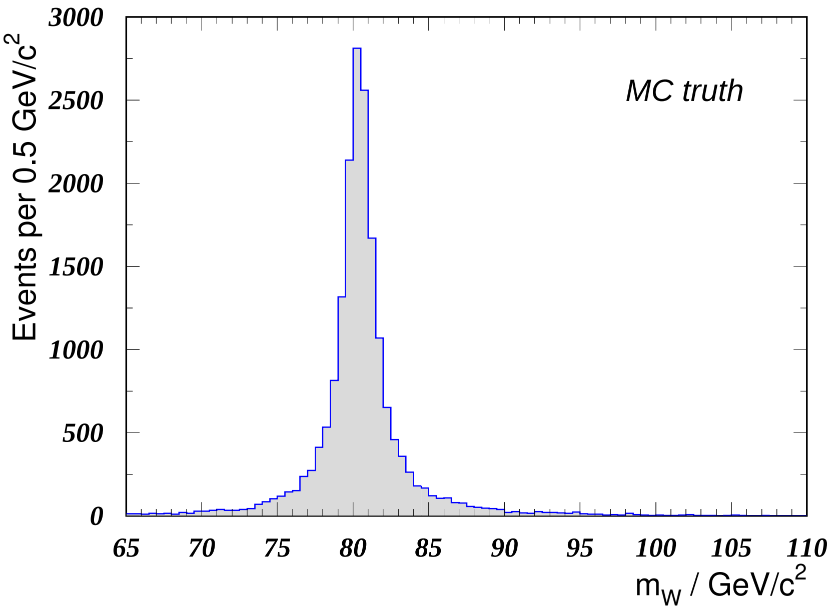

Fig. 9.1: *Distribution of W masses in purely hadronic events generated with* `KORALW` *[59]. The total number of generated WW events is 20000.*

four. Following the standard ALEPH analysis the distance measure for this study is taken to be the `DURHAM` metric [60]. The `DURHAM` metric is based on the relative transverse momentum of two objects i and j normalized to the square of the visible energy of the event:

$$y_{ij} = \frac{2 \ \min\left(E_i^2, E_j^2\right)}{E_{vis}^2} \ (1 - \cos\theta_{ij}) \, . \tag{9.1}$$

The combination of objects is done after the so-called PE-scheme. In the E-scheme the four-momenta of the two objects are summed up:

$$E_{ij} = E_i + E_j, \quad \vec{p}_{ij} = \vec{p}_i + \vec{p}_j.$$

This Lorentz-invariant scheme gives a good energy resolution. In the P-scheme, the three-momenta are summed up and the energy is scaled to obtain a massless object:

$$E_{ij} = |\vec{p}_{ij}|, \quad \vec{p}_{ij} = \vec{p}_i + \vec{p}_j.$$

This combination results in better reconstruction of the jet directions but the energy resolution gets poorer. It is possible to combine the two schemes to a PE-scheme: the selection of objects belonging to a jet is done with the P-scheme, the final combination according to the E-scheme which conserves the four-momentum of the jets.

9.1.3 Jet Pairing

A jet pairing algorithm is needed to identify the two jets originating from the same W boson. The algorithm chosen for this study selects the combination of jets with the smallest asymmetry of masses if both invariant masses of the combined jets are larger than 65 GeV/c^2.

9.1.4 Kinematic Constraints

To obtain a better mass resolution kinematic constraints are introduced. The constraints are supplied by four-momentum conservation. For that purpose the energies of the "massless" jet objects are rescaled solving a system of equations:

$$\begin{pmatrix} 1 & 1 & 1 & 1 \\ e_{1x} & e_{2x} & e_{3x} & e_{4x} \\ e_{1y} & e_{2y} & e_{3y} & e_{4y} \\ e_{1z} & e_{2z} & e_{3z} & e_{4z} \end{pmatrix} \begin{pmatrix} E_1 \\ E_2 \\ E_3 \\ E_4 \end{pmatrix} = \begin{pmatrix} \sqrt{s} \\ 0 \\ 0 \\ 0 \end{pmatrix} \tag{9.2}$$

where $\hat{e}_i$ are the direction vectors of the four jets and $\sqrt{s}$ is the center-of-mass energy. This kinematic constraint introduces a dependence on the beam energy in the W mass determination. To further improve the mass resolution the jet masses can be rescaled according to eq. (8.1) which

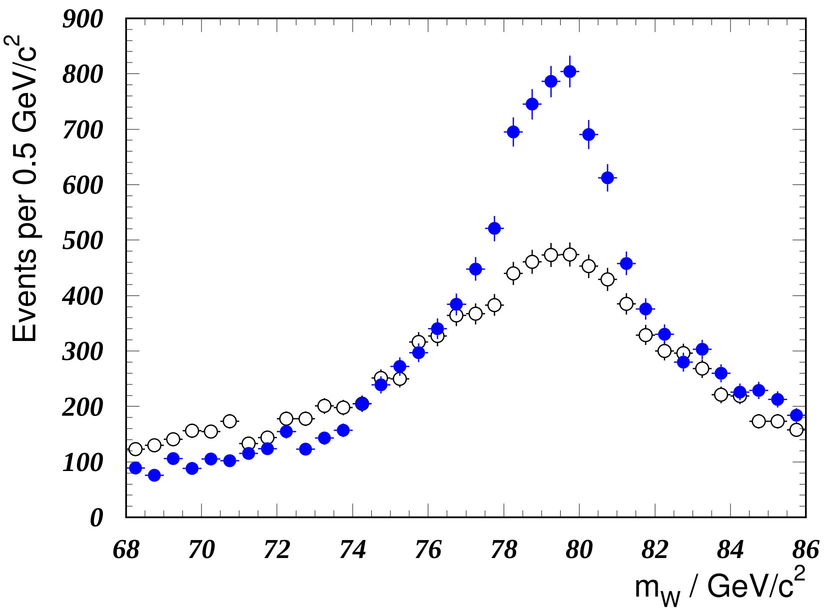

Fig. 9.2: *W mass from hadronic events at generator level with four-momentum conservation constraint with (filled circles) and without (open circles) mass rescaling.*

enhances the dependence on the beam energy. The effect of a jet mass rescaling according to eq. (8.1) can be seen in fig. 9.2. The histogram with the open circles represents a reconstructed mass distribution with only the four-momentum conservation constraint, the filled circles a distribution with mass rescaling. It is obvious that the jet mass rescaling improves the mass resolution. The mass rescaling is not employed for the studies described in the following.

9.2 Beam Parameters and m_W

9.2.1 Beam Energy Uncertainty

Rescaling of jet energies by kinematic constraints and rescaling of invariant masses induces a sensitivity to the beam energy. The relative error of the beam energy translates into the same relative uncertainty on the extracted W mass $\Delta m_W/m_W = \Delta E_{\text{beam}}/E_{\text{beam}}$ since for example the rescaled mass is directly proportional to the beam energy. For the W mass analysis a reduction of the energy error from currently 20 to 10 MeV would be equivalent to more than doubling the integrated luminosity [67]. The beam energies and corresponding uncertainties are determined as described in detail in chapter 4. The LEP beam energies are recorded every 15 minutes or more frequently if significant shifts in the RF frequency happened. The instantaneous values recorded nearest in time to the selected events are used in the standard ALEPH analysis. This procedure ensures that the energy uncertainty relevant for the analysis is covered by the beam energy error.

9.2.2 Energy Asymmetries and Boosts

The constraints discussed in section 9.1.4 and implemented in eq. (9.2) are based on the assumption that the W pair production happens at rest. This is only the case if electron and positron participating in the reaction have exactly the same energy. An asymmetry of the local electron and positron beam energies in the interaction point can for example be caused by an asymmetry in the RF voltage supply to the beam on both sides of the experiment. This voltage asymmetry happens for example if an RF unit on one side trips in which case the missing voltage has to be compensated by other RF units. The energy difference between electron and positron beam due to this effect is typically in the range of 20 to 70 MeV. Another source of energy asymmetries is the natural energy spread of the beams which is proportional to the bunch length and the synchrotron tune (see eq. (4.9)). The spread in center-of-mass energy which is relevant for the extraction of m_W is of the order of 200 MeV.
The asymmetry of the beam energies leads to boosts of the W^+W^- system. The change in center-of-mass energy due to a voltage asymmetry is negligible: for an average beam energy of $\langle E_{\text{beam}}\rangle = 100$ GeV and deviations of the beam energies from the average of + 100 MeV for one beam and − 100 MeV for the other beam the change in E_{cm} is only about 100 keV. The resulting boost, however, changes the angles of the jets originating from the quarks of the decaying W boson. The change in angle can easily be estimated from a simple Lorentz boost in the direction

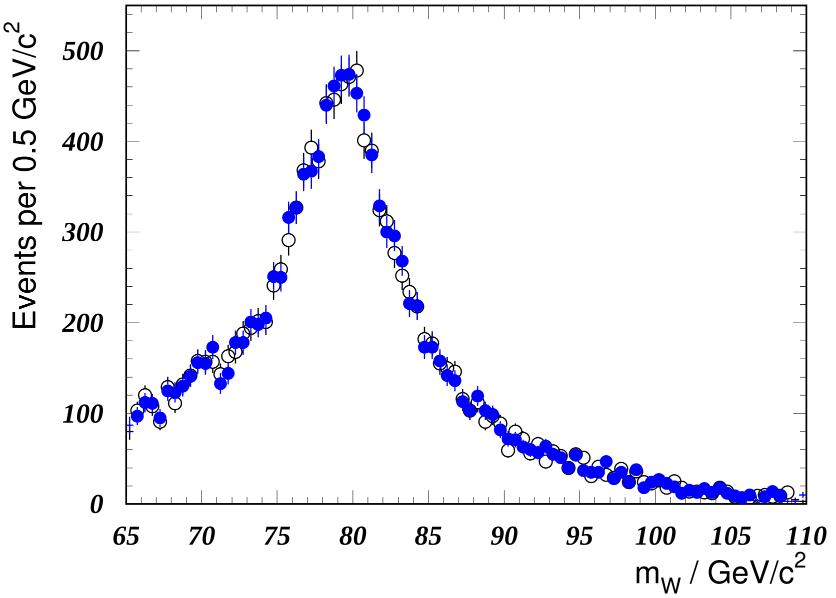

Fig. 9.3: *W mass reconstructed from purely hadronic events at generator level with kinematic constraints (four-momentum conservation, "4C"). The filled circles denote the distribution for a W pair production in rest, the open circles for a boosted case (p_z = 200 MeV/c).*

of the beam axis (z-direction). The change in angle is given by

$$\cos\theta' = \frac{\beta + \cos\theta}{1 + \beta\cos\theta} . \tag{9.3}$$

For a $\beta \ll 1$ this means that the average change of angle is given by $2/3\ \beta$. The invariant mass of two massless objects is given by $m^2 = 2E_iE_j(1 - \cos\theta_{ij})$. Since the *W*s are slow the opening angle θ_{ij} between the two jets will in general be larger than 90°. In a conservative estimate the invariant mass is therefore given by $m^2 = 2E_iE_j$ and the change in m^2 by $\Delta m^2 = 2E_iE_j 2/3\beta$. A first order approximation yields a change in reconstructed mass of $\Delta m = 2/3\beta m$. For a $\beta \approx 10^{-3}$ the mass change is of the order of 50 MeV/c^2. In contrast to the small change in center-of-mass energy due to a boost the change in mass caused by the change in the angles is non-negligible. To test the analytical estimates an analysis on Monte Carlo events at generator level was done.

9.3 Monte Carlo Studies

The full analysis described earlier in this chapter was performed with the original Monte Carlo events and with a dataset where all particle tracks have been boosted along the z-axis with a longitudinal momentum p_z = 200 MeV/c for the center-of-mass system. The mass of the Lorentz-system is given by E_{cm}. Figure 9.3 shows the distribution of the *W* mass reconstructed from purely hadronic events at generator level with kinematic constraints. The filled circles denote the distribution for a W pair production in rest, the open circles for the boosted case. At that scale no significant difference is visible. The analyses with and without boost of 200 MeV/c were repeated for varied assumptions of the center-of-mass energy for the kinematic constraints. Figure 9.4 shows how the value of the reconstructed mass changes as a function of the change

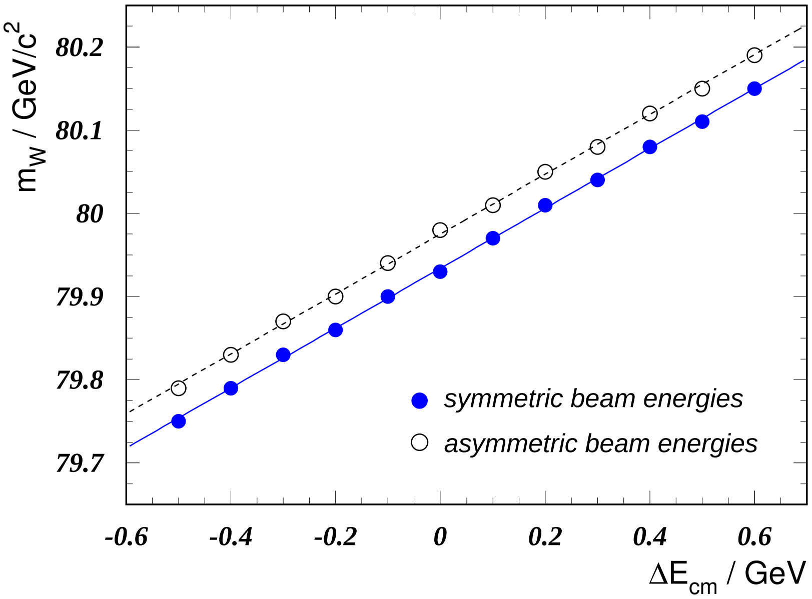

Fig. 9.4: *W mass from hadronic events at generator level as function of deviation from center-of-mass energy for symmetric and asymmetric electron and positron beam energies.*

in center-of-mass energy for the boosted (open circles) and the regular case (filled circles). The change in m_W caused by a boost of 200 MeV/c along the beam axis is found to be 41 MeV/c^2 which is consistent with the approximative estimate.

The mass change due to the E_{cm} assumption for the kinematic constraints visible in the slopes of fig. 9.4 confirms the scaling of the mass uncertainty with the beam energy error $\Delta m_W/m_W = \Delta E_{\mathrm{beam}}/E_{\mathrm{beam}}$. In a realistic scenario the shifts of m_W due to RF asymmetries are negligible since the typical asymmetries are small. The effect of the beam energy spread leads to larger boosts but for this case the center-of-mass energy does not stay constant as in the study described previously, resulting in an additional smearing of the reconstructed masses and a reduced mass shift of 16 MeV/c^2. A full simulation in the standard ALEPH environment is under study. It will show how much of the effects discussed here have to be taken into account for the W mass determination.

Chapter 10

Summary

The measurement of the W mass requires an accurate determination of the beam energy and a good understanding of the accelerator to guarantee stable running with high luminosities at high beam energies. In this thesis a reliable new method was developed to measure the horizontal anharmonicity or detuning with amplitude which turned out to be a very important stability criterion for the LEP high energy optics. The detuning with amplitude was measured for various optics using measurements of the center-of-charge position of a bunch oscillating after a single excitation. In general there is a reasonable agreement of measurements and predictions of the MAD simulation program.
The beam energy of LEP is used as a kinematic constraint in the determination of the mass of the W boson. The relative error on the beam energy therefore translates into the same relative uncertainty on the fitted masses. Generator level Monte Carlo studies confirm this dependence. Asymmetries in the RF voltage supply to the beam on both sides of the detector lead to asymmetries of the local electron and positron beam energies in the interaction point. In the simple generator level analysis a longitudinal boost caused by this kind of energy asymmetry of $p_z = 200$ MeV/c leads to a shift in W mass of 41 MeV/c^2. The typical energy difference between electron and positron beam due to an RF asymmetry is about 20 to 70 MeV and the mass shift is therefore negligible. Another source of energy asymmetries is the natural energy spread of the beams which is of the order of 150 MeV per beam. The typical beam energy spread leads to larger boosts than an RF voltage asymmetry and to a spread in center-of-mass energy. For this case the mass shift was found to be as large as 16 MeV/c^2. However only a full simulation in the standard ALEPH environment will show how much of this effect has to be taken into account in the W mass determination.
The standard procedure of the LEP2 energy calibration is based on precise energy determinations in the energy range from 40 to 60 GeV and on magnetic extrapolations to the respective physics energies (80 to 102 GeV). These extrapolations show differences of the order of 15 MeV which are not fully understood and enter as a large contribution into the uncertainty on the beam energy. To provide an independent cross check for the standard extrapolations three methods

to determine the beam energy above the W pair production threshold based on measurements of the energy loss have been developed and studied in this thesis. Since the energy loss increases with the fourth power of energy, observables sensitive to the energy loss per turn can be used to determine the beam energy.

The radiation damping component of transverse coherent beam oscillations depends on the energy loss per turn. A determination of the damping times can therefore yield the beam energy. The relative accuracy of the method is of the order of 1 %. This uncertainty is too large to serve as a cross check for the standard extrapolations since the required relative uncertainty is of the order of 10^{-4} (or 10 MeV).

The horizontal beam position is a function of the local beam momentum. The continuous energy loss due to synchrotron radiation in the arc sections and the discrete energy gains from the RF system lead to sawtooth-like horizontal orbits in the LEP ring which can be used to determine the beam energy. Since the orbit measurement is completely parasitic this method does not require dedicated measurement time and the beam energy can be determined for the exact time of data taking of the LEP experiments. The relative statistical energy uncertainty of this method is of the order of $5\ 10^{-4}$ but it is strongly limited by systematic effects.

The beam energy measurement based on the analysis of synchrotron oscillations provides a powerful and reliable high precision cross check for high energy calibration. The dependence of the synchrotron tune on various parameters was studied in detail to control systematic effects on the analysis. The error was found to be in the range from 20 to 30 MeV. Future experiments and studies are expected to substantially reduce this uncertainty. Already at the current level of precision the method has become an important tool for the LEP2 energy calibration and will contribute to the reduction of the energy uncertainty. For the W mass analysis a reduction of the energy error from currently 20 to 10 MeV would be equivalent to more than doubling the integrated luminosity of LEP2.

Appendix A

List of Symbols

Symbol	Quantity	Units
α_c	momentum compaction factor	–
β	velocity relative to the speed of light	–
$\beta(s)$	betatron amplitude function	m
B	magnetic field	T
C	machine circumference	m
C_γ	Sand's synchrotron radiation constant for e^-	$m(GeV)^{-3}$
D	dispersion	m
$\mathcal{D}$	damping parameter	–
E_0	beam energy	GeV
E_{cm}	center-of-mass energy	GeV
f_{rev}	revolution frequency	Hz
g	voltage correction factor	–
h	harmonic number	–
$J_{x,y,\varepsilon}$	damping partition number	–
k	normalized quadrupole strength	m^{-2}
L	path length on closed orbit	m
$\mathscr{L}$	luminosity	pb
m_W	mass of the W boson	GeV/c^2
M	RF distribution correction	$(GV)^{-4}$
p	momentum	GeV/c
p_0	momentum of reference particle	GeV/c
$Q_{x,y,s}$	horizontal, vertical and synchrotron tune	–
Q'	chromaticity	–
$\partial Q_x/\partial W_x$	horizontal anharmonicity	m^{-1}
ρ	bending radius	m
$\sigma_{x,y,s}$	tranverse and longitudinal bunch length	m
σ_ε	energy spread	MeV
s	longitudinal coordinate	m
$\tau_{x,y,\varepsilon}$	damping time	s
u	transverse coordinate (x or y)	m
U_0	energy loss per turn	MeV
V, V_{RF}	RF voltage	V
W	Courant-Snyder invariant	m
Z	impedance	Ω

Appendix B

Systematic Studies of the Q_S Fit Model

The total differential of the fit model eq. (7.10) helps probing the dependence of the fit on the individual input parameters. It is given by

$$\begin{aligned}
dQ_s^4 &= 2\alpha_c \left(\frac{h}{2\pi}\right)^2 \left\{ \frac{g^2V_{RF}^2 - \tilde{U}_0^2}{E_c^2} + Mg^4V_{RF}^4 - \frac{\nu\left(g^2V_{RF}^2 - \tilde{U}_0^2\right)}{\alpha_c\ E_c^2\ (1-\frac{\nu}{\alpha_c})} \right\} \Delta\alpha_c \\
&+ \left(\frac{\alpha_c\ h}{2\pi}\right)^2 \left\{ \frac{2g^2V_{RF}^2}{E_c^2} + 4Mg^3V_{RF}^4 \right\} \Delta g \\
&+ \left(\frac{\alpha_c\ h}{2\pi}\right)^2 \left\{ -\frac{2\tilde{U}_0}{E_c^2} \right\} \Delta K \\
&+ \left(\frac{\alpha_c\ h}{2\pi}\right)^2 \left\{ g^4\ V_{RF}^4 \right\} \Delta M \\
&+ \left(\frac{\alpha_c\ h}{2\pi}\right)^2 \left\{ -\frac{2\tilde{U}_0 E^4}{E_c^2} \right\} \Delta\left(\frac{C_\gamma}{\rho}\right) \\
&+ \left(\frac{\alpha_c\ h}{2\pi}\right)^2 \left\{ -\frac{2\left(g^2V_{RF}^2 - \tilde{U}_0^2\right)}{E\ E_c^2} - \frac{8\tilde{U}_0\left(\frac{C_\gamma}{\rho}\right)E^3}{E_c^2} \right\} \Delta E \\
&+ \left(\frac{\alpha_c\ h}{2\pi}\right)^2 \left\{ \frac{2g^2V_{RF}}{E_c^2} + 4Mg^4V_{RF}^3 \right\} \Delta V_{RF}
\end{aligned}$$

with

$$\tilde{U}_0 = \frac{C_\gamma}{\rho}E^4 + K, \qquad E_c = E\left(1 - \frac{\nu}{\alpha_c}\right), \qquad \nu = \frac{(f_{RF} - f_{RF}^c)}{f_{RF}}.$$

To better understand the structure of the dependencies, the fit model's differential can be rewritten for the idealized case without frequency deviation ($\nu = 0$) or additional energy losses

($K = 0$) and a voltage correction factor of $g = 1$

$$
\begin{aligned}
dQ_s^4 &= 2\alpha_c \left(\frac{h}{2\pi}\right)^2 \left\{ \frac{V_{RF}^2}{E^2} - \left(\frac{C_\gamma}{\rho}\right)^2 E^6 + M V_{RF}^4 \right\} \Delta\alpha_c \\
&+ \left(\frac{\alpha_c\, h}{2\pi}\right)^2 \left\{ \frac{2V_{RF}^2}{E^2} + 4MV_{RF}^4 \right\} \Delta g \\
&+ \left(\frac{\alpha_c\, h}{2\pi}\right)^2 \left\{ -2\left(\frac{C_\gamma}{\rho}\right) E^2 \right\} \Delta K \\
&+ \left(\frac{\alpha_c\, h}{2\pi}\right)^2 \left\{ V_{RF}^4 \right\} \Delta M \\
&+ \left(\frac{\alpha_c\, h}{2\pi}\right)^2 \left\{ -2\left(\frac{C_\gamma}{\rho}\right) E^6 \right\} \Delta\left(\frac{C_\gamma}{\rho}\right) \\
&+ \left(\frac{\alpha_c\, h}{2\pi}\right)^2 \left\{ -\frac{2V_{RF}^2}{E^3} - 6\left(\frac{C_\gamma}{\rho}\right)^2 E^5 \right\} \Delta E \\
&+ \left(\frac{\alpha_c\, h}{2\pi}\right)^2 \left\{ \frac{2V_{RF}}{E^2} + 4MV_{RF}^3 \right\} \Delta V_{RF}
\end{aligned}
$$

In the case of homogeneously distributed RF voltage ($M = 0$) and neglecting a possible uncertainty of the voltage determination ($\Delta V_{RF} = 0$) the total differential of the Q_s fit model sorted by powers of the energy is:

$$
\begin{aligned}
dQ_s^4 \left(\frac{2\pi}{\alpha_c h}\right)^2 &= \left\{ \Delta M\, V_{RF}^4 \right\} + \left\{ -2\left(\frac{C_\gamma}{\rho}\right) \Delta K \right\} E^2 \\
&+ \left\{ 2\, V_{RF}^2 \left(\frac{\Delta\alpha_c}{\alpha_c} + \Delta g - \frac{\Delta E}{E} \right) \right\} \frac{1}{E^2} \\
&+ \left\{ 2\, \left(\frac{C_\gamma}{\rho}\right)^2 \left(-\frac{\Delta\alpha_c}{\alpha_c} - 3\,\frac{\Delta E}{E} - 2\,\frac{\Delta\left(\frac{C_\gamma}{\rho}\right)}{\left(\frac{C_\gamma}{\rho}\right)} \right) \right\} E^6
\end{aligned}
$$

Appendix C

The Bending Radius of LEP

The bending radius ρ is a central parameter of a circular accelerator since it defines its size and many beam parameters depend on it. It must be known accurately to evaluate the energy loss since the instantaneous synchrotron radiation power is

$$P_\gamma = \frac{C_\gamma}{2\pi}\, c\, \frac{E^4}{\rho^2} \;\propto\; E^2\, B^2$$

The importance of the radius for the beam energy determination using measurements of the synchrotron tune was shown in chapter 7. Due to the simple modeling used in the normal LEP simulations the radius calculated with MAD has to be corrected to take into account effects like dipole fringe fields. The table of fig. C.1 gives a schematic overview of the problem already described in section 7.3.7. The approximation by a rectangular magnet works well for the integral

	"LEP"		"MAD"
"shape" Ω :	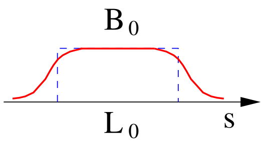		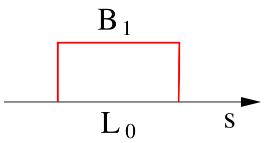
$\int B ds$:	$B_0 \int \Omega ds$	$=$	$B_1 L_0$
$U_0 \sim \int B^2 ds$:	$B_0^2 \int \Omega^2 ds$	$<$	$\frac{B_0^2}{L_0} \left(\int \Omega ds\right)^2$

Fig. C.1: *Calculation of magnetic field integral and integral over the square of the magnetic field for a realistic magnet ("LEP") and treatment in the simulation program "MAD". The field B_1 is adjusted such that the integral over the field which defines the beam energy stays constant.*

over the magnetic fields but for energy loss calculations ($U_0 \propto \int B^2 ds$) this approximation always slightly overestimates the real energy loss. For an accurate determination of the real integral over the square of the magnetic field, the end fields of the LEP dipoles were measured in situ.

C.1 Measurement of Dipole Fringe Fields

The LEP bending dipoles consist of excitation bars with steel-concrete cores. Most magnets are arranged in groups of six cores (three pairs of cores). For details on the LEP magnets see [1]. Figure C.2 shows a drawing of a six core dipole. The gaps between two cores forming a pair is 54 mm, the gap between two pairs is 340 mm. From the drawing it is clear that "end fields"

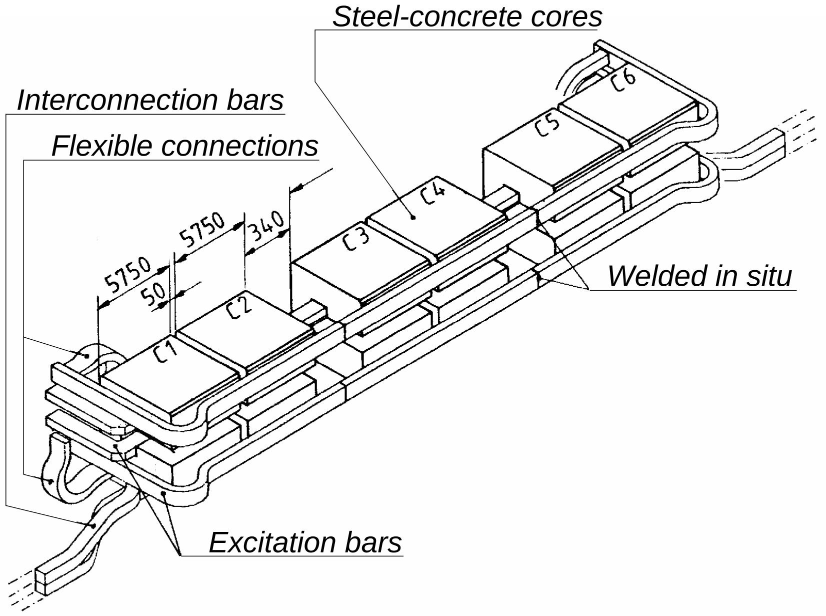

Fig. C.2: *LEP six core dipole. The grouping of the cores into three pairs with small gaps (54 mm) between two cores of a pair and larger gaps (340 mm) between the pairs is clearly visible.*

do not only occur at the extreme ends of the six core group but also in the gaps between the cores. The excitation bars also contribute to the gap field. In the short gaps the field does not change significantly from the core field. The case is different for the field in the 340 mm gaps where field measurements have been performed. Figure C.3 shows a top view of the 340 mm gap with the vacuum chamber. The lines indicate where the magnetic field was measured. The field measurements where done using a device with three hall probes oriented along three axes thus avoiding uncertainties from the probe orientation. The field distribution could only be measured outside the vacuum chamber. A three-dimensional magnet model [54] was used to extrapolate the outside measurements to the position of the beam inside the vacuum chamber. Figure C.4 and fig. C.5 show predictions of the model and the corresponding measurements for the horizontal probe positions indicated in fig. C.3. There is a very good agreement of the

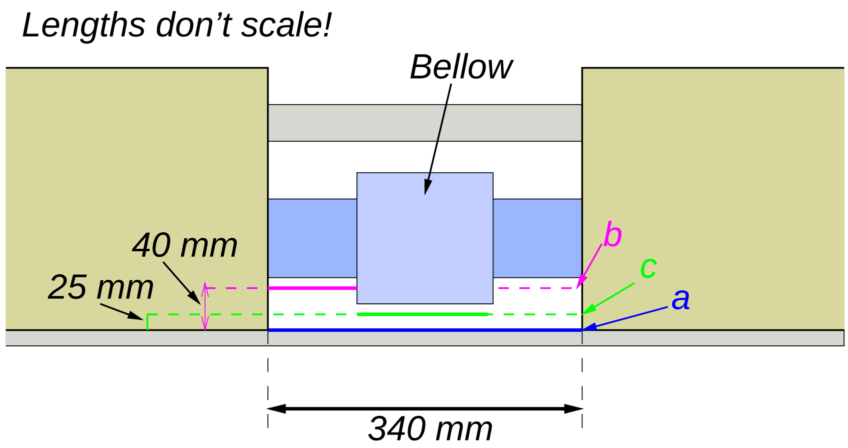

Fig. C.3: *Top view of the 340 mm gap between two pairs of cores with vacuum chamber. The lines labeled a, b and c denote the places where field measurements have been done.*

absolute predictions of the model and the measured fields outside the vacuum chamber. The model can therefore be trusted to predict the real field on the beam axis (thick line without overlay of measurements in fig. C.4 and fig. C.5).
Taking into account the different dipole types in the LEP ring, the correction to the radius extracted from MAD is determined to be 1.6 % using the relations given in Figure C.1.

C.2 Determination of the effective $1/\rho$

The fits to the measurements of the synchrotron tune prefer a smaller correction of the effective parameter $1/\rho$ from MAD than the one determined by explicit calculation of the dipole fringe fields. This could indicate non-modeled energy losses also depending on the energy to the fourth power like synchrotron radiation losses. This effect is not yet fully understood.
To evaluate the effective radius correction relevant for the energy measurement with Q_s, energies determined with the Q_s method (including voltage calibration at low energies and application of the determined voltage correction factor to the high energy fits) are compared with NMR energies (see chapter 4). The χ^2 for this comparison is defined as

$$\chi^2 = \frac{(E_{Q_s} - E_{\mathrm{NMR}})^2}{(\sigma_{E_{\mathrm{NMR}}})^2}. \tag{C.1}$$

Figure C.6 shows the sum of these χ^2 for all high energy determinations as function of the radius correction. The value of the correction used in the fits was the preliminary estimate of 0.28 %. Figure C.6 shows that this value is very close to the minimum. It was kept in the procedure to avoid biasing the Q_s energy results towards the NMR measurements. This study shows that the effective correction to $1/\rho$ can be obtained from dedicated measurements at low beam energies where the results can be compared with resonant depolarization. The comparison of Q_s energies

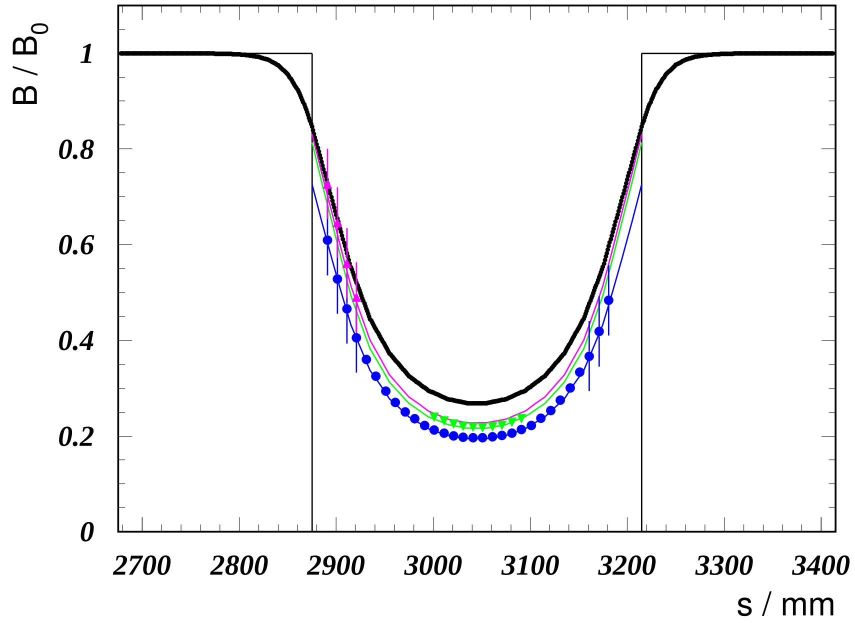

Fig. C.4: *Relative change of magnetic field as function of longitudinal coordinate s in the 340 mm gap between two pairs of cores. The lines are field calculations from a three-dimensional magnet model [54]. The different lines stand for the different horizontal locations of fig. C.3. The lines are overlaid by the actual measurements of the gap fields.*

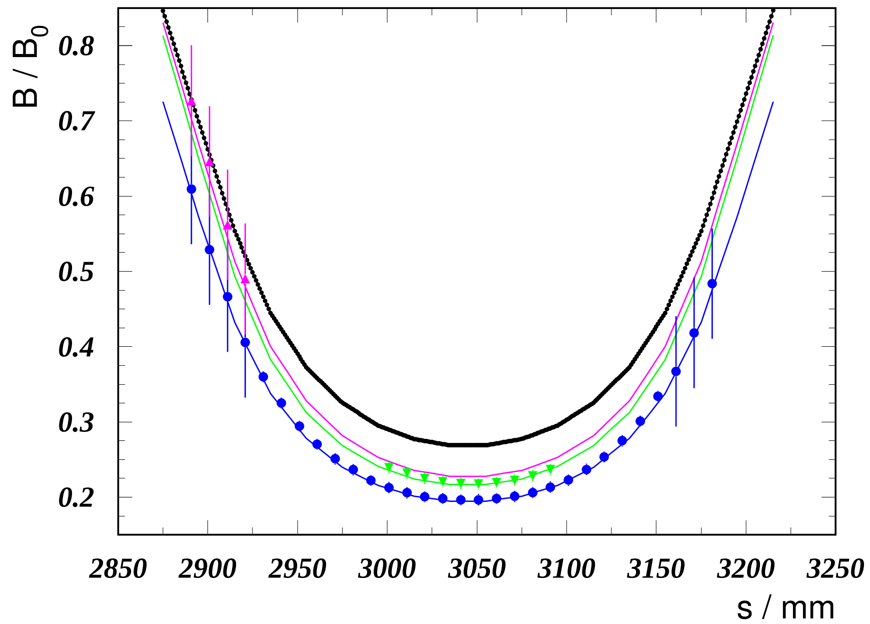

Fig. C.5: *Zoom into figure C.4. The line not overlaid by measurements represents the field on the beam axis which is relevant for the radius calculations.*

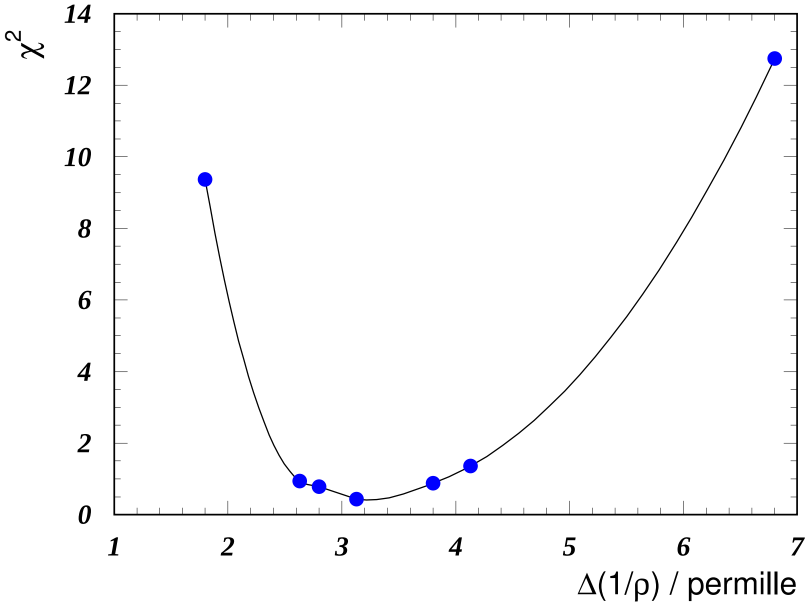

Fig. C.6: χ^2 *for the comparison of NMR energies and energies resulting from the* Q_s *method as function of a change in inverse bending radius. The curve is spline to guide the eye.*

and polarization energies should give a reliable measure of the radius correction.
For the time being, the uncertainty on the beam energy determined with the Q_s method for a "central" correction value (minimum χ^2) is 11 MeV which is equivalent to the quoted 15 MeV energy shift for a 0.1 % change in inverse radius.

Bibliography

[1] LEP Design Report, Vol II, The LEP Main Ring. CERN LEP 84-01, 1984.

[2] LEP Design Report, Vol III, LEP2. CERN-AC/96-01 (LEP2), June 1996.

[3] J. Ellis. Phenomenology of LEP 2 Physics. CERN-TH 97-131, CERN, 1998.

[4] The figure was kindly provided by G. Quast.

[5] G. Quast. Experimental Results on the Electroweak Interaction. In *Prog. Part. Nucl. Phys.*, volume 43, pages 87–166. 1999.

[6] S. Myers. Performance Related Measurements on LEP. CERN-SL 99-002-DI, CERN, 1999.

[7] H. Wiedemann. *Particle Accelerator Physics*, volume I. Springer-Verlag, 1993.

[8] H. Wiedemann. *Particle Accelerator Physics*, volume II. Springer-Verlag, 1995.

[9] K. Wille. *Physik der Teilchenbeschleuniger und Synchrotronstrahlungsquellen.* Teubner, 1992.

[10] J. Rossbach and P. Schmüser. Basic course on accelerator optics. In S. Turner, editor, *Proceedings of the Fifth General Accelerator Physics Course*, volume I, pages 17–88. CERN Accelerator School, 1992. Published as a CERN Yellow Report CERN 94-01.

[11] The figure was kindly provided by J. Wenninger.

[12] M. Sands. The Physics of Electron Storage Rings. SLAC REPORT 121, SLAC, 1970.

[13] K. W. Robinson. Radiation Effects in Circular Electron Accelerators. In *Physical Review*, volume 111, pages 373–380. 1958.

[14] A. Chao and M. Tigner. *Handbook of Accelerator Physics and Engineering.* World Scientific, 1998.

[15] Y. Alexahin et al. Low emittances lattices for LEP2. In *Proceedings of the 17th Particle Accelerator Conference*, 1997. also published as CERN-SL-97-030-AP.

[16] D. Brandt et al. Test of the 102°/90° optics at high energy. SL-MD Note 244, CERN, October 1997.

[17] P. Beloshitsky et al. Experimental studies of a (108°,90°) optics at 45.6 GeV.

[18] A. Verdier M. Lamont, G. Roy. Commisioning of the (131°,90°) lattice. SL-Note 98-059 MD, CERN, 1998.

[19] A. Verdier R. Bartolini, W. Scandale. Detuning with amplitude in LEP from 1000 turn measurements. SL-MD Note 207, CERN, 1996.

[20] N.R. Lomb. In *Astrophysics and Space Science*, volume 39, pages 447–462. 1976.

[21] G. C. Danielson and C. Lanczos. Improvements in Practical Fourier Analysis and Their Application to X-ray Scattering from Liquids. In *J. Franklin Inst., 233*. 1942.

[22] H. Grote and F. C. Iselin. The MAD Program, User's Reference Manual. SL Note 90-13 (AP) (Rev. 4), CERN, March 1995.

[23] N. Akasaka and S. Kamada. Experimental Study of Head-Tail Damping and Nonlinear Filamentation based on Precise Analysis of Coherent Betatron Oscillations in Electron Storage Rings. In V. Suller and Ch. Petit-Jean-Genaz, editors, *Proceedings of the 5th European Particle Accelerator Conference*, volume 2, pages 1141–1143, 1996.

[24] A. Hofmann, private communication.

[25] A.-S. Müller and J. Wenninger. Measurements of Coherent Damping and Tune Shifts with Amplitude at LEP. In *Proceedings of the 6th European Particle Accelerator Conference*, pages 1377–1379, 1998.

[26] A. Verdier, private communication.

[27] R. Assmann et al. Calibration of centre-of-mass energies at LEP1 for precise measurements of Z properties. In *Eur. Phys. J. C*, volume 06(02), pages 187–223. 1999.

[28] A. Blondel et al. Evaluation of the LEP centre-of-mass energy above the W-pair production threshold. CERN-EP 98-191, CERN, 1998.

[29] A.A. Sokolov and I.M. Ternov. On polarization and spin effects in the theory of synchrotron radiation. In *Sov. Phys. Dokl. 8*, page 1203. 1964.

[30] L. Thomas. In *Philos. Mag.*, volume 3, page 1. 1927.

[31] V. Bargmann et al. Precession of the polarization of particles moving in a homogeneous electromagnetic field. In *Phys. Rev. Lett.*, volume 2, page 435. 1959.

[32] C. Caso et al. Review of Particle Physics. In *Eur. Phys. J. C3*, volume 1. 1998.

[33] B. Dehning. *Elektronen- und Positronen-Polarisation im LEP-Speicherring und Präzisionsbestimmung der Masse des Z-Teilchens.* PhD thesis, Ludwig-Maximilians-Universität München, 1995.

[34] R. Assmann. *Optimierung der transversalen Spin-Polarisation im LEP-Speicherring und Anwendung für Präzisionsmessungen am Z-Boson.* PhD thesis, Ludwig-Maximilians-Universität München, 1994.

[35] E. Bravin et al. Energy Calibration at LEP using Nuclear Magnetic Resonance Probes. CERN-SL-98-035 BI, 1998.

[36] J. Wenninger, private communication.

[37] P. Melchior. Tidal Interactions in the Earth Moon System. In *Communications, Serie B, No. 160.* IUG General Assembly, Vienna, August 1991.

[38] L. Arnaudon et al. Effects of Terrestrial Tides on the LEP Beam Energy. In *Nuclear Instruments and Methods A357*, pages 249–252. North-Holland Publishing Company, 1995.

[39] J. Wenninger. Observation of Radial Ring Deformations using Closed Orbits at LEP. In *Proceedings of the 18th Particle Accelerator Conference*, 1999. To be published.

[40] P. Melchior. *The Tides of the Planet Earth.* Pergamon Press, 2nd edition, 1983.

[41] H. Schmickler. Measurement of the central frequency of LEP. SL-MD Note 89, CERN, 1993.

[42] J. Wenninger. Orbit Corrector Magnets and Beam Energy. SL-Note 97-06 (OP), CERN, 1997.

[43] W. Herr. Bunch Trains at High Energy. In J. Poole, editor, *Proceedings of the 6th Workshop on LEP Performance*, pages 125–131, 1996.

[44] M. Meddahi. How do We Get Optics for Energies Above 90 GeV? In J. Poole, editor, *Proceedings of the 7th Workshop on LEP Performance*, pages 91–93, 1997.

[45] The LEP energy working group. Evaluation of the LEP center-of-mass energy for data taken in 1998. LEP Energy Working Group 99/01, CERN, March 1999.

[46] J. Matheson. Status of the Spectrometer Project. talk in the SL seminar.

[47] A. Chao. *Physics of collective beam instabilities in high energy accelerators.* Wiley, 1993.

[48] The figure was kindly provided by E. Peschardt.

[49] J. C. Juillard and E. Peschardt. Damping of Longitudinal Coupled Dipole Bunch Oscillations. In P. Marin and P. Mandrillon, editors, *Proceedings of the 2th European Particle Accelerator Conference*, pages 1554–1556, 1990. Also published as CERN SL 90-81 RFL.

[50] G. Arduini et al. Parasitic Energy Loss in the LEP Superconducting Cavities. CERN-SL-97-034-AP, 1997.

[51] A. Hofmann and T. Risselada. Measuring the ISR impedance at high frequencies by observing the energy loss of a coasting beam. In *Proceedings of the 10th Particle Accelerator Conference*, pages 2400–2402, 1983. also published as CERN-LEP-ISR 83-16 rev.

[52] E. Keil. Diffraction radiation of charged rings moving in a corrugated cylindrical pipe. In *Nuclear Instruments and Methods 100*, pages 419–427. North-Holland Publishing Company, 1972.

[53] E. Rossa et al. Double sweep streak camera for LEP. In P. Marin and P. Mandrillon, editors, *Proceedings of the 2th European Particle Accelerator Conference*, pages 783–785, 1990.

[54] M. Sassowsky, private communication.

[55] D. Buskulic et al. Performance of the ALEPH detector at LEP. In *Nuclear Instruments and Methods A360*, pages 481–506. North-Holland Publishing Company, 1994.

[56] D. Schlatter et al. ALEPH in Numbers. internal note, 1996.

[57] R. Barate et al. Measurement of the W mass by Direct Reconstruction in e^+e^- Collisions at 172 GeV. In *Physics Letters B*, volume 422, pages 384–398. 1998.

[58] R. Barate et al. Measurement of the W mass in e^+e^- Collisions at 183 GeV. In *Physics Letters B*, volume 453, pages 121–137. 1999.

[59] W. Placzek Z. Wąs M. Skrzypek, S. Jadach. In *Comp. Phys. Commun.*, volume 94, page 216. 1996.

[60] S. Catani et al. In *Physics Letters B*, volume 269, page 432. 1991.

[61] R. Barate et al. Measurement of the W Mass in e^+e^- Collisions from 161 to 189 GeV. ALEPH 99-017, 1999.

[62] The LEP Collaborations ALEPH, DELPHI, L3, OPAL and the LEP Electroweak Working Group, and the SLD Heavy Flavour and Electroweak Groups. A Combination of Preliminary LEP Electroweak Measurements and Constraints on the Standard Model. CERN-EP 2000-016, 2000.

[63] The LEP Collaborations ALEPH, DELPHI, L3, OPAL and the LEP Electroweak Working Group, and the SLD Heavy Flavour Group. A Combination of Preliminary LEP Electroweak Measurements and Constraints on the Standard Model. CERN-PPE 97-154, 1997.

[64] The LEP Collaborations ALEPH, DELPHI, L3, OPAL and the LEP Electroweak Working Group, and the SLD Heavy Flavour and Electroweak Groups. A Combination of Preliminary LEP Electroweak Measurements and Constraints on the Standard Model. CERN-EP 99-15, 1999.

[65] P. Janot. Priorities for LEP in 2000. In J. Poole, editor, *Proceedings of the 10th Workshop on LEP-SPS Performance*, pages 250–258, 2000.

[66] T. Sjöstrand G. Altarelli and F. Zwirner, editors. *Physics at LEP2*, volume 1. CERN Yellow Report, 1996.

[67] P. Janot. Pre-Chamonix Meeting, Friday 14th, January 2000. minutes.

Acknowledgments

Sincere thanks to all who have contributed to the work presented in this thesis in helpful and instructive discussions. Especially I would like to thank

Prof. Dr. H.-G. Sander for friendly supervision of my thesis and making sure that it touches both accelerator and particle physics. In case of need he was always available for discussions, coming up with very constructive comments and remarks.

Prof. Dr. K. Kleinknecht for accepting me into his group and for his constant support and advice

Dr. J. Wenninger who helped me make the first steps into the exciting new world of accelerator physics, who accompanied this thesis with his advice and support and who spent numerous hours in the control room helping me to take the data for my studies

Dr. habil. G. Quast for the suggestions to apply as a CERN doctoral student, to work in energy calibration and to study the impact of the energy spread on m_W

Dr. A. Hofmann for his readiness at all times to answer and discuss any questions and for friendly help. He is a true master in explaining complicated things in simple terms.

Dr. K.-H. Kissler for giving me the opportunity to join an exciting project and support in the framework of the doctoral student program at CERN.

Dr. S. Myers for his continuous interest in my work, fruitful discussions and support in allocating MD time for the measurements which were necessary for my studies

Dr. H. Burkhardt who first pointed out to me the measurement of Q_s as a means to determine the energy loss and who introduced me to C++

Dr. A. Verdier for (among many other things) enlightening me about the anharmonicity and for exciting discussions

Dr. J. M. Jowett for explaining how MAD works and telling me the right questions to ask of the simulation

Dr. M. Schmelling, who always knows a way out of statistical traps, for technical support and kind advice in fitting subjects

Dr. G. De Rijk who helped looking for magnetic fields between magnets and Dr. M. Sassowsky who provided calculations of those fields on a very short timescale

Dr. A. Butterworth and Dr. E. Peschardt for their help with the RF system in MD and analysis

Dr. G. Morpurgo for his extremely useful 1000-turn measurement tools and his help in handling the datasets

Dr. R. Aßmann, Dr. K. Hanke, Dr. I. Reichel and Dr. F. Zimmermann for good advice and the numerous interesting discussions on physics as well as on non-physics topics

M. Haarmann, S. Schmeling, Dr. Chr. Zeitnitz and T. Ziegler for many interesting discussions I would not want to miss. Thomas introduced me to the W Monte Carlo and Sascha was a very helpful guide in the bureaucratic jungle

Dr. S. Luitz for his on-line help in computing matters, for the many interesting and instructive discussions, for playing music even at ungodly hours and for his friendship

Dr. H. Wachsmuth who always reminded my that there are worlds beyond LEP and who gave kind advice

Dr. P. Janot for his support and P.R. work for my Q_s studies and for approving even more MD time than I requested

the SL Operations Group and the LEP Energy Working Group for support and friendly acceptance

the ALEPH Collaboration for their interest in energy calibration subjects and for support

Last but not least I would like to thank my parents and my fiancé for their support and endless patience during all phases of this thesis.